The role of the microstructure in granular material instability

Nho Gia Hien Nguyen

N°d'ordre NNT : 2016LYSEI062

THESE de DOCTORAT DE L'UNIVERSITE DE LYON
opérée au sein de
INSA de Lyon

Ecole Doctorale ED162
(MEGA : Mécanique – Energétique – Génie Civil - Acoustique)

Spécialité de doctorat :
Discipline : Génie Civil

Soutenue publiquement le 24/06/2016, par :
Nho Gia Hien NGUYEN

The role of the microstructure in granular material instability

---

Devant le jury composé de :

EL YOUSSOUFI Moulay Saïd	Professeur des Universités	Université de Montpellier	Rapporteur
GUESSASMA Mohamed	Maître de Conférences	Université de Picardie Jules Verne	Rapporteur
HICHER Pierre Yves	Professeur Emérite	Ecole Centrale de Nantes	Examinateur
SIBILLE Luc	Maître de Conférences	Université Grenoble Alpes	Examinateur
DJERAN-MAIGRE Irini	Professeur des Universités	INSA de Lyon	Directrice de thèse
NICOT François	Directeur de Recherche	IRSTEA Grenoble	Co-directeur de thèse
PRUNIER Florent	Maître de Conférences	INSA de Lyon	Co-tuteur

Declaration of Authorship

I, Hien N.G. NGUYEN, declare that this thesis titled, 'The role of the microstructure in granular material instability' and the work presented in it are my own. I confirm that:

- This work was done wholly or mainly while in candidature for a research degree at this University.
- Where any part of this thesis has previously been submitted for a degree or any other qualification at this University or any other institution, this has been clearly stated.
- Where I have consulted the published work of others, this is always clearly attributed.
- Where I have quoted from the work of others, the source is always given. With the exception of such quotations, this thesis is entirely my own work.
- I have acknowledged all main sources of help.
- Where the thesis is based on work done by myself jointly with others, I have made clear exactly what was done by others and what I have contributed myself.

Signed: _____

Date: _____

"Look deep into nature, and then you will understand everything better."

Albert Einstein

Remerciement

Je tiens tout d'abord à remercier le directeur de cette thèse à Grenoble, François Nicot, pour m'avoir fait confiance malgré les connaissances plutôt légères que j'avais en octobre 2012 sur la mécanique des sols, puis pour m'avoir guidé, encouragé, conseillé, fait beaucoup voyager pendant presque quatre ans tout en me laissant une grande liberté et en me faisant l'honneur de me déléguer plusieurs responsabilités dont j'espère avoir été à la hauteur.

Mes remerciements vont également à Irini Djeran-Maigre, ma directrice de thèse à INSA de Lyon, pour la gentillesse et la patience qu'elle a manifestés à mon égard durant cette thèses, pour tous les conseils et les programmes qu'elle a bien voulu m'envoyer, pour l'hospitalité dont elle a fait preuve envers moi lors des séjours que j'ai effectués dans son groupe à LGCIE.

Je tiens à exprimer ma profonde gratitude à Florent Prunier, pour sa disponibilité, ses précieux conseils, ses corrections et ses encouragements.

Un merci en particulier à Nejib Hadda pour m'avoir aider au début de ma thèse et pour avour investi de son temps précieux afain de bien démarrer ma thèse.

Merci aux membres du jury, Pierre-Yves Hicher, Luc Sibille, Mohamed Guessasma, Moulay-Saïd El-Youssoufi pour avoir accepté d'évaluer mon travail. Mes remerciements vont également aux membres de mon comité de thèse qui m'ont permis d'avancer dans la bonne direction tout au long de la thèse.

Je suis également reconnaissant à tous mes collègues d'Irstea de Grenoble et d'INSA de Lyon, qui ont soutenu ce travail par une excellente ambiance de travail. Notamment, les thésards d'Irstea et d'INSA de Lyon pour leur aide, leur soutien, leur bonne humeur et les moments très agréables et inoubliables que nous avons passé ensemble.

Mes remerciements s'adressent enfin à mes parents, ma sœur, mon frère, pour leur soutien et leurs encouragements continus. Et à toi aussi, Jellyfish.

Nho Gia Hien NGUYEN

Abstract

Granular materials consist of dense pack of solid grains and a pore-filling element such as a fluid or a solid matrix. The grains interact via elastic repulsion, friction, adhesion and other surface forces. External loading leads to grain deformations as well as cooperative particle rearrangements. The particle deformations are of particular importance in many industry applications and research subjects, such as powder metallurgy and soil mechanics. The response of granular materials to external loading is complex, especially in case when failure occurs: the mode of the failure can be diffuse or localized, and the development of specimen pattern can be drastically different when the specimen can no longer sustain external loading.

In this thesis, a thorough numerical analysis based on a discrete element method is carried out to investigate the macroscopic and microscopic behavior of granular materials when a failure occurs. The numerical simulations include the vanishing of the second-order work instability criterion to detect failure. Furthermore, it is proved that the vanishing of second-order work coincides with the change from a quasi-static regime to a dynamic regime in the response of the specimen. Then, microstructure evolution is investigated. Evolution of force-chains and grain-loops are investigated during the deformation process until reaching the failure. The second-order work is once again taken into account to elucidate the local aspect that governs the failure, taking place at the particle scale.

The collapse of the discrete specimen when it turns from quasi-static to dynamic regime is accompanied with a burst in kinetic energy. This rise of kinetic energy occurs when the internal stress cannot balance with the external loading when a small perturbation is added to the boundary, resulting in a difference between the internal and external second-order works of the system. The mesostructures have a symbiosis relationship with each other and their evolution decides the macroscopic behavior of the discrete system. The distribution of the collapse of force-chain correlates with the vanishing of the second-order work at the grain scale.

The mesostructures play an important role in the instability of granular media. The second-order work can be used as an effective criterion to detect the instability of the system on both the macroscale and microscale (grain scale).

Keywords:

Second-order work, failure, discrete element modelling, force-chain, grain-loop, microstructure, mesostructure

Résumé

Les matériaux granulaires se composent de grains solides et d'un constituant remplissant les pores, tel qu'un fluide ou une matrice solide. Les grains interagissent au travers de répulsions élastiques, auxquelles s'ajoutent des mécanismes de friction, d'adhérence et d'autres forces surfaciques. La sollicitation externe conduit à la déformation des grains ainsi qu'à des réarrangements de particules. Les déformations des milieux granulaires sont d'une importance capitale dans de nombreuses applications industrielles et dans la recherche, comme par exemple dans la métallurgie des poutres ou en mécanique des sols. La réponse des matériaux granulaires sous chargement externe est complexe, en particulier lorsqu'une rupture se produit: le mode de rupture peut être diffus ou localisé, et l'aspect de peut varier drastiquement lorsque celui-ci ne peut plus soutenir la charge externe.

Dans le cadre de cette thèse, une analyse numérique basée sur une méthode des éléments discrets est réalisée pour étudier les comportements macroscopique et microscopique des matériaux granulaires à la rupture. Ces simulations numériques prennent en compte le critère du travail du second ordre afin de prédire la rupture. De plus il est montré que l'annulation du travail du second ordre coïncide avec la transition d'un régime statique vers un régime dynamique. Ensuite, le comportement matériaux granulaires est analysé à l'échelle micro-structurelle. L'évolution des chaines des forces et des cycles des grains est étudiée durant le processus de déformation jusqu'à la rupture. Le travail du second ordre est également pris en compte pour examiner l'aspect local qui régit la rupture à l'échelle locale.

L'effondrement de l'échantillon discret quand il passe du régime quasi-statique vers le régime dynamique est accompagné d'une bouffée d'énergie cinétique. Cette augmentation de l'énergie cinétique est générée lorsque la contrainte interne ne permet pas d'équilibrer la force externe sous l'action d'une petite perturbation, ce qui entraîne une différence entre les travaux du second ordre interne et externe du système. Les mésostructures démontrent une relation symbiotique entre elles, et leur évolution gouverne le comportement macroscopique du système discret. La distribution de l'effondrement des chaînes de forces est parfaitement corrélée avec l'annulation du travail du second ordre à l'échelle de particules.

Les mésostructures jouent un rôle important dans l'instabilité des milieux granulaires. Le travail du second ordre peut être utilisé comme un critère pertinent et

robuste pour détecter l'instabilité du système que ce soit à l'échelle macroscopique ou microscopique (échelle de particule)

Mots clés

Travail du second ordre, rupture, modélisation par éléments discrets, chaîne de forces, cycle des grains, microstructure, mesostructure

Contents

Declaration of Authorship ii

Remerciement v

Abstract vii

Résumé ix

Contents xi

List of Figures xv

List of Tables xix

Symbols xxi

1 General introduction 1
- 1.1 General contexts . . . 1
- 1.2 (In)Stability and failure in granular media . . . 2
  - 1.2.1 Definition of stability by Lyapunov . . . 3
  - 1.2.2 Stability criterion of Drucker . . . 4
  - 1.2.3 Stability at the global scale: Hill's criterion . . . 4
  - 1.2.4 Stability at the local scale: the second-order work . . . 6
  - 1.2.5 Failure modes in granular materials . . . 7
- 1.3 Granular materials and DEM . . . 8
- 1.4 Mesostructures in granular materials . . . 9
- 1.5 Objective of the thesis . . . 11
- 1.6 Content of the thesis . . . 11

2 Introduction to discrete element modeling 15
- 2.1 Discrete Element Method . . . 15
  - 2.1.1 The open-source software YADE . . . 16
  - 2.1.2 DEM background . . . 17
- 2.2 Convergence conditions . . . 20

2.2.1 Time step . . . 20
2.2.2 Damping . . . 21
2.3 Simulation of the triaxial/biaxial test . . . 21
2.3.1 Form of grains and contact detection . . . 22
2.3.2 Boundary Conditions . . . 26
2.3.3 Specimen preparation . . . 28
2.3.4 Properties of the 3D numerical specimen . . . 29
2.3.4.1 Grains size distribution . . . 30
2.3.4.2 Contact orientations distribution . . . 31
2.3.5 Void ratio e and coordination number Z . . . 32
2.3.6 Simulation of the classical triaxial test . . . 33
2.4 Calibration of the numerical specimen . . . 35
2.5 Conclusion . . . 36

3 Kinetic energy and diffuse failure mode in granular materials 37
3.1 Diffuse failure mode in granular materials . . . 37
3.2 The continuum approach . . . 40
3.2.1 Kinetic energy and second-order work . . . 40
3.2.2 Series expansion approach . . . 44
3.2.3 Integral approach . . . 45
3.3 Numerical inspection . . . 45
3.3.1 Drained triaxial test . . . 46
3.3.2 Undrained triaxial test . . . 52
3.4 Conclusion . . . 57

4 Mesostructures & macroscopic behaviour of granular materials 59
4.1 Mesostructures in granular materials . . . 59
4.1.1 2D numerical specimen . . . 59
4.1.2 Force-chain and grain-loop . . . 62
4.1.2.1 Definition of force-chain . . . 64
4.1.2.2 Definition of grain loops . . . 68
4.1.2.3 Relation between force-chains and grain-loops . . . 70
4.2 Correlation between the variation of mesostructures and macroscopic behavior of granular materials . . . 71
4.3 Instability of force-chains in granular material . . . 73
4.3.1 Definition of force-chain buckling . . . 73
4.3.2 Correlation between the evolution of force-chains and macroscopic behaviour . . . 75
4.4 Relation between the existence of force-chains and attached grain-loops . . . 77
4.4.1 Lifespan of force-chains and attached grain-loops . . . 78
4.5 Buckling of force-chains and local void ratio . . . 85
4.6 Conclusion . . . 87

5 Instability of mesostructures: second-order work investigation 89

5.1 Introduction 89
5.2 Linking macroscopic and microscopic scales 91
5.3 Numerical validation of the second-order work at the contact scale: the 3D case 94
5.3.1 Stress probe and strain probe simulation 94
5.3.2 Vanishing of the second-order work and instability cones . . 97
5.3.3 Result of the numerical validation 98
5.4 Contact c^- and buckling of force-chains 100
5.5 Microscopic second-order work and instability of attached grain-loops 107
5.6 Conclusion 111
5.7 Appendices 112

6 Conclusions and perspectives **115**

Bibliography **119**

List of Figures

1.1 Examples of failure modes of sands: drained triaxial test with a dense specimen (a), average dense sand (b), loose sand (c) (Desrues [2004]); collapse of sand specimen in undrained triaxial test when a small pertubation is applied after the stress peak (d)(Servant et al. [2005]) . . . 8
1.2 Force-chains and grain-loops in the 2D specimen . . . 10

2.1 Contact laws governing the interactions (Cundall and Strack [1979]) 16
2.2 Positions of two particles in contact (Hadda et al. [2013]) . . . 17
2.3 Simulation loop in DEM modeling . . . 18
2.4 Computations sequence within a DEM time step (O'Sullivan [2011]) 20
2.5 Cubic specimen - geometrical settings . . . 22
2.6 Macroscopic friction angle in terms of microscopic friction angle, results from Mahboubi et al. [1996] and Chareyre [2003] , assembled by Sibille [2006a], with n is the porosity of the specimen . . . 23
2.7 Examples of the refinement of geometrical model of grains: (a) 2-particles clumps (Chareyre [2003]), (b) ellipsoid (Bonilla [2004]), (c) polygonal (Alonso-Marroquın [2004]) . . . 23
2.8 "Hard sphere" and "Soft sphere" contact models in DEM . . . 24
2.9 Overlap between two particles in contact . . . 25
2.10 Preparation of numerical 3D specimen . . . 29
2.11 3D numerical specimen in YADE . . . 30
2.12 The grading curve of the generated sample . . . 31
2.13 Isotropy of the distribution of contact orientations of the specimens: (a) dense, (b) loose in three planes "12", "23" and "13" (See Figure 2.5 for the definition of the axis 1, 2 and 3) . . . 32
2.14 Essential results of the numerical triaxial test . . . 34
2.15 Experimental curves Royis and Doanh [1998] and numerical results from Calvetti et al. [2003] and the YADE Code . . . 36

3.1 Cubic specimen - geometrical settings . . . 40
3.2 Flow chart of the general simulation . . . 46
3.3 Evolution of deviatoric stress q in terms of axial strain of the drained triaxial test . . . 47
3.4 The additional force applied on the top-plate after stabilization . . . 48
3.5 Time evolution of axial strain and kinetic energy after the application of Δs . . . 48

3.6 Evolution of both internal stress σ_1 and applied stress s_1 49
3.7 Computation of the kinetic energy from the second-order work equation 50
3.8 Kinetic energy E_c - Series expansion approach 51
3.9 Kinetic energy E_c - Integral approach 51
3.10 Deviatoric stress in terms of axial strain ε_1 and mean stress p. The point B at which the additional load is applied is indicated. 53
3.11 Axial strain and kinetic energy after the application of Δs 54
3.12 Internal stress σ_1 and applied stress s_1 54
3.13 Computation of the kinetic energy E_c from the second-order work equation 55
3.14 Kinetic energy E_c - Series expansion approach (zoom to short time increments) 56
3.15 Kinetic energy E_c - Integral approach (zoom to short time increments) 56

4.1 The 2D model in YADE 60
4.2 The contact law of the interaction between the disks 60
4.3 Result of the drained biaxial test: deviatoric stress versus axial strain ε_1 61
4.4 Result of the drained biaxial test: volumetric strain ε_v versus axial strain ε_1 62
4.5 Force-chains and grain-loops in the 2D specimen 63
4.6 Force network in 2D specimen (particles are hidden) 64
4.7 Direction of the most compressive principal stress of a particle in a force-chain, θ is defined in equation (4.4) (Peters et al. [2005]) . . . 66
4.8 Directions of the minor principal stresses of particles that can not form a force-chain (a) and can form a force chain (b) 67
4.9 Force-chains in 2D specimen (particles marked with dark blue color) 68
4.10 Definition of grain loops L-3 (a), L-4 (b), L-5 (c) and L-6 (d) 68
4.11 Comparison between the deviatoric stress q and the total number of force-chains in the biaxial test 71
4.12 Volumetric strain ε_v and the variation of the number of grain loops 72
4.13 Calculation of the buckling angle θ_b in the 3-particle segment in a force-chain. If this buckling angle exceeds the threshold, the force-chain is considered as buckling. 73
4.14 Numbering of buckling events during the biaxial test 74
4.15 Variation of kinetic energy E_c and evolution of buckling events during the biaxial test 76
4.16 Force-chain (particles marked with dotted pattern) with attached grain-loops 78
4.17 Evolution of β_3 versus the normalized lifespan of force-chains 79
4.18 Evolution of β_6 versus the normalized lifespan of force-chains 80
4.19 Phases in the drained biaxial test: hardening, softening and ultimate 81
4.20 Evolution of β_3 (left) and β_6 (right) of the force-chains in the hardening phase (zoom) 82

4.21 Evolution of β_3 (left) and β_6 (right) of the force-chains in the softening phase (zoom) . . . 82
4.22 Evolution of β_3 (left) and β_6 (right) of the force-chains in the ultimate phase (zoom) . . . 83
4.23 Variation of β_3 and β_6, compared separately in 3 phases . . . 84
4.24 Local area used to calculate the void ratio around the buckling grain 85
4.25 Comparison of the local void ratio between the *buckling zone* and *non-buckling zone* . . . 86

5.1 Cubic specimen - geometrical settings . . . 91
5.2 Definition of particles in contact (Nicot et al. [2012a]) . . . 92
5.3 Definition of the Rendulic plan: stress probe and strain probe (left) and the response of the system (right) (Hadda et al. [2013]) . . . 95
5.4 Deviatoric stress versus axial strain and the 3 states where the probing test is carried out . . . 96
5.5 Volumetric strain versus axial strain and the 3 states where the probing test is carried out . . . 96
5.6 The normalized second-order work from the strain probe test mentioned in Section 5.3.1 . . . 97
5.7 Comparison between W_2 and W_2^m at point A . . . 99
5.8 Comparison between W_2 and W_2^m at point B . . . 99
5.9 Comparison between W_2 and W_2^m at point C . . . 100
5.10 Three considered states $\varepsilon_1 = 0.1\%$, $\varepsilon_1 = 2\%$ and $\varepsilon_1 = 6\%$ . . . 101
5.11 Relative displacement field ΔU_x at (a): $\varepsilon_1 = 0.1\%$, (b): $\varepsilon_1 = 2\%$ and (c): $\varepsilon_1 = 6\%$ . . . 102
5.12 Relative displacement field ΔU_y at (a): $\varepsilon_1 = 0.1\%$, (b): $\varepsilon_1 = 2\%$ and (c): $\varepsilon_1 = 6\%$ . . . 102
5.13 Distribution of contacts c^- at (a): $\varepsilon_1 = 0.1\%$, (b): $\varepsilon_1 = 2\%$ and (c): $\varepsilon_1 = 6\%$ . . . 103
5.14 Distribution of force-chains at (a): $\varepsilon_1 = 0.1\%$, (b): $\varepsilon_1 = 2\%$ and (c): $\varepsilon_1 = 6\%$ . . . 103
5.15 Distribution of buckling grains at (a): $\varepsilon_1 = 0.1\%$, (b): $\varepsilon_1 = 2\%$ and (c): $\varepsilon_1 = 6\%$ . . . 104
5.16 Zoom to the sample. Red dots demonstrate contacts c^-, green particles are buckling grains, dark blue grains are particles belonging to force-chains . . . 104
5.17 Definition of the scanning zone around the buckling grain . . . 106
5.18 Average magnitude of the vanishing second-order work around the buckling grains . . . 107
5.19 Decompostion of a grain-loop *L-3* into 3 contacts . . . 108
5.20 Comparison between the second-order work for loop L-3 and L-6 in the biaxial test . . . 109
5.21 Comparison between the second-order work for attached loop *L-3a* and *L-6a* in biaxial test . . . 110

5.22 Summary of the distribution of contacts c^- in the drained biaxial test of the dense specimen 112
5.23 Summary of the distribution of force-chains in the drained biaxial test of the dense specimen 113
5.24 Summary of the distribution of buckling grains in the drained biaxial test of the dense specimen 114

List of Tables

2.1 Numerical parameters 30
2.2 Comparison of the parameters of the numerical models 35

3.1 Numerical parameters 46

4.1 Model parameters 61

Symbols

a	distance	m
k_n	normal stiffness	Pa
k_t	tangential stiffness	Pa
W_2	second-order work	J
D_s	sphere's diameter	m
φ_c	microscopic friction angle	$^\circ$
$\boldsymbol{\varepsilon}$	Eulerian strain tensor	-
$\boldsymbol{\sigma}$	Eulerian stress tensor	-
$\boldsymbol{\Pi}$	Piola-Kirchhoff stress tensor	-

Dedicated to my parents, sister, brother and Jellyfish

Chapter 1

General introduction

1.1 General contexts

In mountainous regions, natural catastrophic accidents, such as landslides or avalanches often cause great loss to humanity, both in economy and social safety. In order to avoid these problems, researches have been carried out to investigate and better define these natural phenomena, so methods of predicting and preventing can be realized afterward. It is very important to understand when and why the failure occurs.

In particular, for granular materials, the behaviour of the system on the macroscale is mainly defined by structures which are on the microscale. To anticipate failures of the material on the macroscopic scale, the investigation can be carried out at smaller scale, which is in the scope of this thesis: to consider the general case of the failure occurring in granular materials and to investigate the role of microstructures to the macroscopic behaviour of granular materials.

To understand these problems, numerical simulations using discrete elements method are put into execution to verify the relevance of failure criteria and instabilities. Furthermore, more detailed numerical analyses at a smaller scale are taken into account, in order to understand the behaviour of microstructures in granular assemblies just before and during the failure of the material.

1.2 (In)Stability and failure in granular media

Normally for a non-viscous material, its behavior can be described by the Cauchy stress tensor $\boldsymbol{\sigma}$ and the small strain tensor $\boldsymbol{\varepsilon}$, such that:

$$\dot{\boldsymbol{\sigma}} = \boldsymbol{M}\dot{\boldsymbol{\varepsilon}} \tag{1.1}$$

When $\boldsymbol{M}$ is positive definite, it exists a unique solution $\dot{\boldsymbol{\varepsilon}}$ for a loading condition $\dot{\boldsymbol{\sigma}}$. Classically, a failure state is described as a limit stress state. Such condition is given by the relation:

$$det(\boldsymbol{M}) = 0 \tag{1.2}$$

which is also called the plasticity limit condition.

For associated materials (also known as standard materials) this condition gives good predictions of failure. In fact when this condition is matched, the stress rate $\dot{\boldsymbol{\sigma}}$ is nil for a strain rate $\dot{\boldsymbol{\varepsilon}}$ not nil. Nevertheless it has been proven, experimentally and theoretically that this last condition is not sufficient for non-associated materials.

As an example, Desrues and Viggiani [2004] demonstrated, by experimental works, for the sand, the failure by strain localization (appearance of the shear band) can occur before the limit of plasticity. The strain localization by the shear band is detected by the vanishing of the determinant of the acoustic tensor, such that (Rice [1976], Rudnicki and Rice [1975]) :

$$det(\boldsymbol{n}\boldsymbol{M}\boldsymbol{n}) = 0 \tag{1.3}$$

where $\boldsymbol{n}$ is the normal vector to the band. This criterion allows us to detect some particular failures which can occur inside the limit of plasticity. However this criterion is relevant to describe the failure in localized mode. Unfortunately, in granular materials we also observe failure in diffuse mode, which is not detectable for $det(\boldsymbol{n}\boldsymbol{M}\boldsymbol{n}) = 0$. Therefore we need to use another failure criterion.

In this thesis, we use the vanishing of the second-order work as a criterion to detect instabilities of granular materials, known as Hill's criterion, explained in below sections.

1.2.1 Definition of stability by Lyapunov

It is necessary to revisit the definition of stability initially introduced by Lyapunov [1907]. This theory destines to the study of the movement of a mechanical system having a finite number of degrees of freedom and is described by time dependent functions. The movement of the system is considered stable if a small perturbation of initial conditions (position or velocity) does not increase indefinitely over time but remains limited instead. As pointed out by Chambon et al. [2004], this definition can be applied to an equilibrium state in the way that this equilibrium state is a particular case of movement to which the positions at any instant t correspond to the initial position.

Darve and Laouafa [2000] propose an extension to the definition of Lyapunov in the context of continuum mechanics: "For a non-viscous material and a given loading history, a stress-strain state is considered stable if for all small loading variations, the response of the system is small", such as:

$$\forall \epsilon > 0 \quad \exists \eta = \eta(\epsilon) \quad \text{such that} \quad \|ds\| < \eta \Rightarrow \|dr\| < \epsilon \tag{1.4}$$

Thus, all the limit stress state, commonly called failure states are unstable following Lyapunov theory. Similarly, the peak of q and all the descending branches of the curve representing the behavior of the undrained test of a loose sand in the $q-p'$ diagram are unstable following Lyapunov, since a small addition to the axial force causes the collapse of the specimen (Chapter 3).

Di Prisco and Imposimato [1997] propose an application of Lyapunov's definition to granular materials by taking into account the microstructure to explain their observation of collapse of materials. For this purpose, they consider that each micro-configuration of grains is a point of a body. Each of these points is connected biuniquely to a defined point in space whose coordinations are the state variables (for example the relative density or the texture tensor). By using a mathematical

definition of distance in this space of variables of state Di Prisco and Imposimato [1997] sets out the following criterion:

"A granular system is defined as stable, when the distance between the starting and the finishing point, defined in the state variable space, continuously decreases in direct proportion to the decrease in the size of the load disturbance, of whatever kind it may be."

However, we do not know any practical applications based on this definition.

1.2.2 Stability criterion of Drucker

The criterion of stability by Drucker [1957] is described below:

"The displacement of the body will change as added force is applied and equilibrium is maintained. It was postulated that the work done by the external agency during the application of force must be positive and over a cycle of application and removal, positive or zero, zero only when purely elastic changes take place. In such a cycle, work cannot be extracted from the system of the body and the set of forces acting upon it."

For a non-viscous material, this criterion is written as:

$$\dot{\boldsymbol{\sigma}} : \dot{\boldsymbol{\varepsilon}}^p > 0 \qquad \forall \dot{\boldsymbol{\varepsilon}}^p \neq 0 \tag{1.5}$$

where $\dot{\boldsymbol{\varepsilon}}^p$ is the plastic strain rate. Drucker precises that this postulate requires a linear incremental stress-strain relation, and an associated flow rule. Mandel [1966] also shows that the Drucker postulate can be violated when the Coulomb internal friction is considered.

1.2.3 Stability at the global scale: Hill's criterion

For a solid volume V in the steady state, supposed that a part of the boundary is fixed and other part of the boundary is only under actions of dead loading. Following Hill [1958], a system is considered unstable if when being under a small load perturbation, the deformation may continue infinitesimally without any supply of external energy.

Hill's criterion is expressed as (Hill [1958]):

$$\int_V \dot{s}_{ij} \frac{\partial \dot{U}_j}{\partial x_i} dV > 0 \tag{1.6}$$

where $\dot{s}_{ij}$ is the rate of the nominal stress tensor, $\frac{\partial \dot{U}_j}{\partial x_i}$ is the kinematically admissible velocity field associated with $\dot{s}_{ij}$.

A more classical form can be adopted to describe the Hill's criterion. The second-order work (Hill [1958]) can be expressed through the material description (Lagrangian formalism) such that:

$$W_2 = \int_{V_0} \delta \boldsymbol{\Pi}_{ij} \delta \boldsymbol{F}_{ij} dV_0 \tag{1.7}$$

In the case of small deformation and that geometric effect can be negligible, the Hill's stability condition can be expressed by the Cauchy stress tensor as below (Nicot et al. [2007]):

$$W_2 = \int_V \delta \boldsymbol{\sigma}_{ij} \delta \boldsymbol{\varepsilon}_{ij} dV \tag{1.8}$$

where $\boldsymbol{\Pi}$ is the first Piola-Kirchoff stress tensor, $\boldsymbol{F}$ is the general term of deformation gradient, $\boldsymbol{\sigma}$ is the Cauchy stress tensor and $\boldsymbol{\varepsilon}$ is the strain tensor.

In both description, the second-order work is associated to the incremental variation of two quantities $\delta \Pi_{ij}$ and δF_{ij} or $\delta \sigma_{ij}$ and $\delta \varepsilon_{ij}$ relating to the constitutive behavior of the granular material with the initial volume V_0 and the volume V of the current configuration.

Another study by Osinov and Wu [2005] mention about this criterion from the same test by considering at first a quasi-static strain perturbation and then a dynamic perturbation by applying a velocity field. The study manages to show that, under a quasi-static regime,the equilibrium state requires an external application of energy, and the sign of this received energy corresponds to the sign of $\int_V \dot{\boldsymbol{\sigma}} : \dot{\boldsymbol{\varepsilon}} dV$. In the dynamic case, Osinov and Wu [2005] introduce the kinetic energy K_c and show that at the initial moment of the application of the perturbation, we have:

$$\frac{d^2K_c}{d^2t} = -\int_V \dot{\boldsymbol{\sigma}} : \dot{\boldsymbol{\varepsilon}}\ dV \tag{1.9}$$

Also, the Hill's condition is verified as the kinetic energy diminishes rapidly after the application of the perturbation.

It is worth noting that, similar to what expressed in Equation 1.9, Nicot et al. [2007] confirms that the positiveness of the Hill's criterion is considered as a stability condition, both in quasi-static and in dynamic case.

1.2.4 Stability at the local scale: the second-order work

The local stability, also stated as material stability (Hill [1958]), is based on the notion of instability which can be developed from a material point in continuous medium (Bigoni [2000]). This stability condition can be derived from the global form (Equation 1.6) and it relates to the sign of the second-order work W_2.

Following Hill, a material element is defined stable if the positive condition of the second-order work is verified:

$$W_2 = \dot{\boldsymbol{\sigma}} : \dot{\boldsymbol{\varepsilon}} > 0;\ \forall \dot{\boldsymbol{\varepsilon}} \neq 0 \tag{1.10}$$

It is worth noting that the global stability (Equation 1.6) of a solid volume V is satisfied if the condition in Equation 1.10 is satisfied at every point in the volume V (Bigoni and Hueckel [1991]). Moreover, for the homogeneous case, these two conditions (1.6) and (1.10) coincide.

In general, the link between the stability condition of Lyapunov [1907] and Hill's condition is not clear (Osinov and Wu [2005]). On the other hand, Koïter [1969] manages to demonstrate the equivalence between them in elastic case. The agreement between the positiveness of the second-order work and the uniqueness of the solution is also validated at some constitutive relations (Bigoni [2000], Bigoni and Hueckel [1991]).

For the non-associated materials, Chambon and Caillerie [1999] prove that the positiveness of the second-order work at each solid point implies the uniqueness condition of Hill [1958] given by:

$$\int_V \delta\dot{\boldsymbol{\sigma}} : \delta\dot{\boldsymbol{\varepsilon}}\, dV > 0, \forall\dot{\varepsilon} \tag{1.11}$$

where δ is the difference between two admissible fields. Raniecki [1979], Raniecki and Bruhns [1981] also proves this point for hypo-elastic relations. However, Valanis [1985] showed that the uniqueness can be verified even if the sign of the second-order work is negative.

1.2.5 Failure modes in granular materials

The notion of failure can be encountered in many fields. This notion is essential in material sciences where failure can be investigated at the specimen scale. In geomechanics, usually it is assumed that failure occurs whenever a material specimen is no longer able to sustain any deviatoric load increment. This condition is associated with a sudden change in the specimen microstructure, namely the sharp decrease in the number of grain contacts. The significant increase in the number of degrees of freedom implies the possibility of rapid relative displacements between grains, leading in some cases to the collapse of the specimen.

Failure: we consider the failure of a material when a small increment of loading leads to a large strain within the specimen. The appearance of a peak (or a plateau) on the *deviatoric stress - axial strain* curve obtained from a drained triaxial test applying on a dense (or loose) sample is considered as an example of a state of failure. In this manuscript, the term **collapse** is also used to describe a failure of the granular material where the strain increases very largely in a very short time period (see Chapter 3).

For geomaterials, several failure modes can occur within the plastic limit surface. From a mathematical point of view, this feature is essentially related to the non symmetry of the tangent constitutive tensor. Two specific modes of failure can be defined: the localized mode and the diffuse mode.

- In the *localized* mode, the strain is concentrated in one (or multiple) shear band(s), the displacement field is highly heterogeneous and organized.
- The *diffuse* failure mode is characterized with the absence of any form of localization within the specimen, the displacement field is chaotic, without any apparent organization.

Starting from the classical drained triaxial test applying to a dense homogeneous soil specimen, as an example, the localized failure mode generally occurs nearly at the peak of the deviatoric stress q (plotted in terms of the axial deformation ε_1) (Figure 1.1 (a, b, c)).This mode of failure is identified with the appearance of the shear band (one shear band or multiple shear bands). It is also noticed that the localized failure can occur before the plastic limit condition.

The diffuse failure mode can be found in the undrained triaxial test applying on a loose specimen. In this test, the deviatoric stress q (plotted in terms of the average stress p) reaches a peak. After this peak, if the specimen is strain-controlled, the test can continue until the deviatoric stress is nil (the applied strain rate is constant). This case corresponds to the static liquefaction. However, if the loading is stress-controlled or if a small perturbation is added after the deviatoric stress peak, this can lead to the collapse of the specimen (Figure 1.1 (d)). This phenomenon corresponds to the diffuse failure without any sign of localization.

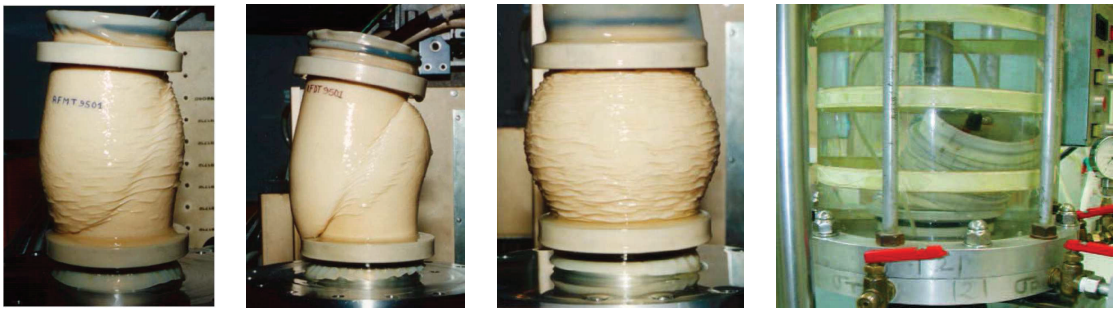

FIGURE 1.1: *Examples of failure modes of sands: drained triaxial test with a dense specimen (a), average dense sand (b), loose sand (c) (Desrues [2004]); collapse of sand specimen in undrained triaxial test when a small pertubation is applied after the stress peak (d)(Servant et al. [2005])*

1.3 Granular materials and DEM

Granular materials are of great importance in civil engineering or in manufacturing processes whether they are granular soils in nature or raw materials for industries. Because of their discontinuous nature, the behaviour of such materials is complex and it is not trivial to carry out their modelling.

As an important part of several engineering applications, lots of studies have been carried out to understand their behavior and properties, especially in soil mechanics. Nowadays with the help of modern and powerful computer, we can simulate them using the DEM (Discrete Element Method) from classical tests in laboratory like the triaxial test to the more complex one like the corrosion happening in a huge dam... These kinds of simulations provide a robust and flexible way of research, also they can provide realistic results.

DEM is nowadays recognized as a research tool across a number of fields. Interest in DEM is rising rapidly and assessing the state of the art of DEM used in geomechanics is difficult as the situation is rapidly changing. The robust information to the particle scale that we can receive from DEM allows us to go deeply into details of micromechanics of granular materials. Micromechanics deals with the relationship between external stresses and strains, using internal information such as average internal forces and displacements. This approach requires complete information of all characteristics such as contact forces, average microscopic geometry, contacts distribution and coordination number for all elements in the assembly (O'Sullivan [2011], Thompson et al. [2004]). Consequently, failures of granular materials in general (or soils in particular) can be simulated and investigated, which draw huge interest for both academic research and applied civil engineering.

1.4 Mesostructures in granular materials

Granular materials are built with grains having interactions with each other. The arrangement of particles, and the distribution of contact forces as well can form different kinds of structures in the medium. For example, the strong contact forces between particles can form a sort of linear pattern, corresponding to the so-called force-chain, or more particularly in 2D case, the particles in contact can form a close polygon and create the grain-loop. Figure 1.2 displays force-chains and grain-loops within a 2D specimen. These two are the essential structures inside the granular medium.

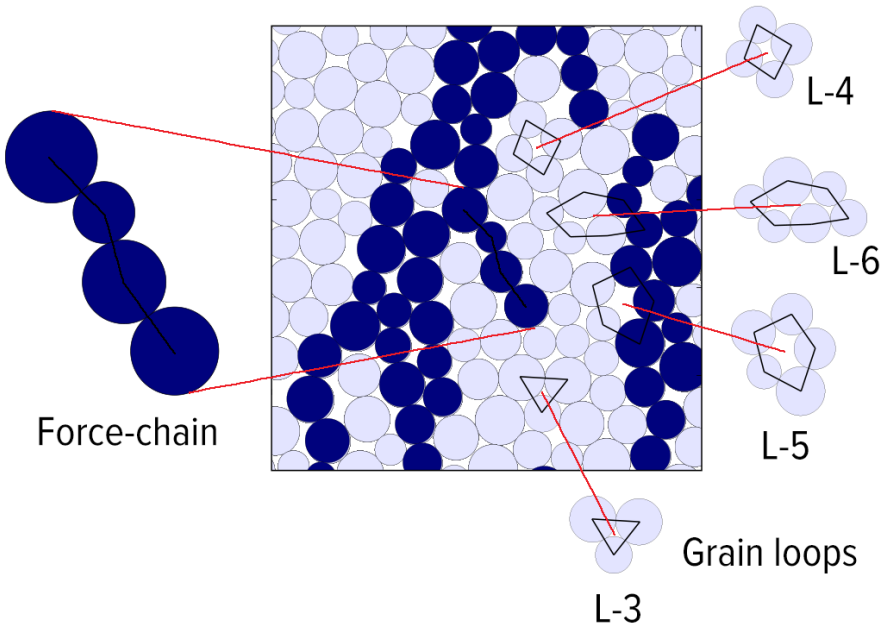

FIGURE 1.2: *Force-chains and grain-loops in the 2D specimen*

The contact forces inside granular materials can be distinguished into strong and weak force networks. The strong force network, which is directly connected to the capacity of the specimen to sustain external load, can be characterized by geometry conditions and therefore the so-called *force-chain* is introduced. The macroscopic behavior of the specimen is strongly related to the distribution of force-chains and the instability of force-chains.

Grain-loops (in 2D case) are known to contribute to granular stability and have inspired new approaches to understanding the stress responses of granular matter (Smart and Ottino [2008], Tordesillas et al. [2010a]). The idea of 2D grain-loops is simple but it is very important as it can be seen everywhere, not only granular materials: from real life problem like stacking fruits on the shell, to topological researches. More and more researchers pay attention to this structure to the behaviour of granular materials (Tordesillas et al. [2010a], Walker and Tordesillas [2010]). However there are still many unanswered questions concerning grain-loops. Which size of the grain-loop matters the most? What decides the stability of grain-loops? What is the contribution of grain-loops to other mesostructures? Those are the issues that this thesis tries to resolve.

Force-chains and grain-loops are defined as the mesostructures in granular materials in the scope of this thesis. For a particular case like the drained biaxial test of a dense specimen, the variation of mesostructures affects directly the macroscopic

behaviour of the system: the variation of the number of force-chains and the number of grain-loops to the deviatoric stress and the volumetric strain, respectively. When the failure of the material occurs (known as the appearance of the shear band in the specimen), the distribution of the collapse of force-chains (buckling of force-chains) and the spatial disposition of grain-loops change accordingly (as discussed in Chapter 4). Furthermore, inside the world of mesostructures, force-chains and grain-loops also rely on each other and create a complex relation. This thesis shows an attempt to elucidate these problems and widen the understanding about granular matter from the particle scale.

1.5 Objective of the thesis

The study presented in this thesis is realized by series of numerical DEM simulation of classical triaxial tests (for the 3D case) and biaxial tests (for the 2D case), in order to investigate these principal issues:

- Validating the relation between the evolution of kinetic energy and the second-order work calculated from the stress and deformation measured from the boundary. This investigation points out the influence of the loading path and the control parameter on the failure nature (effective or non-effective) and the failure mode (diffuse or localized).
- Finding the role of force-chains and grain-loops in the instability of granular materials, and what is the relation between force-chains and grain-loops.
- Linking the macroscopic second-order work (specimen scale) and microscopic second-order work (particle scale) to investigate instability on the mesostructure scale (force-chains and grain-loops).

1.6 Content of the thesis

In this thesis, series of numerical simulation are carried out, with the help of the Discrete Element Method (DEM). The considered problems are categorized into following sections:

- The first two chapters are the general introduction and the presentation of the discrete element method, giving the context and the basis of the numerical tool in the scope of this thesis. In Chapter 2, the process of the numerical specimen preparation and validation is also presented.

- Chapter 3 studies the failure of granular materials (in 3D case). The purpose of this section is to verify the relation between the development of kinetic energy with the macroscopic second-order work calculated from the boundary of the system. The second-order work is introduced in the context of the bifurcation theory, to detect occurrence of the failure of the system.

- In Chapter 4, investigations about the meso-structures in the granular media, including the force-chains and the grain-loops, are considered for the 2D case. These two structures play a basic and an important role to the macroscopic behavior of the system. Also, their instability shows a close correlation with the failure of the sample. Furthermore, a mutual relationship between force-chains and grain-loops is pointed out.

- The last Chapter 5 investigates instabilities of mesostructures (in 2D case) by using the microscopic second-order work. The second-order work is proven to be a condition for the failure of the system to occur. First, this chapter tries to elucidate the correlation between the collapse of force-chains and the distribution of the vanishing of the microscopic second-order work, by the fact that both of them share the same pattern when the failure occurs in the specimen (the appearance of the shear band). After that, the second-order work of the grain-loops is taken into account to investigate the instability of grain-loops.

- Finally, the conclusion chapter summarizes the thesis and proposes some perspectives and open questions for future developments.

Stability of granular materials is an important branch of research. Researches about failures can help researchers and engineers to predict natural hazards and to propose a method to prevent them to happen. Nowadays thanks to DEM modelling, the behaviour of granular materials including failures, can be simulated realistically, that provides to researchers an efficient tool to study from laboratory tests to real life phenomena.

In particular, it is observed that the failure of sand might happen before the Mohr-Coulomb limit, where the failure mode is diffuse or localized, without any appearance of localization patterns. In the case where the specimen is stress-control in classical drained and undrained triaxial tests, the failure is depicted as a transition from a quasi-static regime to a dynamic regime, the granular medium then totally collapses (the strain rate largely increases), as a result, a burst in kinetic energy is observed.

The discrete elements method also allows us to look deeply into the contact scale inside granular materials. By investigating the behavior of mesostructures and comparing them with the macroscopic behaviour of materials, this thesis tries to understand the role of mesostructures to the development of instability in granular materials.

Furthermore, the second-order work computed from microscopic variables (Nicot et al. [2012a]) is taken into account, considering contact forces and positions of particles, as a link to the macroscopic second-order work. This notion can be expanded to the mesoscale, where the second-order work is used to investigate the instability of grain-loops.

Chapter 2

Introduction to discrete element modeling

2.1 Discrete Element Method

The discrete element method proposed by Cundall and Strack [1979] (hereafter abbreviated DEM) is a very powerful numerical tool to simulate soils and other granular materials. The DEM modeling involves specifying the equations of motion for a system of discrete bodies, and solving the resulting equations. The mechanical response of granular materials in DEM is governed by the contacts between constitutive particles and between particles and the boundaries. So that the physical quantities that control these interactions (particle rotations, contact orientations, contact forces etc.) can easily be measured, which is almost impossible to capture in a laboratory test. The DEM model allows us to look inside the material and understand the fundamental particle interactions underlying the complex, macro-scale response. Moreover, the DEM enables analyzing of the mechanisms involved in large-displacement problems in geomechanics. These problems cannot easily be modeled using more widespread continuum approaches such as the finite element method (FEM). Furthermore, as failure in geomechanics often involves very large displacements or deformations, DEM modeling can therefore provide a convenient framework to investigate failure mechanisms. Consequently, using DEM allows us to mimic the response of granular materials in the real world.

2.1.1 The open-source software YADE

The DEM software YADE (abbreviation of "Yet Another Dynamic Engine", Šmilauer et al. [2010]) is an open-source software, which is developed based on the C++ & Python programming languages. The calculation method is similar to the one proposed by Cundall and Strack [1979], the details of the simulation is fully described in the next paragraphs.

The contact laws governing the interactions between the particles are defined by the parameters illustrated in Figure 2.1

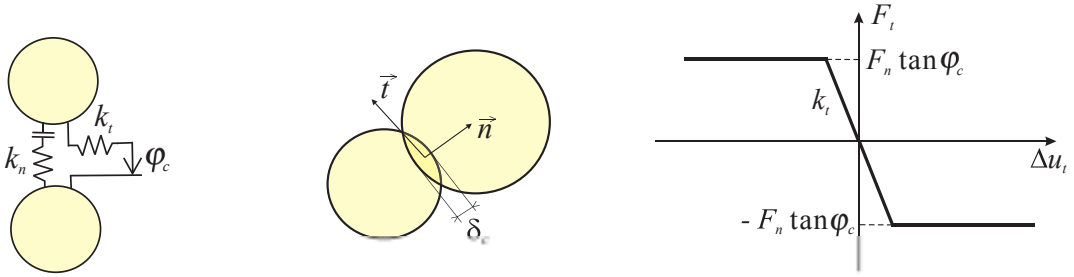

FIGURE 2.1: *Contact laws governing the interactions (Cundall and Strack [1979])*

These parameters include the normal stiffness coefficient k_n (normal direction to the contact plane), the tangential stiffness coefficient k_t (tangent direction to the contact plane) and the microscopic friction angle φ_c. There is no tensile force. The inter-particle contact behaviour in the normal contact direction is governed by an elastic force-displacement relation, as described in equation (2.1):

$$\Delta F_n = k_n \Delta \delta_c \quad \text{and} \quad F_n \geq 0 \tag{2.1}$$

where δ_c is the penetration depth between two particles in contact (Figure 2.2), also known as the subtraction between the sum of two radii and distance between two centers of the particles in contact.

The tangent force F_t is incrementally computed at each time step as described in equation (2.2):

$$\Delta F_t = k_t \Delta u_t \quad \text{and} \quad |F_t| \leq F_n \tan\varphi_c \tag{2.2}$$

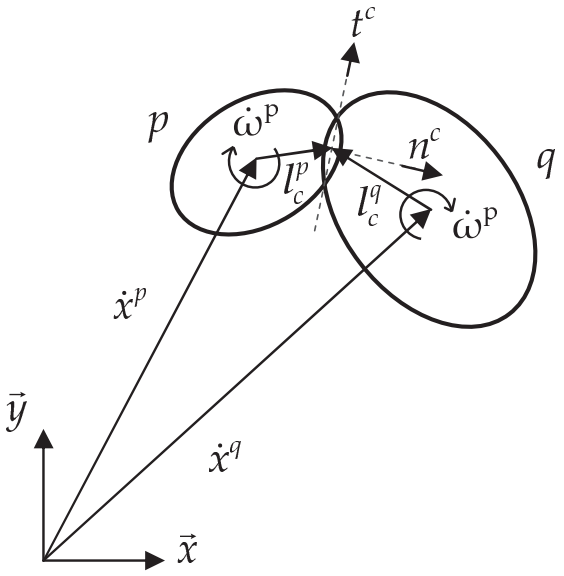

FIGURE 2.2: *Positions of two particles in contact (Hadda et al. [2013])*

For every time step, the tangential component of contact force must be corrected such that it does not exceed the shear strength of the contact. When the normal and tangential components of the contact force are determined based on equations 2.1 and 2.2, they are added to the resultant force and the moment applied on the particles in contact.

2.1.2 DEM background

This section dedicates to the explanation of DEM formulations implemented in the YADE DEM code. The presentation order is the same of what directly happens in the simulation. First, the new interaction happens between two particles, which consists in:

- Detecting collision between two particles
- Creating interaction and computing its properties; they are either precomputed or derived from properties of both particles (Šmilauer et al. [2010])

After that, for existing interactions:

- Strain evaluation

- Stress computation based on strains
- Force application to particles in interaction

The simulation loop in the DEM is demonstrated in the diagram below (Figure 2.3):

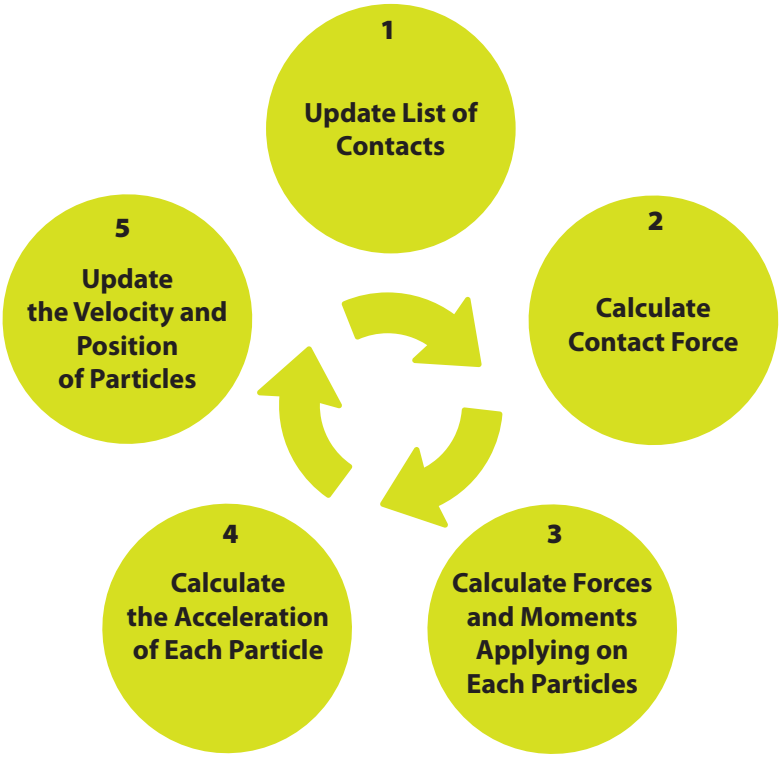

FIGURE 2.3: *Simulation loop in DEM modeling*

Let us consider a particle, its translation movement is defined by its position $\boldsymbol{x}_i$, its velocity $\dot{\boldsymbol{x}}_i$ and its acceleration $\ddot{\boldsymbol{x}}_i$. The rotation of the particle is described by its angular velocity $\dot{\boldsymbol{\omega}}_i$ and its angular acceleration $\ddot{\boldsymbol{\omega}}_i$. The translation movement of the particle therefore reads:

$$\mathcal{F}_i = m\ddot{\boldsymbol{x}}_i \tag{2.3}$$

where m is the mass of the particle.

In a local coordinate system oriented such that it represents the principal axes of the inertia of the particle, the rotation of the particle is described by the equation below:

$$\mathcal{M} = J\ddot{\boldsymbol{\omega}}_i \tag{2.4}$$

where J is the inertia moment of a spherical grain which has radius R ($J = \frac{2}{5}mR^2$).

Suppose that the linear acceleration $\ddot{x}_i$ and the angular acceleration $\ddot{\omega}_i$ are constant in the interval $t - \frac{\Delta t}{2}$ and $t + \frac{\Delta t}{2}$, and by integrating movement equations following a finite difference scheme on the time step Δt, the velocity at the instant $t + \frac{\Delta t}{2}$ is given by:

$$\dot{x}_i^{t+\frac{\Delta t}{2}} = \dot{x}_i^{t-\frac{\Delta t}{2}} + \ddot{x}_i^t \Delta t = \dot{x}_i^{t-\frac{\Delta t}{2}} + \frac{\mathcal{F}_i}{m}\Delta t \tag{2.5}$$

$$\dot{\omega}_i^{t+\frac{\Delta t}{2}} = \dot{\omega}_i^{t-\frac{\Delta t}{2}} + \ddot{\omega}_i^t \Delta t = \dot{\omega}_i^{t-\frac{\Delta t}{2}} + \frac{\mathcal{M}_i}{J}\Delta t \tag{2.6}$$

and new positions and orientations at the instant $t + \Delta t$ is given by:

$$x_i^{t+\Delta t} = x_i^t + \dot{x}_i^{t+\frac{\Delta t}{2}} \Delta t \tag{2.7}$$

$$\omega_i^{t+\Delta t} = \omega_i^t + \dot{\omega}_i^{t+\frac{\Delta t}{2}} \Delta t \tag{2.8}$$

$\mathcal{F}_i^{t+\Delta t}$ and $\mathcal{M}_i^{t+\Delta t}$ for the next loop are determined by using the force-displacement law.

As demonstrated in Figure 2.4 in every time step there are two main series of calculations O'Sullivan [2011]:

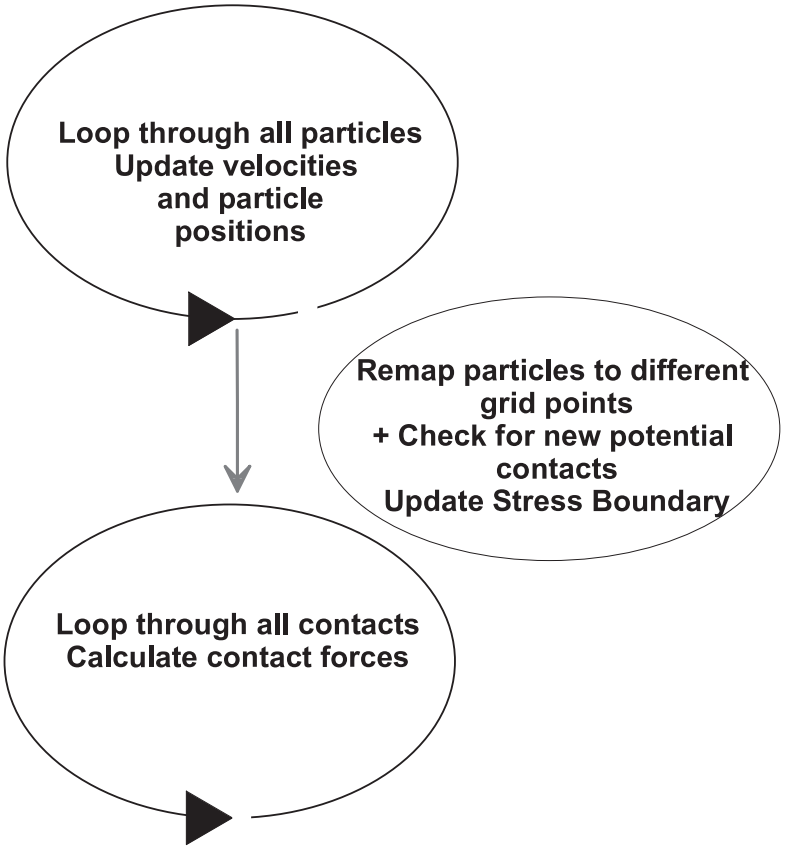

FIGURE 2.4: *Computations sequence within a DEM time step (O'Sullivan [2011])*

2.2 Convergence conditions

2.2.1 Time step

The choice of time step in DEM modeling is very important, it must be estimated carefully to maintain the stability of the numerical solution and avoid the cost of calculation (time consuming).

The convergence of a computation process toward a stable solution is also dependent on the value of the time step for the wave propagation in the medium. If we consider each element in the assembly as a mass oscillator m connected by a spring with the stiffness k to a fixed body, the time step Δt is determined by the period of the oscillation $T = 2\pi\sqrt{\frac{m}{k}}$ in order to avoid the dynamic effect. Consequently, Δt must be smaller than the smallest period obtained from all particles in the assembly.

In YADE software, the critical time step Δt_c is estimated as a fraction C_t of the smallest equivalent period of the assembly T^T (for the translation movement) and T^R (for the rotation):

$$\Delta t_c = C_t \min(T^T, T^R) = C_t \min(\sqrt{\frac{m}{k_n}}, \sqrt{\frac{J}{k_r}}) \tag{2.9}$$

where k_n and k_r are the normal stiffness and the rotation stiffness of interactions applying on each particle, respectively. J is the inertia moment.

2.2.2 Damping

In order to amortize the vibration in the DEM simulation, Cundall and Strack [1979] proposed a global non-viscous damping applying to each particles. This damping system plays two different roles: first, to reduce the resultant force if it is driving and to increase it if it is opposed to the movement. In this system, the damping force at each node (particle) is proportional to the magnitude of the out-of-balance-force with a sign that ensures that the vibrational modes are damped, rather than steady motion. The "out-of-balance-force" is the non-zero resultant force that acts on a particle to cause acceleration. For each particle, a damping force $\mathcal{F}_i^a$ and a damping moment $\mathcal{M}_i^a$ are added, such that:

$$\mathcal{F}_i^a = -\lambda^a |\mathcal{F}_i| \text{sign}(\dot{x}_i) \tag{2.10}$$

$$\mathcal{M}_i^a = -\lambda^a |\mathcal{M}_i| \text{sign}(\dot{\omega}_i) \tag{2.11}$$

where λ^a is the damping coefficient ($\lambda^a \in [0, 1]$). By default, YADE uses $\lambda^a = 0.05$.

2.3 Simulation of the triaxial/biaxial test

The geometrical settings of the specimen used in this manuscript are demonstrated in Figure 2.5

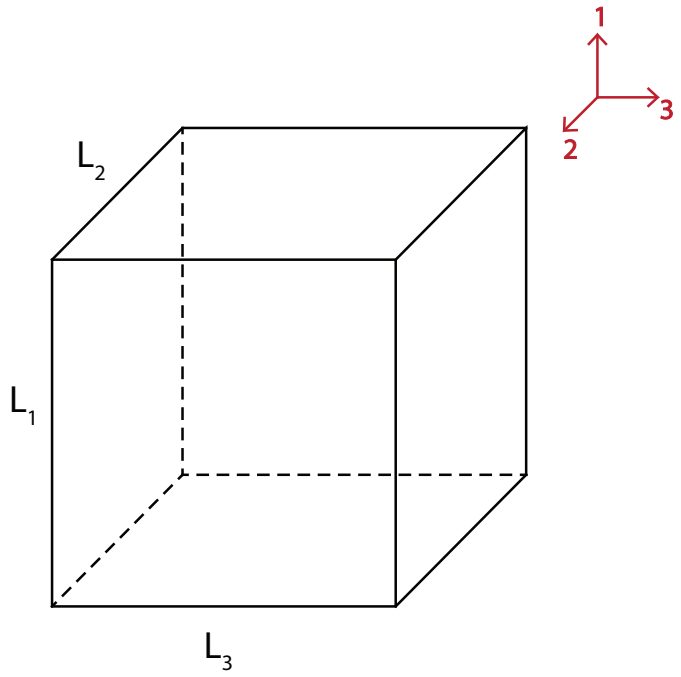

FIGURE 2.5: *Cubic specimen - geometrical settings*

The index direction '1' is the axial direction while '2' and '3' are the lateral directions. In what follows, the discussion focuses mainly on 3D specimen. The configuration and simulation results of the 2D biaxial test are presented in Chapter 4.

2.3.1 Form of grains and contact detection

In classical DEM tool, the form of grains is usually disks (2D case) or spheres (3D case). It is obvious that this form is the easiest for the implementation of contact detection. However, the purpose of using DEM in geomechanics in general is to describe as precise as possible the behaviour of granular materials; the disk or the sphere lead to some issues, especially the macroscopic friction angle at the peak of the deviatoric stress ϕ_{lim}. In fact, the relation between the macroscopic friction angle ϕ_{lim} and the microscopic friction angle φ_c is not linear. It exists a saturation of ϕ_{lim} when φ_c increases limiting the maximum value of ϕ_{lim}. On the contrary, ϕ_{lim} does not vanish with φ_c. This problem is discussed by Sibille [2006a], the comparison is shown in Figure 2.6:

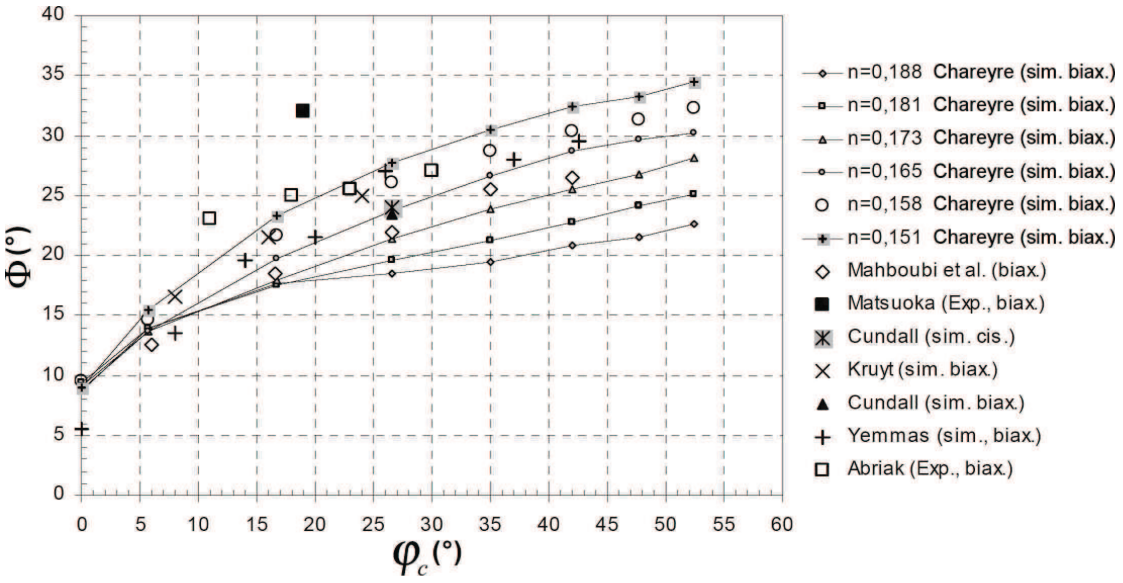

FIGURE 2.6: *Macroscopic friction angle in terms of microscopic friction angle, results from Mahboubi et al. [1996] and Chareyre [2003] , assembled by Sibille [2006a], with n is the porosity of the specimen*

An effective and simple solution to attain a realistic macroscopic friction angle is to block the rotation of the circular of spherical grains (Calvetti et al. [2003]). However, this method resolves only the issue on the macroscopic scale (the granular assembly), it does not describe precisely the real physical kinematics at the grains scale. Another authors (Iwashita and Oda [2000]), in a study of micro-mechanisms in the shear band, propose that we allow the transmission of moment between two grains in contact until a certain threshold. Otherwise, in order to better describe the behaviour of numerical granular models, some authors apply a variety of particles form; for example, Chareyre [2003] sticks particles into groups of two to create 2-particle clumps, Bonilla [2004] uses ellipsoid grains and Alonso-Marroquın [2004] uses polygonal form (Figure 2.7).

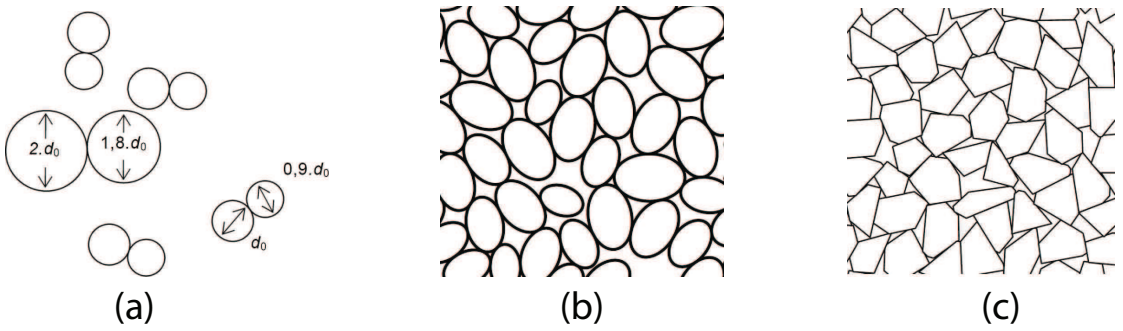

FIGURE 2.7: *Examples of the refinement of geometrical model of grains: (a) 2-particles clumps (Chareyre [2003]), (b) ellipsoid (Bonilla [2004]), (c) polygonal (Alonso-Marroquın [2004])*

The simulations in this thesis are carried out by the YADE software (Šmilauer et al. [2010]), where the particles are basically spheres for the 3D case; for the 2D case, certain degrees of freedom are blocked to have a 2D configuration (see Section 4.1.1). Generally, disks and spheres are currently the most common types of particles considered in 2D and 3D DEM simulations respectively. These particles are widely used as it is very simple to identify whether they are contacting; the geometry of the contact point, including the contact overlap or separation, can be accurately calculated. There are obviously more contacts than particles in a DEM simulation, since one particle can have contacts with several other particles, and contact resolution is usually the most computationally expensive part of the DEM algorithm. The more efficient this stage in the calculation is, the larger the number of particles can be included into the computation.

The numerical techniques used in DEM can be divided into two categories as *soft sphere* (molecular dynamics) and *hard sphere* (event driven) approaches. The *soft sphere* model (Figure 2.8(a)), in which the particle is considered "soft", allows the penetration between particles at the contact point. This method is logical, since in reality, we consider the deformation of particles at the contact point; also this method makes it easier to evaluate the contact force. In the case of *hard sphere* (Figures 2.8(b)), there is no deformation or penetration considered.

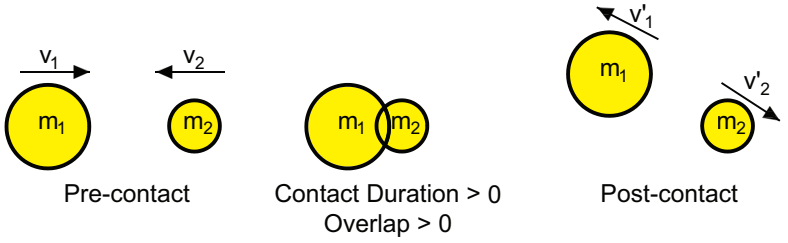

(a) "Soft sphere" model

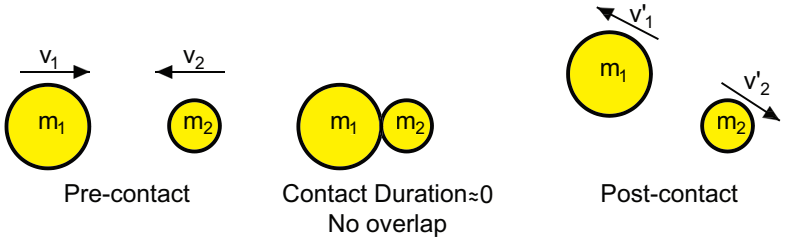

(b) "Hard sphere" model

FIGURE 2.8: *"Hard sphere" and "Soft sphere" contact models in DEM*

The principle behind the *soft sphere* method is to solve the equations governing the linear and angular dynamic equilibrium of contacting particles for every time step. In fact the word *soft* may cause some misunderstanding; in the simulation, soft particles are actually rigid, however they are allowed to have overlap at the contact points. Consequently, physical actions is realized only when spheres penetrate each other.

There are also some researchers developed a method call *contact dynamics* (Lanier and Jean [2000]). This method is also defined as 'non-smooth contact dynamics'. The idea of this method is that the contact forces are determined so that there is no deformation of particles (similar to *hard spheres* but allows finite contact durations).

In the YADE code, the *soft sphere* model is adopted. When disk or sphere particles are used, the contact overlap between to particles, p and q (Figure 2.9), is simply calculated as:

$$\begin{aligned} \delta_c &= R_p + R_q - \sqrt{(x_p - x_q)^2 + (y_p - y_q)^2} \quad (2D) \\ \delta_c &= R_p + R_q - \sqrt{(x_p - x_q)^2 + (y_p - y_q)^2 + (z_p - z_q)^2} \quad (3D) \end{aligned} \tag{2.12}$$

where R_p and R_q are the particle radii and the centroidial coordinates are given by (x_p, y_p, z_p) and (x_q, y_q, z_q) respectively.

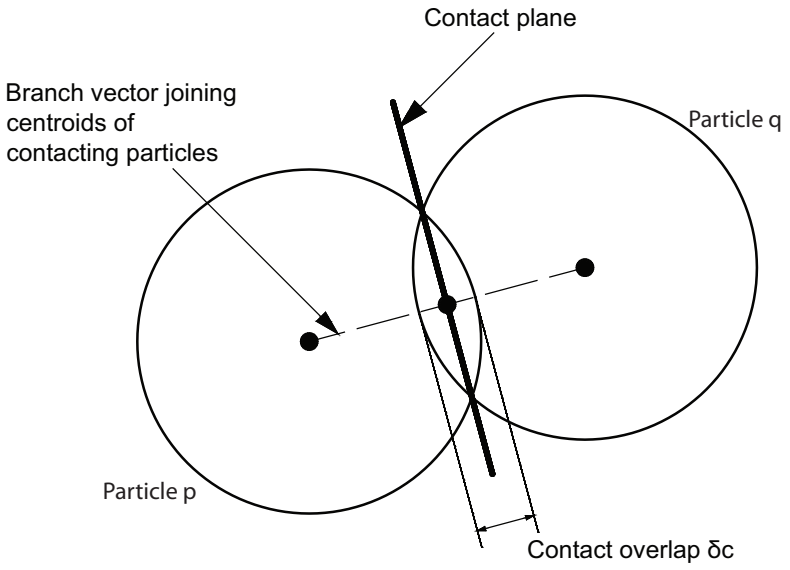

FIGURE 2.9: *Overlap between two particles in contact*

If the calculated overlap δ_c is positive then this contact is transmitting a compressive force, otherwise the contact is considered inactive. This calculation is also used in the contact detection phase of the simulation to assess whether the particles can potentially contact.

2.3.2 Boundary Conditions

In discrete element modeling, choosing the boundary conditions plays an important role. An essential point in setting up a DEM simulation is to decide which spatial domain will be considered. Then the boundaries of this domain must be numerically described in the DEM simulation. In continuum numerical modeling, the boundary conditions can be displacement conditions (the movement is restricted) or traction boundary conditions (the stress is specified). Similarly, in DEM simulation, the displacement boundary conditions can be defined by specifying the coordinates of elements or by fixing their movement; and the traction boundary conditions can be achieved by applying force to selected elements, the value of the applied force can be calculate directly from the sum of particle-boundary contact forces and the area of the boundary itself which is in agreement of a desired value of external stress. This external force is then added to the contact forces acting on the particles, after that the resultant force is used to calculate the particle accelerations and incremental displacements.

Several types of boundary conditions can be found in DEM simulation. The most classical one is the *rigid wall*, where the boundary is essentially a finite frictionless plane; this implementation is simple to detect the particle-wall contact and also makes the stress estimation easier as the stress acting on the boundary is the quotient of the sum of contact forces from the particle-wall interactions and the area of the wall. Another type of boundary condition is the *periodic boundaries*. Some authors are using this configuration in their study, such as Thornton [2000] and Ng [2004]. Periodic space is created by repetition of parallelepiped-shaped cell, which allows particles to "go through" the cell edge and re-appear on the opposite edge; therefore using periodic boundaries allows modeling of very large assemblies while considering only a sub-domain of granular specimen. The last type is *membrane boundaries*, where the boundaries are built from particles to make a flexible membrane.

In this manuscript, rigid walls are used as boundary conditions, which are typical and widely used in DEM simulation. Rigid walls are frictionless, have no mass (therefore they have no inertia), the contact force between particle and the wall is used only for updating the particle coordinates. As the forces acting on the walls do not influence the motion of the walls, the control of the walls is explicitly executed by applying a certain velocity onto them.

As the walls containing the specimen are frictionless, the principal directions of stresses and strains coincide with the coordinate axes $\boldsymbol{x}_1$, $\boldsymbol{x}_2$ and $\boldsymbol{x}_3$ (3D case). Along with prescribed boundary conditions, the stress and stress states in the specimen are considered homogeneous. The principal strains are then calculated directly from the walls displacement, while the correspondent principal stresses are obtained from contact forces at the boundary, similar to laboratory tests.

The walls only transmit normal contact forces from particles having contacts with them (because they are frictionless). When a particle penetrates a wall with the penetration depth δu_n, a proportional force is applied on this particle. This contact force $\boldsymbol{F}_c$ with the boundary is elastic and it is oriented in the normal direction to the wall:

$$\boldsymbol{F}_c = \boldsymbol{F}_n = k_n \delta u_n \boldsymbol{n} \tag{2.13}$$

In the case of spherical particle in contact with the boundary, the position vector $\boldsymbol{x}_{F_c}$ of the point applying the interaction force $\boldsymbol{F}_c$ is given by:

$$\boldsymbol{x}_{F_c} = \boldsymbol{x} - (R - \frac{\delta u_n}{2})\boldsymbol{n} \tag{2.14}$$

where $\boldsymbol{x}$ is the position vector of the particle and R is its radius.

In the numerical simulation, boundaries have no-mass, therefore they do not return any result from numerical integration scheme of Newton movement equations, and the walls do not interact with each other.

2.3.3 Specimen preparation

The algorithm used in this manuscript is adapted from the works of Sibille [2006b] and Hadda et al. [2013]. The *particle generation method* is a geometric algorithm and allows creating the assembly without the use of the dynamic calculation. This method is fast and the created particles do not have interaction with each other within the space defined by the boundaries during the generation process. However, this method makes it difficult to approach a desired grains size distribution.

In fact, particle's radii are manipulated by an algorithm: for each sphere, its radius is randomly chosen within a predefined range. Then this particle is located randomly inside the boundaries. By varying the parameters of the material (internal friction degree, range of random size generation...) and calibrate with other numerical model and experimental works, adequate models are chosen (Section 2.4).

When the mode of generation is chosen, the mode of compressing is defined: for each time step, radii of all particles are multiplied by a coefficient greater than 1, until the confining stress is reached ($\sigma_1 = \sigma_2 = \sigma_3 = 100kPa$ for the 3D case, $\sigma_1 = \sigma_2 = 100kPa$ for the 2D case). This method changed the size of particles, however the form of the grading curve is unchanged, it is just shifted along the axis of the size of the size of particles (Figure 2.12).

The procedure of the preparation consists of the following steps:

- The particle cloud is randomly generated inside the six walls (3D case) or four walls (2D case) with the same unique value for the radii of the particles. For the 3D case, the number of particles is 10000 particles (spheres), for the 2D case, the number of particles is 20000 particles (disks).
- Execution of the geometrical algorithm by randomly varying the radii of the particles. This step allows the specimen to have a particle assembly with random particle sizes.
- Isotropic compression step: gradually growing of the particles size with the same factor for every grains. At the same time, the stress calculated from the boundaries is computed and verified with the chosen confining stress. This step stops when the desired value of stress on the boundaries is reached (equal to the chosen confining stress) (Figure 2.10).

- Return to the idle state for the granular assembly in order to obtain a quasi-static regime by verifying an adequately small value of the kinetic energy of the system ($E_c \leq 10^{-7} J$), in comparison with the work created by the external load applying on the boundaries.

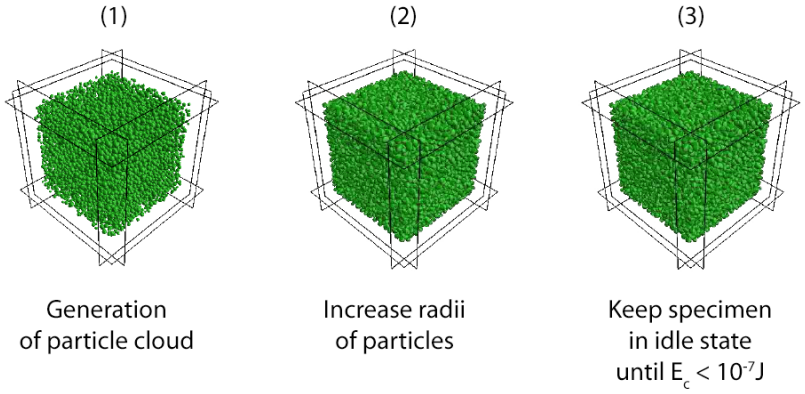

FIGURE 2.10: *Preparation of numerical 3D specimen*

It is worth noting that the porosity of the assembly depends on the friction angle's value φ_c (Hadda et al. [2013], Sibille [2006b]): the smaller φ_c is, the more compactness can be obtained. $\varphi_c = 5°$ is used to generate the dense specimen, and $\varphi_c = 25°$ is used for the loose specimen. The small value of φ_c allows the grains to slide more easily between each other, thus it is easier for them to fill the empty space in the sample.

2.3.4 Properties of the 3D numerical specimen

The 3D numerical specimen consists in a package of 10000 spheres in six frictionless walls. The visualization of the specimen is demonstrated in Figure 2.11.

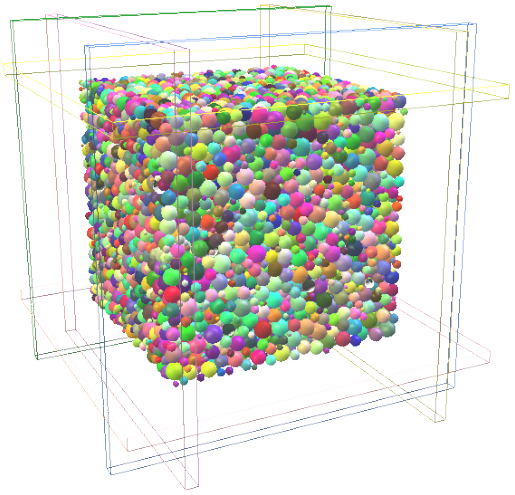

FIGURE 2.11: *3D numerical specimen in YADE*

The parameters of the specimens can be found in Table 2.1.

Terms	Number	Unit
Initial box's size	$0.198 \times 0.198 \times 0.198$	m × m × m
Number of particles	10000	-
Diameters	$0.002 \sim 0.0075$	m
k_n/D_s	356	MPa
k_t/k_n	0.42	-
Friction angle φ_c	35	deg
Void ratio e	0.61 (dense), 0.72 (loose)	-
Coordination number Z	4.3 (dense), 2.75 (loose)	-

TABLE 2.1: *Numerical parameters*

2.3.4.1 Grains size distribution

The variation of the particle diameters is obtained from the method of generation presented in Section 2.3.3. The diameter of the particles varies from 4 to 15 mm. The grading curve is shown in Figure 2.12:

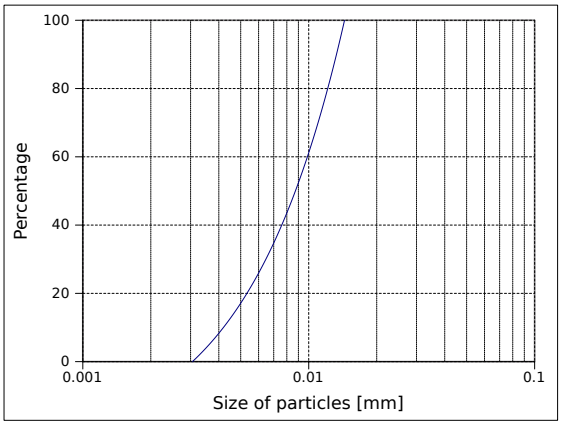

FIGURE 2.12: *The grading curve of the generated sample*

2.3.4.2 Contact orientations distribution

The numerical specimen generation procedure must satisfy the structural isotropy condition. The distribution of the contact orientations at the isotropic state, after the first compression, is shown in Figure 2.13(a) for the dense specimen and in Figure 2.13(b) for the loose specimen. In our case, the contacts near the boundaries are not taken into account in order to avoid the majority of normal direction to the walls. In this study, a distance $l = 1.5 \langle D_s \rangle$ from the boundaries is used. The result shows a satisfying isotropy of the distribution of the contact directions.

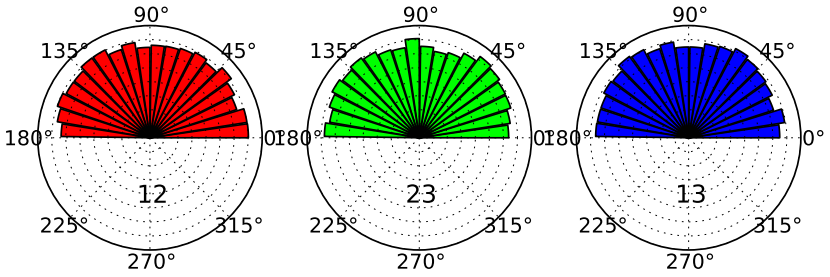

(a) Dense specimen

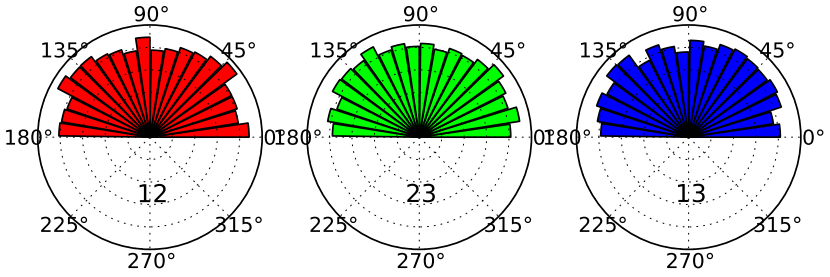

(b) Loose specimen

FIGURE 2.13: *Isotropy of the distribution of contact orientations of the specimens: (a) dense, (b) loose in three planes "12", "23" and "13" (See Figure 2.5 for the definition of the axis 1, 2 and 3)*

2.3.5 Void ratio e and coordination number Z

The void ratio quantifies the granular packing density without explicit consideration of the particulate structure; only the total mass of particles, the solid particle density and the global volume of the specimen are taken into account. The void ratio e of the 3D dense specimen is $e = 0.61$ and of the loose specimen is $e = 0.72$. The preparation of the numerical simulation produces a common range of void ratios and those two values are chosen for the rest of the study.

The coordination number Z, notion used by Thornton [2000], is defined as the average number of contacts on a single particle in the granular packing. It can be used to validate the generated specimen as a random close packing. In this thesis, number Z is calculated only on the contacts between particles and not on the contacts between particles and walls. The coordination number is simply calculated as:

$$Z = 2\frac{N_c}{N_p} \tag{2.15}$$

where N_c is the total number of contacts and N_p is the number of particles. The number of contacts is multiplied by 2 because one contact is shared by 2 particles. The number Z of the two specimens is shown in Table 2.1.

2.3.6 Simulation of the classical triaxial test

As mentioned in previous section, dense and loose specimens are prepared by an isotropic compression with a constant value of the stress applying on the walls. $\sigma_i = 100kPa\,(i = 1, 3)$. After that, the triaxial test is applied:

- The drained triaxial test: the lateral stresses are kept constant and an axial strain rate $\dot{\varepsilon}_1 = 0.01s^{-1}$ is applied on the top and bottom walls, moving toward the center of the specimen.
- The undrained triaxial test: a strain rate $\dot{\varepsilon}_1$ is applied on the top and bottom walls, while the lateral deformations are kept under the condition $\dot{\varepsilon_1} + \dot{\varepsilon_2} + \dot{\varepsilon_3} = 0$ (isochoric condition).

The results of the tests are shown in Figure 2.14: a drained triaxial test is carried out for the dense and loose specimens. The diagram demonstrates the evolution of the deviatoric stress $q = \sigma_1 - \sigma_3$, as well as the volumetric strain $\varepsilon_v = \varepsilon_1 + \varepsilon_2 + \varepsilon_3$, in terms of the axial strain ε_1. The simulation is stopped when the axial strain reaches 30%.

For the loose specimen, also an undrained triaxial test is simulated, the diagram demonstrates the evolution of the deviatoric stress versus the axial strain, also the relation between the deviatoric stress q and the mean stress $p = \frac{1}{3}(\sigma_1 + \sigma_2 + \sigma_3)$.

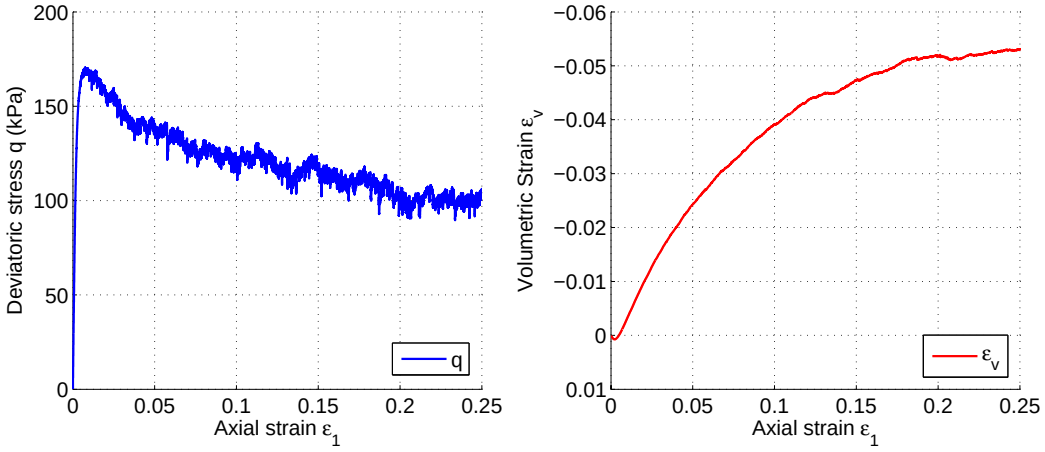

(a) Dense specimen (drained test)

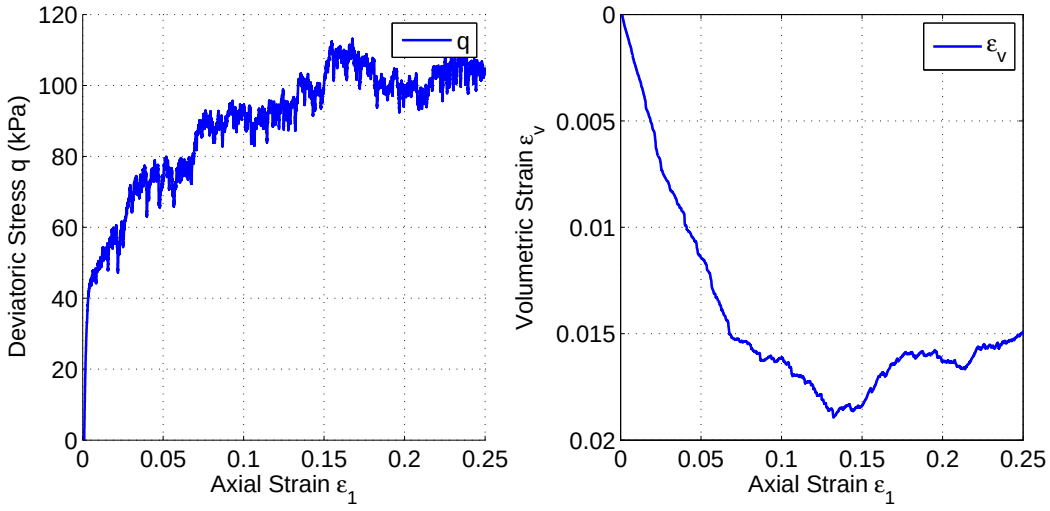

(b) Loose specimen (drained test)

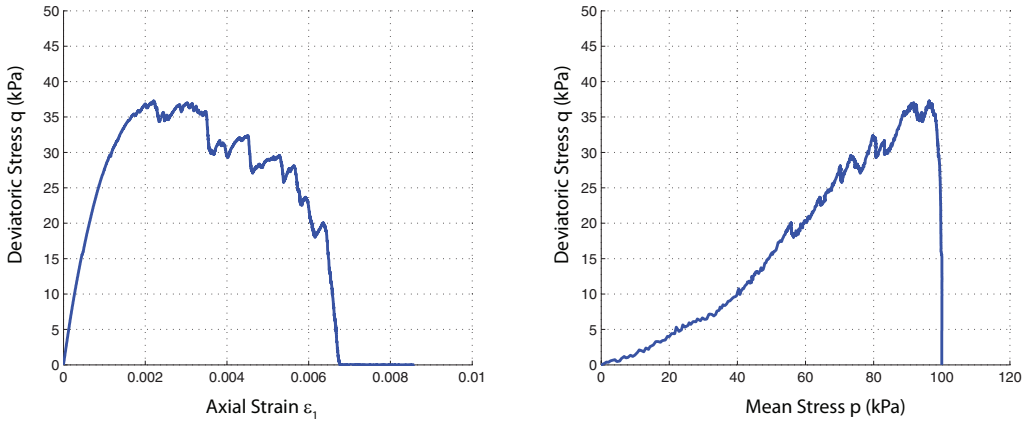

(c) Loose specimen (undrained test)

FIGURE 2.14: *Essential results of the numerical triaxial test*

2.4 Calibration of the numerical specimen

The numerical YADE model is calibrated based on the experimental work of Royis and Doanh [1998] and compared with the simulation of Calvetti et al. [2003]. The procedure of the calibration is summarized below:

- Because of the limitation of the numerical tool, the same grains size distribution as Hostun sand in the experimental study cannot be reproduced. The grain sizes are randomly generated and the void ratio $e = 0.65$ is selected.
- Then, the parameters k_t, k_n, φ_c are modified to match the numerical results as close as possible to the experimental data.

The parameters of the discrete model are shown in Table 2.2, and these parameters are compared with those used by Calvetti et al. [2003]. Only the loading paths between two simulations are identical. Figure 2.15 shows the comparison of the deviatoric stress q and the volumetric strain ε_v over the drained triaxial test between the experimental results Royis and Doanh [1998] and the two numerical models. Since the normal stiffness coefficient used in this manuscript is greater than the one used to calibrate, a fluctuation after the peak of the deviatoric curve is observed. It is worth to note that the numerical simulation carried out by Calvetti et al. [2003] is calibrated with the experimental results of Royis and Doanh [1998]. We observes that from the same geometry of a numerical specimen, we can vary the mechanic parameters in different ways to obtain the same system's response at the macroscopic scale.

	Number of particles	D_s (mm)	e	k_n/D_s (MPa)	k_t/k_n	φ_c $(^o)$
YADE Specimen	10000	2.0 to 7.5	0.65	356	0.42	20
Calvetti et al. [2003]	3500	0.15 to 0.45	0.72	222 to 667	0.25	19.3

TABLE 2.2: *Comparison of the parameters of the numerical models*

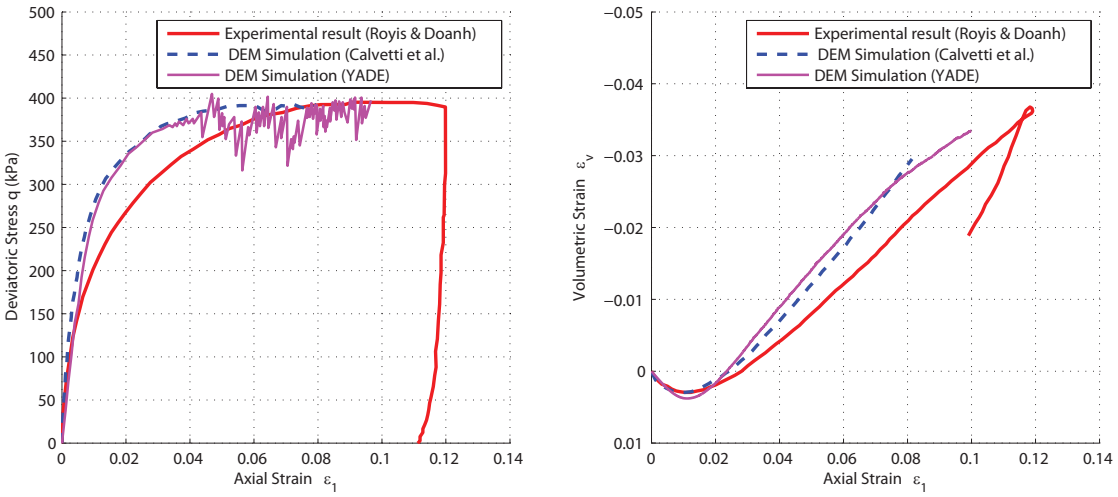

FIGURE 2.15: *Experimental curves Royis and Doanh [1998] and numerical results from Calvetti et al. [2003] and the YADE Code*

2.5 Conclusion

This chapter revisits the concept of DEM and explains how DEM works. It discusses through all necessary details for a DEM simulation: particles, boundary condition, contact law etc. and then points out the importance of DEM to geomechanics.

Then, this chapter presents the properties of the numerical specimens used in the manuscript by introducing all parameters used in the YADE DEM software. Two main 3D specimens are introduced: a dense package and a loose package. The numerical results show the basic mechanical response of a granular packing through the classical triaxial test: the drained test applied on both dense and loose specimens, and the undrained test applied on the loose specimen. These models are calibrated with numerical results and from an experimental database.

After this chapter, the numerical tools and specimens are prepared; then in following chapters, we address the problematics in the object of this thesis.

Chapter 3

Kinetic energy and diffuse failure mode in granular materials

3.1 Diffuse failure mode in granular materials

The notion of failure can be encountered in many fields, irrespective of the scale considered. This notion is essential in material's sciences where the failure can be investigated on the specimen scale. It is also meaningful in civil engineering to prevent or to predict the occurrence of failure on large scale. If the definition of failure seems to be meaningful in some cases, and at least from a phenomenological point of view, this is not always true, particularly when considering heterogeneous materials. For instance, for geomaterials made up of a grain assembly, the notion of failure remains disputable. When regarding a granular assembly on a microscopic scale, failure might be related to the contact opening between initially contacting grains. However, the kinematic investigation of granular materials, along any given loading path, reveals that an important fraction of the contacts open, without any visible failure pattern that can be observed on the macroscopic scale even though the disappearance of contact is not necessarily correlated with the local failure. Thus, the common "popular" definition of failure as the breakage of a given material body in two pieces cannot be applied to complex, divided materials made up of an assembly of elementary particles.

Generally, an effective failure in a material gives rise, according to the loading conditions, or to some disturbances, defects, etc., to outbursts in kinetic energy.

There is a transition (a bifurcation) from a quasi-static regime (the system admits a unique incremental response over a given incremental loading) toward a dynamical regime (inertial effects govern the response of the system). Effective failure manifests itself by suddenly exponentially growing strains. Moreover, these exponentially growing strains are associated with bursts of kinetic energy, as also observed experimentally and numerically.

From a theoretical point of view, by taking into account the energy conservation law in continuum mechanics expressed with a Lagrangian formalism and differentiated with respect to time (Nicot and Darve [2007], Nicot et al. [2007, 2012b]), the evolution of the kinetic energy can be expressed as a function of two basic integrals, namely the so-called second-order works: the external second-order work related to the external forces applied, and the internal second-order work related to the continuous constitutive behaviour of the body.

This equation is central since it highlights the role played by the second-order works in the onset of failure. Moreover, it proves that the failure is related to a conflict between the external load that one can apply onto the boundary of the system, and the internal stress taking place within the system, and directly related to the constitutive properties of the material. Even though this chapter does not attempt to be a complete review on the concept of second-order work, and on the related criterion, some general results are recalled herein. Initially introduced by Hill [1958] as an instability criterion, the second-order work criterion means that the material can continue to deform in one stress-strain direction without any external energy input (Valanis [1989]; Bigoni [2000], Bigoni and Hueckel [1991], Petryk [1993]). It was also proved that the second-order work criterion corresponds to the vanishing of the determinant of the symmetric part of the elasto-plastic matrix (Darve et al. [2004], Nicot et al. [2009], Prunier et al. [2009b]). This feature is very important, at least for two separate reasons:

- Firstly, let the Bromwich theorem Iordache and Willam [1998] be recalled. This theorem states that the smallest eigenvalue of the symmetric part $\mathbf{M}_s$ of any square matrix $\mathbf{M}$ is lower than any real part of the eigenvalues of $\mathbf{M}$ (the inequality is strict when $\mathbf{M}$ is nonsymmetric). Thus, the determinant of $\mathbf{M}_s$ always vanishes before that of $\mathbf{M}$. For many materials, as geomaterials, the elasto-plastic matrix is nonsymmetric. Thus, the determinant of

the symmetric part of the elasto-plastic matrix vanishes before the determinant of the elasto-plastic matrix itself, i.e. before the plastic condition is met. This result is fundamental because it indicates that a failure can occur even though the plastic condition is not met (as soon as the elasto-plastic matrix is nonsymmetric). In other words, the mechanical states at which the determinant of the symmetric part of the elasto-plastic matrix becomes nil constitute the lower boundary of the bifurcation domain (Neilsen and Schreyer [1993]; Darve et al. [2004]; Sibille et al. [2007]; Sibille et al. [2009]; Nicot and Darve [2007]; Nicot et al. [2009]);Prunier et al. [2009a], while its upper boundary is given by the plastic limit condition.

- Secondly, the second-order work criterion contains the particular cases of the strain localization criterion (vanishing value of the determinant of the acoustic matrix; Rudnicki and Rice [1975]). It can be proved that the second-order work criterion is met within the localization band. When the localization criterion is not met, the failure is diffuse, with a chaotic kinematical pattern.

The objective of this chapter is to check carefully the equation relating the second-order time derivatives of the kinetic energy of the system to the external and internal second-order works. For this purpose, numerical simulations based on a discrete element method Cundall and Strack [1979] will be employed to model the response of a granular assembly along different loading paths. Firstly, a dense specimen will be considered, subjected to a conventional drained triaxial loading path. It will be shown that an abrupt collapse can be observed at the deviatoric stress peak, if some (even small) additional, external loads are prescribed. Then, an undrained triaxial loading path will be simulated by considering a loose specimen. Here again, at the deviatoric stress peak, the collapse of the specimen is observed when an additional load is imposed. The discrete element method enables simulating the collapse of the specimen in a straightforward manner, since the motion of each particle can be followed over time. In this context, two different numerical methods will be compared to approach the second-time derivatives of the kinetic energy, together with both the external and internal second-order works, once failure has occurred.

3.2 The continuum approach

3.2.1 Kinetic energy and second-order work

Effective failure of a granular system as a transition from a quasi-static regime to a dynamic regime was proved to be associated with an outburst in kinetic energy (Nicot et al. [2012b]). The effective failure of soil specimen can be regarded as the collapse of the system when the specimen is no longer able to sustain the external load. This leads to large deformation, where strains increase greatly in a short period of time. This failure mode is also called diffuse failure mode (Darve et al. [2004]). When the system turns from quasi-static to dynamic regime, it is reasonable to analyse the variation of kinetic energy. Thereafter, we particularize the analysis to a cubic specimen ($L_1 \times L_2 \times L_3$) as defined in figure 3.1.

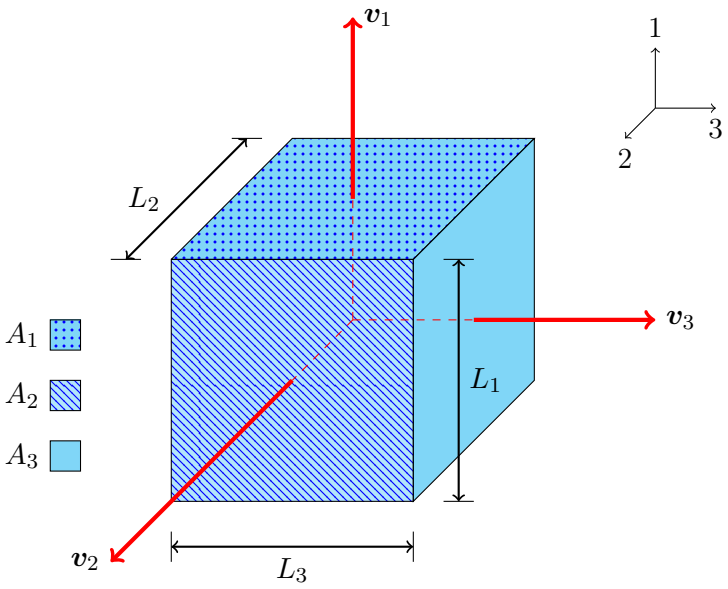

FIGURE 3.1: *Cubic specimen - geometrical settings*

The index direction '1' is the axial direction while '2' and '3' are the lateral directions. Based on this configuration, the external stress s is defined by forces acting on along boundaries, this average stress is calculated by summing the contact forces f along the boundary, and dividing by the surface area of the rigid boundary for the model 3D. When a stress is applied on a certain side 'i', it means equivalently that an external force f_i is introduced on the sides and consequently, the external stress is $s_i = f_i/A_i$ where A_i is the area of the surface perpendicular

to the direction 'i' as mentioned in Figure 3.1. The displacement of each side 'i', along the direction $\boldsymbol{v}_i$ is denoted $U_i = \boldsymbol{u}.\boldsymbol{v}_i$. In contrast, the internal stress $\boldsymbol{\sigma}$ (or $\boldsymbol{\Pi}$) takes place within the specimen, resulting from the constitutive behaviour of the considered material.

In the initial configuration C_0, at time t_0, the specimen has a volume $V_0 = L_1^0 L_2^0 L_3^0$, and a volumic mass ρ_0 enclosed by the boundary $\Gamma_0 = \partial V_0$. After a certain loading history, the body is in a strained configuration C and occupies a volume $V = L_1 L_2 L_3$ of boundary (Γ), in equilibrium under a prescribed external loading. This loading is defined by specific static or kinematic parameters, referred to as the loading parameters. $F_{ij} = \frac{\partial x_i}{\partial X_j} = \delta_{ij} + \frac{\partial U_i}{\partial X_j}$ is the general term of the deformation gradient tensor $\boldsymbol{F}$. $\boldsymbol{\Pi}$ denotes the Piola-Kirchhoff stress tensor of the first type, $\boldsymbol{\Pi} = det\boldsymbol{F}\boldsymbol{\sigma}\boldsymbol{F}^{-T}$. $\boldsymbol{\Pi}$ is the transformed quantity of the Cauchy stress tensor $\boldsymbol{\sigma}$ through the bijection ϑ mapping the material point from the reference configuration to the current configuration ($\boldsymbol{x} = \vartheta(\boldsymbol{X})$). This bijective transformation is convenient so as to obtain all integrals given with respect to a fixed domain. In this context:

$$\langle \boldsymbol{F} \rangle = \begin{bmatrix} \langle F_{11} \rangle & 0 & 0 \\ 0 & \langle F_{22} \rangle & 0 \\ 0 & 0 & \langle F_{33} \rangle \end{bmatrix} \text{ and } \langle \boldsymbol{\Pi} \rangle = \begin{bmatrix} \langle \Pi_{11} \rangle & 0 & 0 \\ 0 & \langle \Pi_{22} \rangle & 0 \\ 0 & 0 & \langle \Pi_{33} \rangle \end{bmatrix}$$

Where $\langle M \rangle = 1/V_0 \int_{V_0} M dV$ denotes the mean value of the variable M over the whole volume V_0.

Adopting a Lagrangian formulation and in absence of body forces, the evolution of each material point of the system is given by the equation:

$$\rho_0 \ddot{U}_i - \frac{\partial \Pi_{ij}}{\partial X_j} = 0 \tag{3.1}$$

where $\boldsymbol{u}$ is the displacement field. The kinetic energy of the whole system reads:

$$E_c = \frac{1}{2} \int_{V_0} \rho_0 \dot{\boldsymbol{U}}^2 dV_0 \tag{3.2}$$

A double time differentiation of equation (3.2) yields:

$$\ddot{E}_c = \int_{V_0} \rho_0 \ddot{\boldsymbol{U}}^2 dV_0 + \int_{V_0} \rho_0 \dot{\boldsymbol{U}} \cdot \dddot{\boldsymbol{U}} dV_0 \tag{3.3}$$

Combining equation (3.3) with equation (3.1) gives:

$$\ddot{E}_c = \int_{V_0} \rho_0 \ddot{\boldsymbol{U}}^2 dV_0 + \int_{V_0} \dot{U}_i \frac{\partial \dot{\Pi}_{ij}}{\partial X_j} dV_0 \tag{3.4}$$

By virtue of the Green formula, equation (3.4) can be written as:

$$\ddot{E}_c = \int_{V_0} \rho_0 \ddot{\boldsymbol{U}}^2 dV_0 + \int_{\Gamma_0} \dot{U}_i \dot{\Pi}_{ij} N_j dS_0 - \int_{V_0} \dot{\Pi}_{ij} \frac{\partial \dot{U}_i}{\partial X_j} dV_0 \tag{3.5}$$

It results that the second-order time derivative of the kinetic energy is the sum of three terms:

- The first term $I_2 = \int_{V_0} \rho_0 \ddot{\boldsymbol{U}}^2 dV_0$ is an inertial term. As a quadratic average of the acceleration, this term is always positive.
- The second term $\int_{\Gamma_0} \dot{U}_i \dot{\Pi}_{ij} N_j dS_0 = \int_{\Gamma_0} \dot{U}_i \dot{s}_i dS_0$ is a boundary term involving the control parameters (the displacements $\boldsymbol{U}$, and the current external forces $\boldsymbol{f}$ with $d\boldsymbol{f} = \boldsymbol{s} dS_0$) acting on the boundary of the initial (reference) configuration of the system. It is thereafter called the external second-order work W_2^{ext} and can be expressed as:

$$W_2^{ext} = \sum_{i=1}^{3} \dot{s}_i \dot{U}_i A_i = \dot{s}_1 \dot{U}_1 A_1 + \dot{s}_2 \dot{U}_2 A_2 + \dot{s}_3 \dot{U}_3 A_3 \tag{3.6}$$

- The third term introduces explicitly the second-order work which expresses, following a semi-Lagrangian formalism Hill [1958], as $\int_{V_0} \dot{\Pi}_{ij} \frac{\partial \dot{U}_i}{\partial X_j} dV_0 = \int_{V_0} \dot{\Pi}_{ij} \dot{F}_{ij} dV_0$. This term is related to the constitutive behaviour of the material, and is therefore referred to as the internal second-order work W_2^{int}. It should be noted that at any material point of the system, both stress rate tensor $\dot{\boldsymbol{\Pi}}$ and velocity gradient tensor $\dot{\boldsymbol{F}}$ are related by the constitutive equation $\dot{\Pi}_{ij} = L_{ijkl} \dot{F}_{kl}$, where the four-order tensor $\overset{(4)}{\boldsymbol{L}}$ is the tangent constitutive tensor for rate-independent materials.

For the homogeneous case, it is possible to invoke the fundamental Hill identity, where $\left\langle \dot{\Pi}_{ij}\dot{F}_{ij} \right\rangle = \left\langle \dot{\Pi}_{ij} \right\rangle \left\langle \dot{F}_{ij} \right\rangle$. The internal second-order work reads:

$$W_2^{int} = \int_{V_0} \dot{\Pi}_{ij}\dot{F}_{ij} dV_0 = V_0 \left\langle \dot{\Pi}_{ij}\dot{F}_{ij} \right\rangle = V_0 \left\langle \dot{\Pi}_{ij} \right\rangle \left\langle \dot{F}_{ij} \right\rangle \tag{3.7}$$

For the sake of simplicity, terms F_i (resp. $\dot{F}_i$) and Π_i (resp. $\dot{\Pi}_i$) denotes $\langle F_{ii} \rangle$ (resp. $\left\langle \dot{F}_{ii} \right\rangle$) and $\langle \Pi_{ii} \rangle$ (resp. $\left\langle \dot{\Pi}_{ii} \right\rangle$). As $\dot{F}_i = \frac{\dot{U}_i}{L_i}$, notice that the initial volume of the specimen is given by $V_0 = L_1 A_1 = L_2 A_2 = L_3 A_3$, then $A_i = V_0 / L_i$. The internal second-order work can be expressed as:

$$W_2^{int} = \dot{\Pi}_1 \dot{U}_1 A_1 + \dot{\Pi}_2 \dot{U}_2 A_2 + \dot{\Pi}_3 \dot{U}_3 A_3 \tag{3.8}$$

It follows that equation (3.5) can be expressed as:

$$\ddot{E}_c = I_2 + W_2^{ext} - W_2^{int} \tag{3.9}$$

Based on equations (3.6) and (3.8), the equation (3.9) can be rewritten as:

$$\ddot{E}_c = I_2 + \sum_{i=1}^{3} (\dot{s}_i - \dot{\Pi}_i) \dot{U}_i A_i \tag{3.10}$$

It is important to distinguish the stress acting on the boundary of the specimen and the stress acting within the specimen. The constitutive response of the specimen is characterized by a relation between strain rate $\dot{F}_i$ and stress $\dot{\Pi}_i$. However the only information that can be obtained is via boundary record, involving s_i and U_i. During a quasi-static evolution of the specimen, the internal stress tensor within the specimen is balanced with the external stress vector, so that for each side 'i' $\Pi_i = s_i$. Thus, the constitutive response of the specimen can be investigated in that case from the measurable variables s_i and U_i (or $F_i = U_i / L_i + 1$). This is exactly what is done during laboratory tests. This is sound until the specimen fails: if inertial effects take place, the external stress is not balanced by the internal stress, and a heterogeneous strain field may develop within the specimen Nicot et al. [2012b].

The problem at hand now is specialized into a granular material comprised of N grains. Throughout the manuscript, 'p' will denote indiscriminately the grain (as

a body) or enumerate a particular grain within the assembly such that $1 \leq p \leq N$. Then, the equation (3.2) can be rewritten as:

$$E_c = \sum_{p \in V_0} \frac{1}{2} m^p (\boldsymbol{v}^p)^2 + \frac{1}{2} \boldsymbol{\omega}^p (I^p (\boldsymbol{\omega}^p)^T) \tag{3.11}$$

where m^p is the mass of particle 'p', $\boldsymbol{v}^p$ is the velocity of particle 'p', I^p is the moment of inertia and $\boldsymbol{\omega}^p$ is the angular velocity of 'p'.

Likewise, we have:

$$I_2 = \sum_{p \in V_0} m^p (\ddot{u}^p)^2 \tag{3.12}$$

The purpose of the following development is to compute the evolution of the kinetic energy over time, using two different ways: (1) by considering a direct computation from equation (3.9); (2) by a numerical integration procedure has to be set up in order to deduce the kinetic energy. In what follows, two numerical procedures are compared: first, a series expansion approach is considered; then, an integral approach is used.

3.2.2 Series expansion approach

Let us consider a small increment of time Δt between t and $t + \Delta t$. The Taylor expansion of $E_c(t)$ is:

$$E_c(t + \Delta t) = E_c(t) + \Delta t \dot{E}_c(t) + \frac{\Delta t^2}{2} \ddot{E}_c(t) + o(\Delta t^3) \quad \forall \Delta t \tag{3.13}$$

At time t, the system is supposed to be in equilibrium state, then $E_c(t) = 0$ and $\dot{E}_c(t) = 0$ (Nicot et al. [2012b]). When the time increment Δt is small enough, the equation (3.13) becomes:

$$\Delta t^2 \ddot{E}_c(t) \approx 2 E_c(t + \Delta t) \tag{3.14}$$

By combining equation (3.14) with (3.9) we obtain an expression of the kinetic energy as a function of the second-order works of the system:

$$E_c(t + \Delta t) \approx \frac{1}{2} (I_2 + W_2^{ext} - W_2^{int}) \Delta t^2 \tag{3.15}$$

Based on equation (3.15), in the numerical validation process, the external and internal second-order works will be captured and compared explicitly with the evolution of the kinetic energy for every time step. It should be noted that this approximation is limited to small time increments.

3.2.3 Integral approach

From equation (3.9), an alternative approach consists in integrating twice equation (3.9) with respect to time. By doing so and recalling that $E_c(t) = 0$ and $\dot{E}_c(t) = 0$, for each value Δt, an integral expression of $E_c(t + \Delta t)$ can be found:

$$E_c(t+\Delta t) = \int_t^{t+\Delta t} \left(\int_t^T (I_2 + W_2^{ext} - W_2^{int}) \delta\tau \right) \delta T \tag{3.16}$$

The purpose of the next section is to evaluate these two approaches from a numerical analysis based on discrete element simulations.

3.3 Numerical inspection

The numerical specimen considered in this chapter was introduced in chapter 2. It is a dense specimen of 10000 spherical particles placed inside 6 frictionless walls.

Since the response received from the DEM simulation is dynamic, the quasi-static response of the specimen is attained for a sufficiently low loading rate. As mentioned in Nicot et al. [2012b], this DEM tool can be used to investigate the increase in kinetic energy by comparing the balance between the loading defined at the boundary of the system and the bearing capacity of this system related to the constitutive behaviour at the material point scale.

In this study, even though large deformation is supposed to take place, it will be assumed (for the sake of simplicity) that the evolution of the system can be characterized by $\boldsymbol{\varepsilon}$ (small strain tensor) and $\boldsymbol{\sigma}$ (Cauchy stress tensor), using an updated Lagragian configuration. Thus, at each loading state, both Cauchy stress tensor ($\boldsymbol{\sigma}$) and Piola-Kirchhoff stress tensor ($\boldsymbol{\Pi}$) coincide. Likewise, $\dot{\boldsymbol{\varepsilon}}$ and $\dot{\boldsymbol{F}}$ coincide.

The flow chart of the simulation is described in figure 3.2

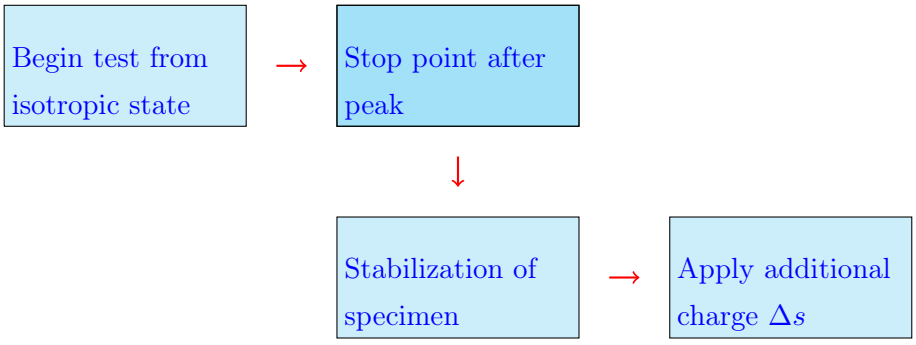

FIGURE 3.2: *Flow chart of the general simulation*

In the next section, two simulations are considered: first, a drained test applied to the dense package; then, an undrained test applied to the loose package. As previously mentioned in Chapter 2, the parameters of the two specimens are indicated in Table 3.1.

Terms	Values	Unit
Number of particles	10000	-
Diameters	$0.002 \sim 0.0075$	m
k_n/D_s	356	MPa
k_t/k_n	0.42	-
Friction angle φ_c	35	deg
Void ratio e	0.61 (dense), 0.72 (loose)	-

TABLE 3.1: *Numerical parameters*

3.3.1 Drained triaxial test

The specimen is first compressed with the external stress $s_1 = s_2 = s_3 = 100kPa$. Then from this isotropic state, the lateral stress is kept constant $s_2 = s_3 = 100kPa$ and a strain rate $\dot{\varepsilon}_1 = 0.01s^{-1}$ is applied. This value of strain rate is kept constant in order to maintain the quasi-static condition for the system. Under this mode of control, the internal stress balances with the external stress ($s_i = \sigma_i$). Until the desired state after the peak of the curve (q, ε_1) is reached (marked as point A in Figure 3.3, where $q = \sigma_1 - \sigma_3$ is the deviatoric stress), the control of the system is switched into a full stress control so that the specimen is stabilized by fixing the value of the external stress by $s_1 = \sigma_1^A = 266.5kPa$ and $s_2 = s_3 = 100kPa$.

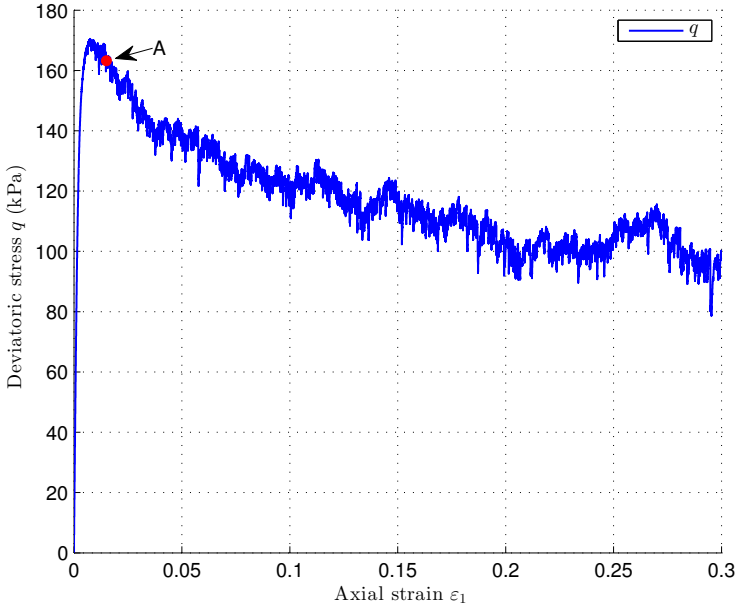

FIGURE 3.3: *Evolution of deviatoric stress q in terms of axial strain of the drained triaxial test*

The additional charge Δs is applied at point A once the specimen is stabilized. This application is executed by an imposed force $f = \Delta s \times A_{top}$ to obtain the stress value of $\Delta s = 5kPa$, as described in figure 3.4. Thus, the external loading conditions are:

- $s_1 + \Delta s = 266.5 + 5 = 271.5(kPa)$ applied to the upper plateau
- $s_2 = s_3 = 100(kPa)$ applied to the lateral walls

where A_{top} is the area of the top surface of the specimen at the time the additional force is applied on the system.

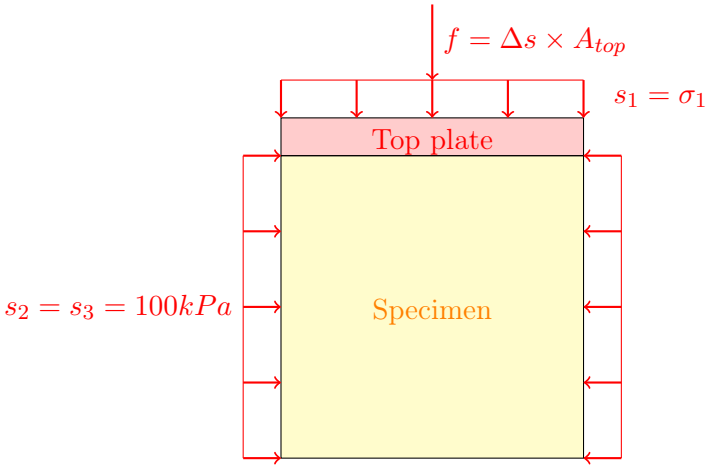

FIGURE 3.4: *The additional force applied on the top-plate after stabilization*

The additional force is not applied directly but gradually in 400 numerical time steps to avoid any too strong dynamic effect.

The evolution of the kinetic energy of the system after the application of the additional charge Δs is shown in figure 3.5: in short time period, an outburst of E_c is observed. By comparing E_c with the evolution of the axial strain ε_1, it is important to note that the investigation is only carried out until $\Delta t = 0.05s$ because after that time, the axial strain is close to 70%; as seen in figure 3.5, at this moment, the specimen has completely collapsed.

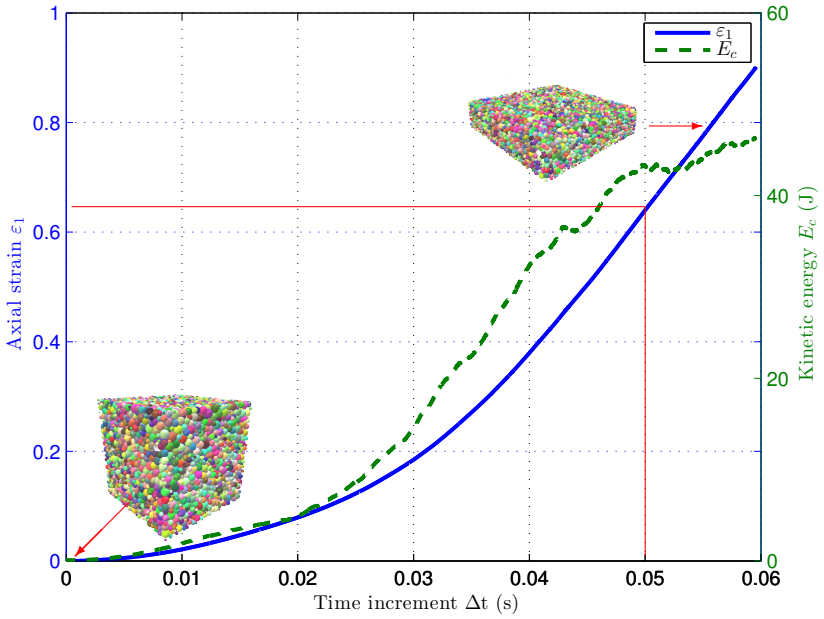

FIGURE 3.5: *Time evolution of axial strain and kinetic energy after the application of* Δs

From the very beginning of the application of the additional load, the internal stress σ_1 increases to balance the applied load s_1. This phenomenon can be explained by the fact that the system slightly gains this capacity after the stabilization process; but immediately after that, as seen in Figure 3.6, σ_1 decreases rapidly and then separates from the applied external stress s_1.

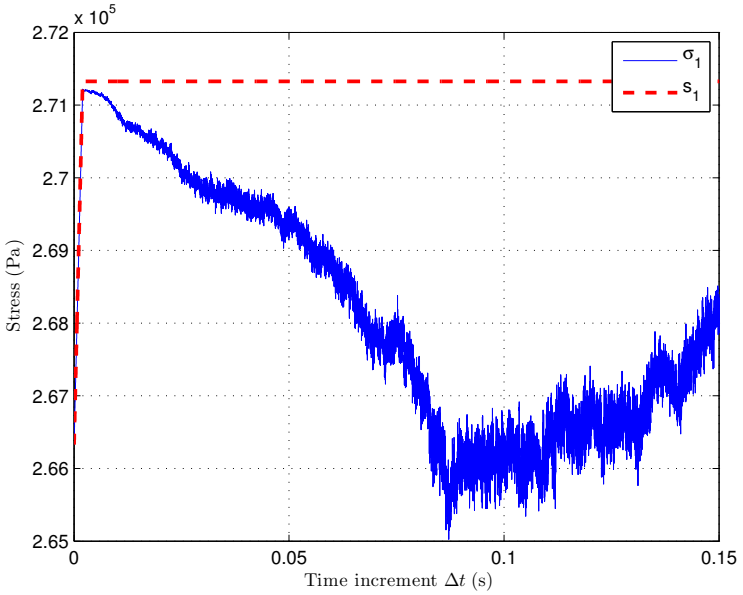

FIGURE 3.6: *Evolution of both internal stress σ_1 and applied stress s_1*

This phenomenon recalls equation (3.10). In this test, the lateral external stress is kept constant $s_2 = s_3 = 100kPa$, then $\dot{s}_2 = \dot{s}_3 = 0$. Therefore in this context, equation (3.10) can be rewritten as:

$$\ddot{E}_c = I_2 + A_1\dot{U}_1(\dot{s}_1 - \dot{\sigma}_1) \tag{3.17}$$

Therefore, the unbalance between external stress s_1 and internal stress σ_1 (with $\dot{\sigma}_1 < 0$ and $\dot{s}_1 = 0$) in this case leads to $\ddot{E}_c > 0$, which describes an outburst in kinetic energy.

The result of the two numerical approaches mentioned in sections 3.2.2 and 3.2.3 is shown in Figure 3.7 and a zoom to a smaller time step Δt is demonstrated in Figure 3.8 and Figure 3.9. For a small increment of Δt from $0s$ to $0.02s$, the series expansion shows a good adequacy with the kinetic energy within the specimen computed using equation (3.11); however, when Δt is larger ($\Delta t > 0.02s$), this agreement

between these two terms is no longer maintained, as expected when using the Taylor series expansion of E_c. On the other hand, the second approach involving a numerical integration of the term E_c and $\int_t^{t+\Delta t}\left(\int_t^T (I_2 + W_2^{ext} - W_2^{int})\delta\tau\right)\delta T$ leads to a better agreement for larger time steps, as demonstrated in Figure 3.9. In fact, unlike equation (3.15), equation (3.16) is not an approximation, and gives the exact expression of the kinetic energy with respect to both internal and external second-order works. However, for long time periods, a discrepancy develops caused by large strains taking place within the specimen and loss of homogeneity.

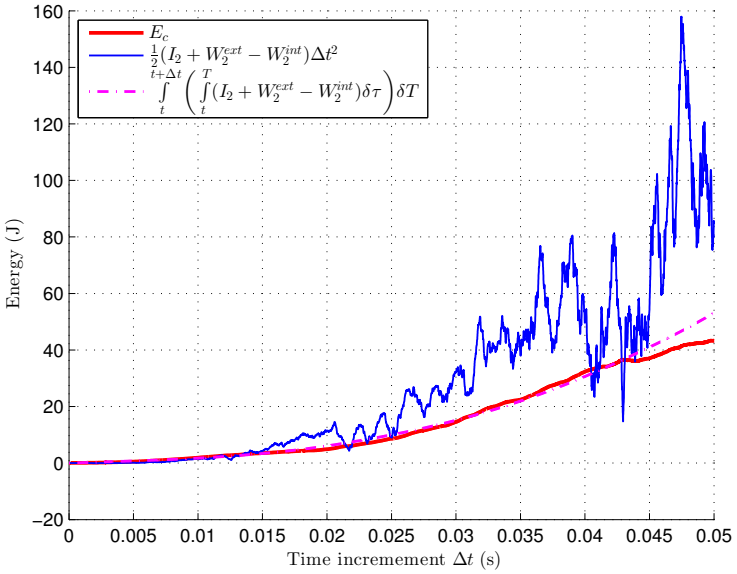

FIGURE 3.7: *Computation of the kinetic energy from the second-order work equation*

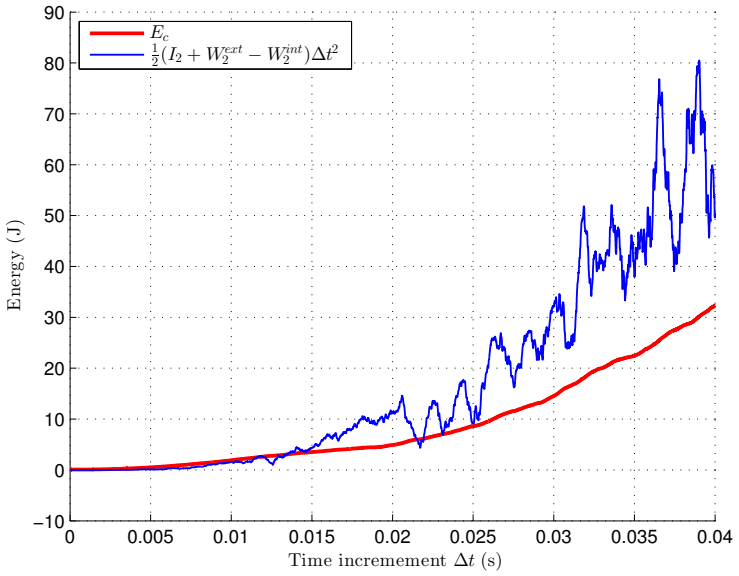

FIGURE 3.8: *Kinetic energy E_c - Series expansion approach*

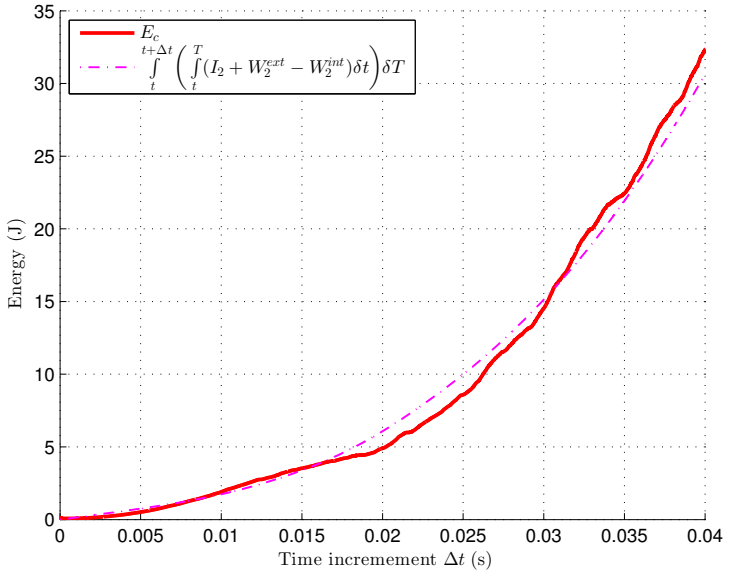

FIGURE 3.9: *Kinetic energy E_c - Integral approach*

After the time $\Delta t = 0.04s$, the axial strain ε_1 reaches over 40 % and the specimen collapses.

The results clearly show that, equation (3.15) is valid only for an infinitesimally small time step from the equilibrium state, whereas equation (3.16) is valid until the system has collapsed. These two approaches have been investigated for the

drained triaxial test on a dense specimen. In the next section, the undrained triaxial test on a loose specimen is considered.

3.3.2 Undrained triaxial test

The second specimen investigated is a loose specimen with the same parameters as those reported in Table 2.1. This specimen is subjected to an undrained (isochoric) triaxial test in asymmetric condition. The strain rate applied to the top plate is $\dot{\varepsilon}_1 = 0.01s^{-1}$. The isochoric condition reads: $\dot{\varepsilon}_1+\dot{\varepsilon}_2+\dot{\varepsilon}_3 = 0$. The condition on the lateral walls is therefore $\dot{\varepsilon}_2 = \dot{\varepsilon}_3 = -\frac{1}{2}\dot{\varepsilon}_1$. In order to stabilize the specimen until an equilibrium state is reached, at the desired point B described in Figure 3.10, the walls are fixed until the specimen fully attains a quasi-static regime before the application of the additional load Δs. At this point, the control on the boundaries is switched into stress control while maintaining the isochoric condition. Since this is a loose package, the choice of B must be close enough to the peak of the curve $q - p$ or otherwise it will be impossible to stabilize the specimen.

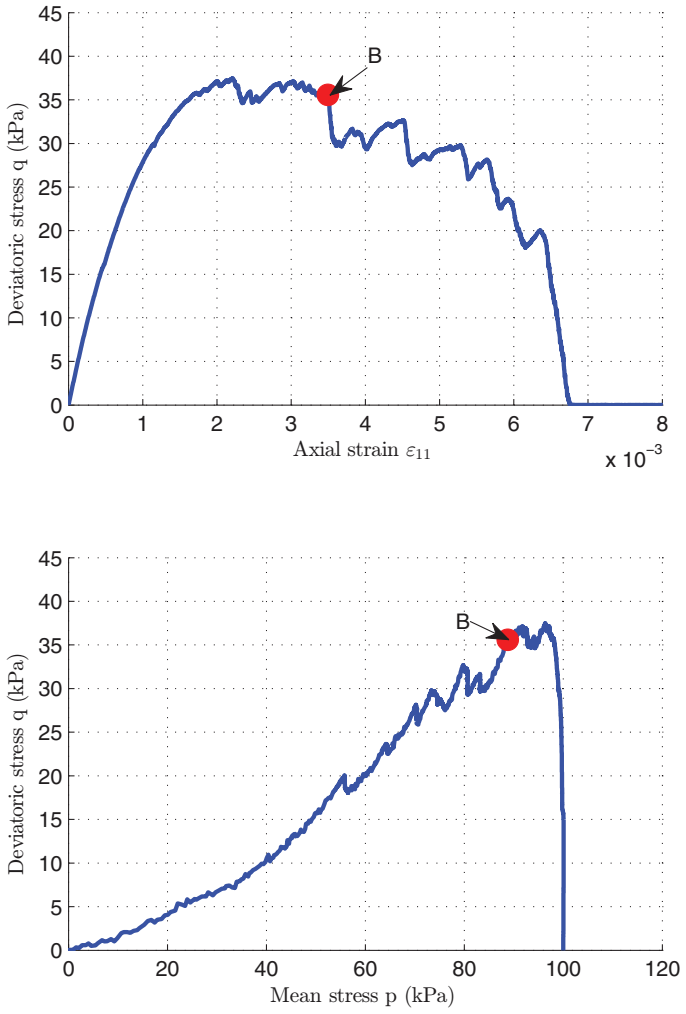

FIGURE 3.10: *Deviatoric stress in terms of axial strain ε_1 and mean stress p. The point B at which the additional load is applied is indicated.*

Similar to the dense specimen, the additional load Δs is applied gradually in 300 numerical time steps to the top plate while the isochoric condition is kept to maintain the isochoric behaviour. The investigation is carried out to $\Delta t = 0.05s$ corresponding to an axial strain ε_1 greater than 80%. At this time the specimen is completely collapsed, as seen in Figure 3.11.

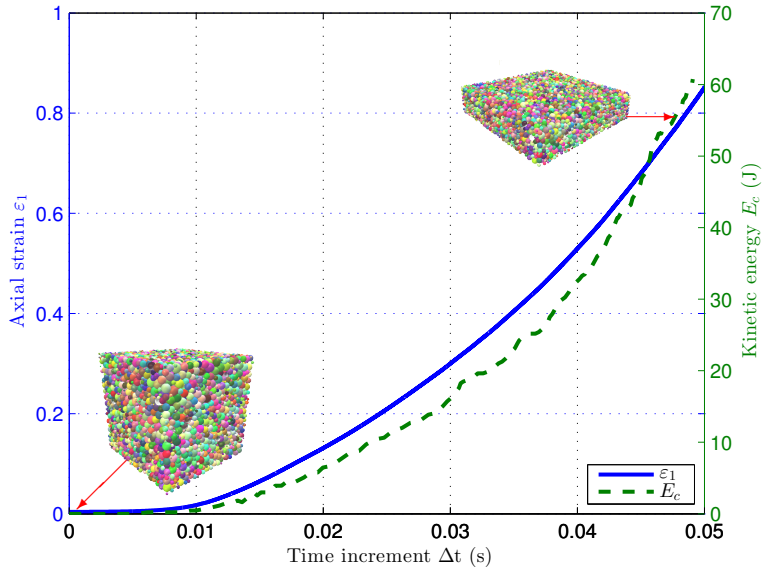

FIGURE 3.11: *Axial strain and kinetic energy after the application of* Δs

As a result of the additional load, the internal stress σ_1 at the beginning can balance the applied stress s_1 because the specimen gains strength after stabilization, but immediately after σ_1 and s_1 rapidly separate from each other (figure 3.12).

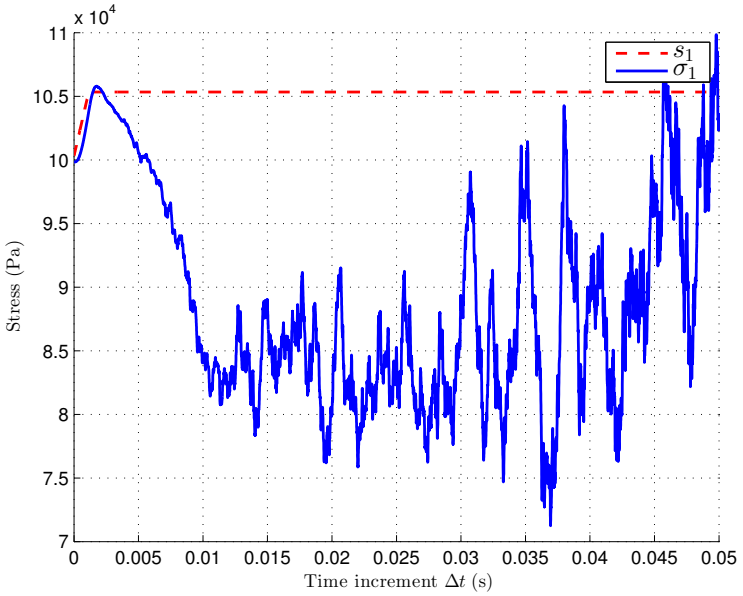

FIGURE 3.12: *Internal stress* σ_1 *and applied stress* s_1

As observed in the previous section, and according to equation (3.10), the difference between the internal and external stresses leads to an outburst in the kinetic energy E_c of the system.

The E_c and the series expansion is compared and good agreement between these terms is found for a small time increment value (Figure 3.13), from $\Delta t = 0s$ to $\Delta t = 0.015s$; after that the agreement is no longer valid.

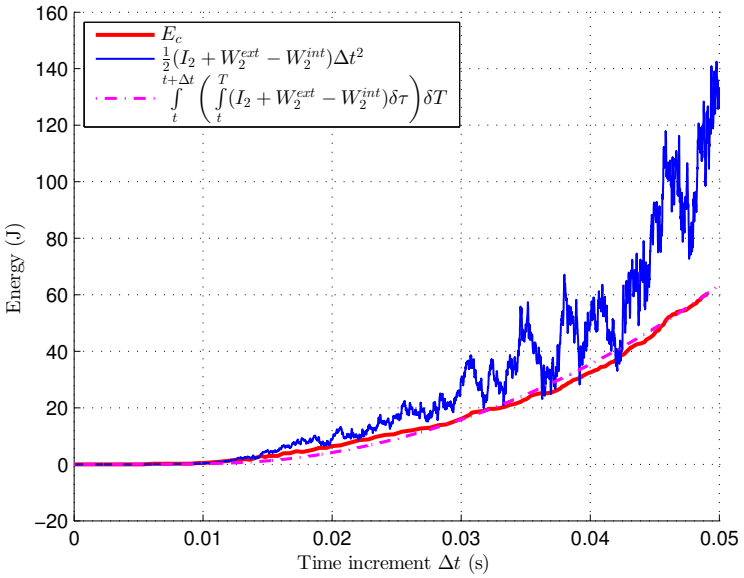

FIGURE 3.13: *Computation of the kinetic energy E_c from the second-order work equation*

The diagram in Figure 3.14 shows a clearer view of the comparison between the evolution of the kinetic energy E_c and the series expansion approach $0.5 \times (I_2 + W_2^{ext} - W_2^{int})\Delta t^2$. In this diagram, a closer zoom to the time step Δt highlights only the terms concerned, and shows that the agreement is valid for short time steps ($\Delta t \sim 0.015s$).

The result of the second approach is shown in Figure 3.15, with good agreement between the kinetic energy and the integral term $\int_t^{t+\Delta t}\left(\int_t^T (I_2 + W_2^{ext} - W_2^{int})\delta\tau\right)\delta T$ until the collapse of the specimen ($\Delta t \sim 0.04s$).

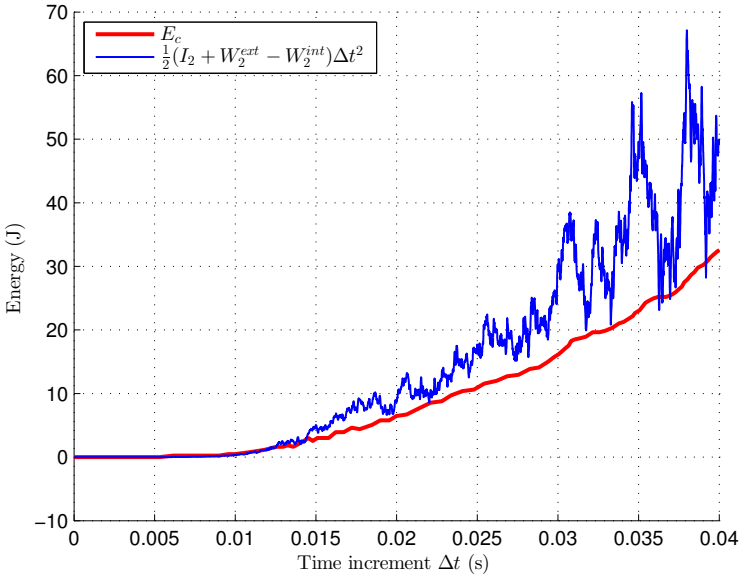

FIGURE 3.14: *Kinetic energy E_c - Series expansion approach (zoom to short time increments)*

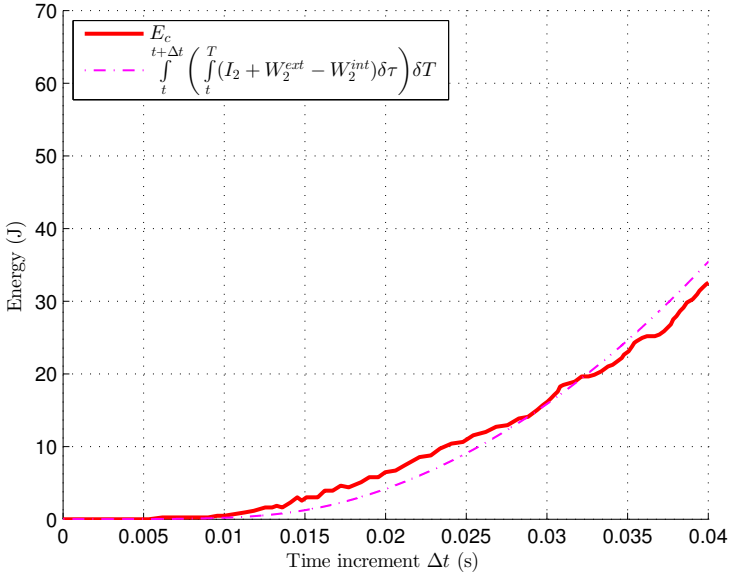

FIGURE 3.15: *Kinetic energy E_c - Integral approach (zoom to short time increments)*

For the loose package, an outburst in kinetic energy is also found when an additional load is applied to the specimen, where the system turns from quasi-static to a dynamic regime and leads to the diffuse failure mode.

3.4 Conclusion

We have investigated the mechanism of collapse from an equilibrium state of a granular, rate-independent material, where the failure is defined by an outburst in kinetic energy under incremental loading. This increase in kinetic energy is caused by the difference between the external second-order work involving the external loading parameters and the internal second-order work. The mechanical origin lies in the distinction between the internal stress within the material and the applied stresses on the system's boundary. When the internal stress loses the capacity to balance the external stress, the specimen produces a dynamic response. An increase in kinetic energy was observed after a limit state was reached (axial or deviatoric stress peak), after application of a small additional axial load. Very good agreement was found with the integral method, whereas the method based on expansion series requires a small time range. Of course, for very large strains, corresponding to a substantial collapse of the specimen, the validity of the equation can no longer be tracked.

In the next chapter, a closer scale will be taken into account: the meso-structures inside the granular materials.

Chapter 4

Mesostructures & macroscopic behaviour of granular materials

4.1 Mesostructures in granular materials

An important choice to be made in this chapter is switching from 3D to 2D simulation. It is obvious that the 3D models provide the realistic result that engineers are interested in. However, the advantage of 2D models is that a 2D simulation runs more rapidly than a 3D simulation with equivalent or even more number of particles. This difference in computational effort arises because 2D particles have three degrees of freedom, while 3D particles have six. Moreover the number of contacts per particle is greater in the 3D case as contacts can develop anywhere along the particle surface, rather than being restricted to in-plane contacts, as in the 2D case. Particles in a 2D simulation will not experience out-of-plane forces and only moments acting about axes orthogonal to the analysis plane can be considered. As visualization of particle displacements and contacts force networks is much easier, 2D models can be more useful to study particle-scale mechanics in detail. Since this chapter is dedicated to the mesoscale investigation, 2D simulation is adopted.

4.1.1 2D numerical specimen

The static biaxial drained test (Figure 4.1) presented in this chapter is simulated using the software YADE. This model consists in a package of 20000 disks in a

rectangular box. There is no friction on the four walls. To prepare the package, first, the 20000 disks are randomly generated, after that the package is compressed by applying the isotropic stresses on the walls, $s_1 = s_2 = 100kPa$. The biaxial test is performed by applying a strain rate $\dot{\varepsilon}_1 = 0.01s^{-1}$, while the lateral stress is kept constant $\sigma_2 = 100kPa$.

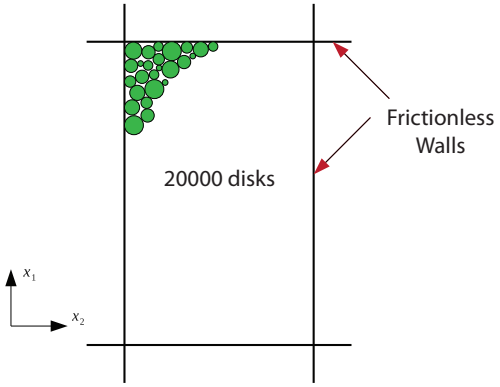

FIGURE 4.1: *The 2D model in YADE*

As presented in Chapter 2, the contact law is governed by three mechanical parameters: the normal stiffness coefficient k_n, the tangential stiffness coefficient k_t and the friction angle φ_c. For a pair of particles in contact, the normal force F_n is defined by k_n and the overlap between the two particles; there is no tensile force. The tangential force F_t is governed by the relative tangential displacement, multiplied by k_t, in compliance with the Coulomb's friction law $|F_t| \leq F_n \tan\varphi_c$. A scheme is recalled to explain the contact law that governs the interactions in Figure 4.2.

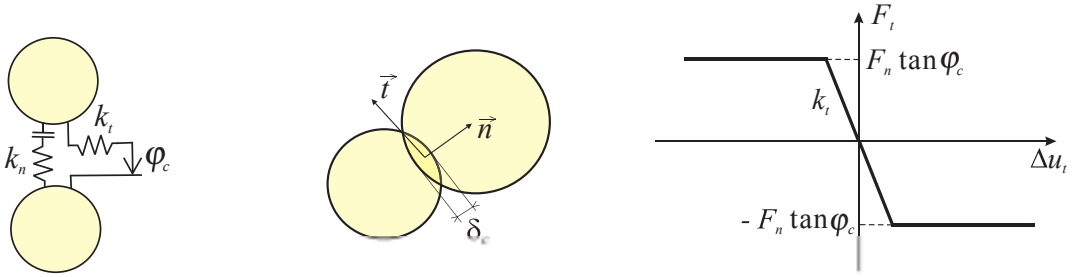

FIGURE 4.2: *The contact law of the interaction between the disks*

A summary of all the material parameters governing the contact can be found in table 4.1.

Number of particles	20000
Density of particles	3000 kg/m^3
k_n/D_s	5×10^9 Pa
k_t/k_n	0.42
φ_c	35^o
Porosity n (at isotropic state)	0.167 (dense)

TABLE 4.1: *Model parameters*

It is worth noting that the particles generated in YADE are basically spheres, however we can block the movement and rotation of the spheres on the third plane, to have the configuration of a 2D specimen. The result of the drained biaxial test is shown in Figures 4.3 and 4.4:

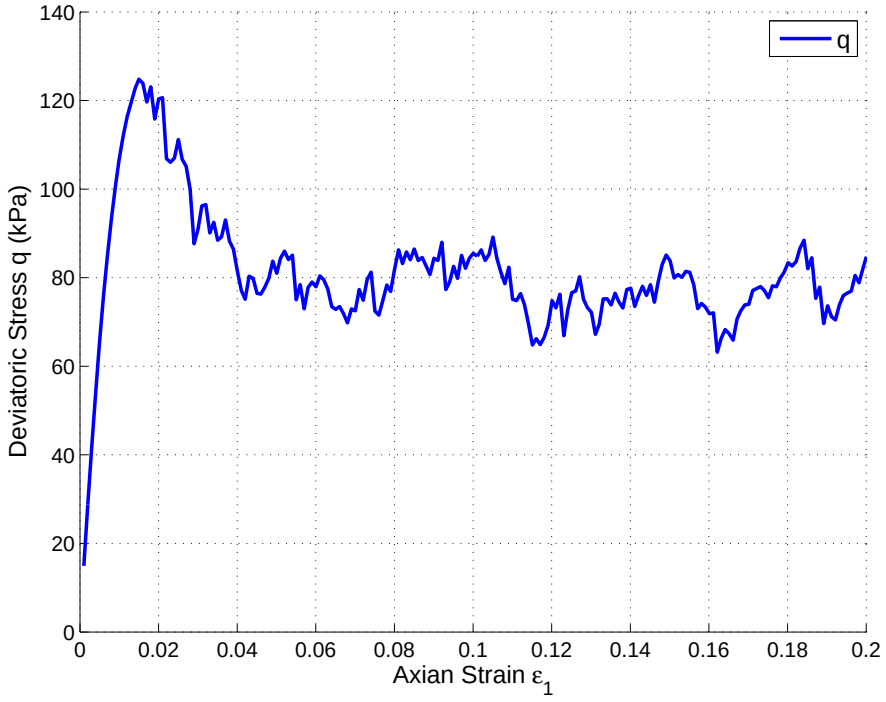

FIGURE 4.3: *Result of the drained biaxial test: deviatoric stress versus axial strain* ε_1

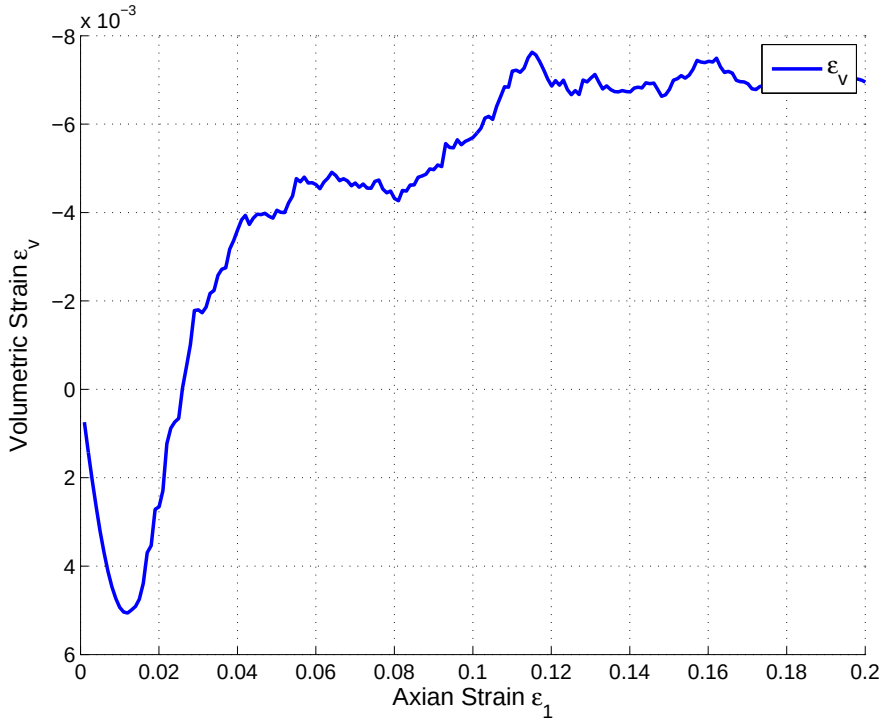

FIGURE 4.4: *Result of the drained biaxial test: volumetric strain ε_v versus axial strain ε_1*

The deviatoric stress curve reaches a peak at the strain state $\varepsilon_1 = 1.5\%$, after that, a softening phase is observed, and the curve tends to have a plateau until the end of the test. The simulation is stopped when the axial strain reaches 20%.

4.1.2 Force-chain and grain-loop

As previously mentioned in Chapter 1, this chapter investigates structures built inside granular materials on the meso-scale, involving force-chains and grain-loops. In this manuscript, the term "macrostructure" describes the specimen scale, the term "microstructure" describes the particle scale and finally the term "mesostructure" describes a structure that is built based on a set of particles in interaction into a certain kind of more complex structures: the particle interactions can form a quasi-linear pattern like the force-chain or they can assemble and form a grain-loop (Figure 4.5).

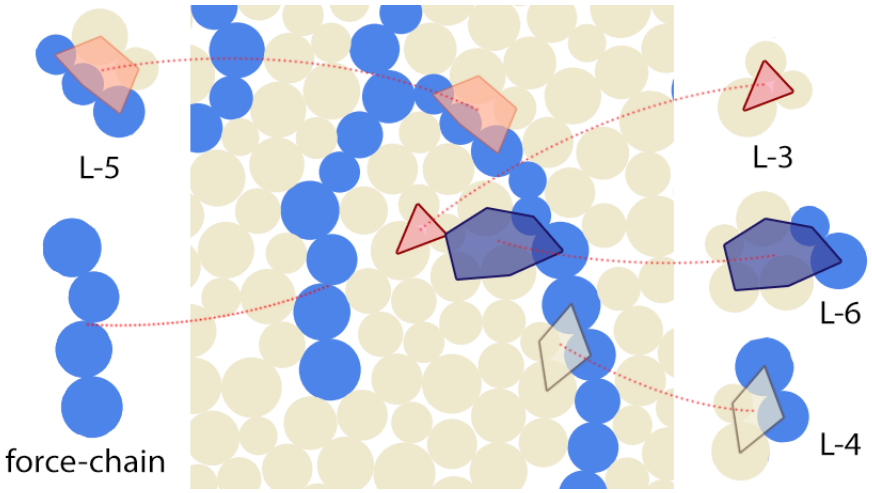

FIGURE 4.5: *Force-chains and grain-loops in the 2D specimen*

Several studies have been carried out to understand the behaviour and properties of mesostructures within the two-dimensional system: some authors study about the instability of force-chains (Hunt et al. [2010], Tordesillas and Muthuswamy [2009], Tordesillas et al. [2009]), or point out the correlation between the instability of force-chain and the development of the shear band in dense granular assemblies (Tordesillas [2007]); others mention about the relation between the evolution of force-chains and its relation with the grain-loop containing three particles (known as 3 grains cycle, in this thesis, this term is alternatively switched to grain-loop *L-3*). Force-chains are known as a system's response to external loading, and they are considered as the main ingredient deciding the strength of granular materials. While grain-loops can be directly considered as "the laterally supporting contact network" (Tordesillas et al. [2010a]). However, there are still some aspects that need to be carefully investigated, such as the relation between the force-chains evolution and the instability of granular material in the drained biaxial test of a dense specimen, or the correlation between the instability of force-chains and the variation of different kinds of grain-loops. This chapter demonstrates an effort to elucidate these issues.

Generally, force-chains and grain-loops have essential contributions to the macroscopic behavior of the system. Also, the relation between these structures plays an important role to the instability of the structure. The definition of these structures is explained in the following sections.

4.1.2.1 Definition of force-chain

It is important to distinguish the 'force network' and 'force-chain' in granular materials: within a numerical granular sample, whenever there is an interaction between two particles, we can define the branch vector connecting these two elements; by doing so for every interaction inside the specimen, a "force network" can be achieved (Figure 4.6 demonstrates the force network in a 2D specimen, thicker lines describe stronger contact force).

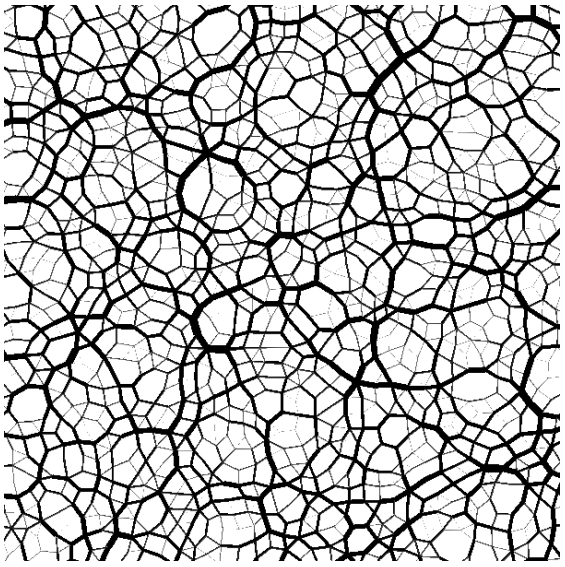

FIGURE 4.6: *Force network in 2D specimen (particles are hidden)*

However, inside this 'force network', the distribution of contact forces is not always homogeneous, especially in the 2D biaxial test, when the deviatoric stress is applied to the specimen. There are two coexisting phases that can be considered: the strong network and the weak network. Thus, the 'force-chain' is introduced.

In a granular medium, forces are transmitted via a two-phase network of contact forces: strong contact force network comprising of the force-chains, which bear the majority of the load; surrounding this is the complementary weak network of particles that provides lateral stability to the force chains (Radjai et al. [1998], Tordesillas et al. [2011b]). The force-chains are not intrinsically built inside the material, but are more likely in response to the external forces. Basically, the force-chain is a structure formed by the particles which satisfy three following conditions (Peters et al. [2005]):

1. The contact forces inside the force-chain must be from the strong interactions: the interparticles carry a force above the global average
2. A force-chain contains at least three particles
3. The particles inside the force-chain must create a quasi-linear pattern

Let us consider the first condition of the definition of a force-chain. For a particle inside the specimen, the stress tensor can be described as:

$$\tilde{\sigma}_{ij} = \frac{1}{V}\sum_{c=1}^{N^c} f_i^c r_j^c \tag{4.1}$$

where V is the volume of the particle, N^c is the number of contacts of the particle, f_i^c is the ith component of the force acting at the contact and r_j^c is the jth component of the radius vector from the center of the particle to the point of contact. Thus, the principal stresses can be defined by:

$$\sigma_1 = \frac{\sigma_{11}+\sigma_{22}}{2} + \sqrt{(\frac{\sigma_{11}-\sigma_{22}}{2})^2 + (\sigma_{12})^2} \tag{4.2}$$

$$\sigma_3 = \frac{\sigma_{11}+\sigma_{22}}{2} - \sqrt{(\frac{\sigma_{11}-\sigma_{22}}{2})^2 + (\sigma_{12})^2} \tag{4.3}$$

where the σ_{ij} are the components of the symmetric part of the particle stress, σ_1 is the major principal stress and σ_2 is the minor principal stress. It is worth to note that inside DEM, the convention of the stress is tension-positive, so the minor principal stress is the most compressive principal stress. We can define the direction of the major principal stress from the positive x_1 axis, θ, by the equation:

$$\tan(2\theta) = \frac{2\sigma_{12}}{\sigma_{11}-\sigma_{22}} \tag{4.4}$$

Figure 4.7 illustrates the direction of the most compressive principal stress of a particle

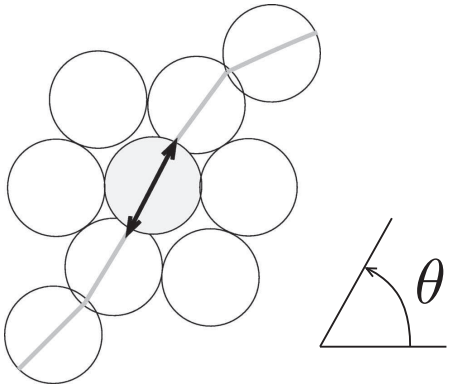

FIGURE 4.7: *Direction of the most compressive principal stress of a particle in a force-chain, θ is defined in equation (4.4) (Peters et al. [2005])*

For particles in a force-chain, they must carry large stresses compared to particles not in chains. It is generally accepted that only particles with contact forces (or equivalently, stresses) have magnitudes greater than the average value. Thus, a particle j can only be part of a force-chain if the magnitude of its minor principal stress is greater than the average, as described in equation (4.5):

$$\left|\sigma_2^j\right| > \frac{1}{N}\sum_{i=1}^{N}\left|\sigma_2^i\right| \tag{4.5}$$

where N is the number of particles, and $\left|\sigma_2^i\right|$ denotes the magnitude of the minor principal stress of particle i.

The second condition of forming a force-chain is a simple concept: one or two particles are not able to form a chain. The minimum quantity requires 3 particles.

The last condition is the "quasi-linear pattern" or similarly, a force-chain can be consider a "quasi-linear particle assemblies" (Campbell [2003]). Inside a force-chain, the directions of the minor principal stresses must form a quasi-linear line (Figure 4.8).

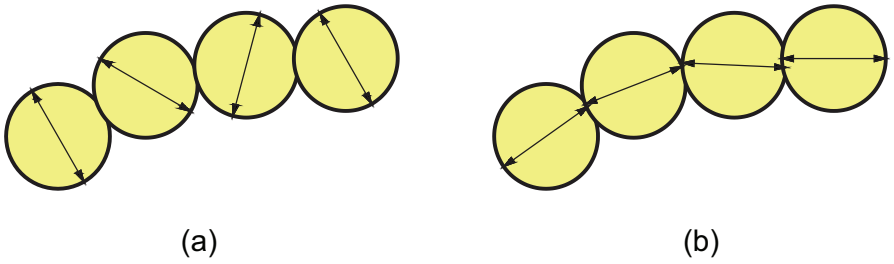

FIGURE 4.8: *Directions of the minor principal stresses of particles that can not form a force-chain (a) and can form a force chain (b)*

The algorithm is explained in following steps:

1. Read the interactions information of all particles
2. Filter out particles which have minor principal stress smaller than the average value
3. After that, filter one more time the particles that are not in contact with other highly stressed particles, also particles have less than two contacts
4. From the set of filtered particles, choose a starting grain then find the next particles in chain, while checking the quasi-linear pattern condition demonstrated in Figure 4.8

By looping the algorithm of force-chains detection on all particles within the granular specimen, we can define the location of all force-chains at each state. For example, an illustration of force-chains in 2D spherical particles specimen is shown in Figure 4.9.

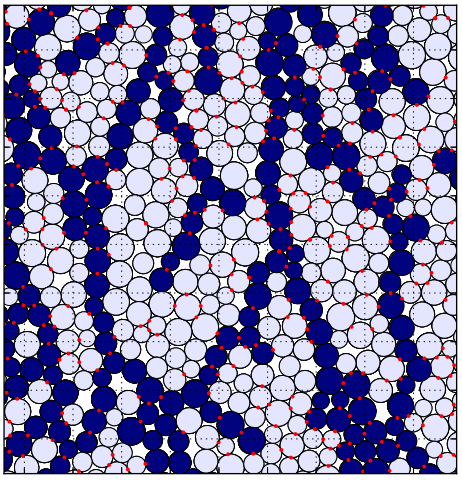

FIGURE 4.9: *Force-chains in 2D specimen (particles marked with dark blue color)*

4.1.2.2 Definition of grain loops

The next structure considered is the grain-loop. As mentioned previously, particles within the granular medium can form a linear pattern as the force-chain, but they can also form into a closed pattern. The grain-loop is a constructed structure based on a set of particles having interaction with each others, forming a closed cycle of particles in contact, the centers of which forming a closed polygonal line. In this thesis, the considered grain-loops involve the loop-3, loop-4, loop-5 and loop-6, as shown in figure 4.10. For the sake of simplicity, the grain loop-i is denoted L-i ($i = 3, 4, 5, 6$).

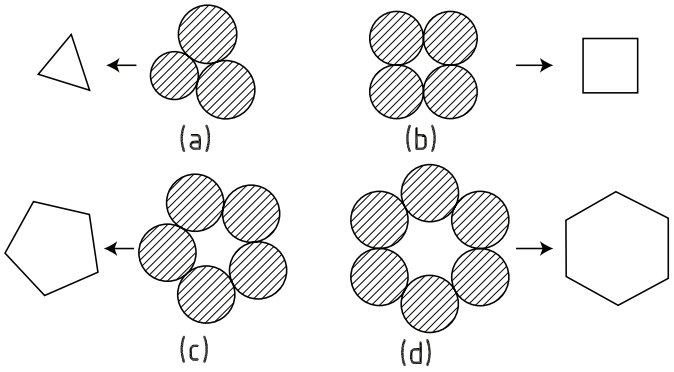

FIGURE 4.10: *Definition of grain loops L-3 (a), L-4 (b), L-5 (c) and L-6 (d)*

It is worth noting that, based on this definition, grain-loops can also be defined from the force-network map, where the triangle, the quadrangle, the pentagon and the hexagon correspond to grain-loops *L-3*, *L-4*, *L-5* and *L-6*, respectively (as demonstrated in Figure 4.10, grain-loops can be alternatively represented by vector branches connecting particles in contact). From the geometrical point of view, we can see that the grain-loop *L-3*, which the vector branches connecting the particles form a triangle, with this geometrical configuration, the ability to deform of this loop is restrained, since a small movement of one particle inside the loop can break the interaction and therefore the grain loop *L-3* is not available anymore; on the contrary, for the grain loop *L-6*, the vector branches connecting the particles form a hexagon, and the particles inside L-6 have more space to deform. The behaviour of the grain-loop can be greatly affected by their difference of deformability, therefore makes influence to the behaviour of the granular system.

To detect and classify the grain-loops inside the 2D granular specimen, we apply a modified technique of the so-called *mini cycle basis* algorithm (Mehlhorn and Michail [2007]) to the contact network built from the interactions between grains (the grain-wall contacts are not taken into account). It is worth noting that some other authors use the terminology "cycle" instead of "loop" to describe this kind of mesostructures, therefore in this manuscript, *mini cycle basis* is equivalent to *mini loop basis*. The brief description of the mentioned algorithm is presented below:

Let us consider $G(V, E)$ an undirected unweighted graph with m edges, n vertices and κ connected components, T be any spanning forest of G. A *loop* C of G is any subgraph in which each vertex has even degree. Each loop is associated with an *incidence vector* x, indexed on E, where $x_e = 1$ of e is an edge of C and $x_e = 0$ for other cases. The vector space generated by the incidence vectors of loops is called the *loop space* of G, and has dimension $N = m - n + \kappa$. A maximal set of linearly independent loops is called the *loop basis*.

The weight of a loop is the sum of the weights of its edges, and the weight of a loop basis is the sum of the weights of its loops. For the unweighted case, this is simply a count of number of edges. The minimum loop basis is the loop basis of minimum weight in a graph.

Let $\{e_1, ..., e_N\}$ be the edges of $G \backslash T$ in some arbitrary but fixed order.

For each vertex v and edge $e = (u, w)$, construct the loop $C = SP(v, u) + SP(v, w) + (u, w)$, where $SP(a, b)$ is the shortest path from a to b. If these two

shortest paths do not contain a vertex other than v in common, then keep the loop and add it to a set of loops defined as the *Horton set*. The Horton set always contains a minimal loop basis, but not necessarily all the loops that belong to any minimal loop basis. By processing, uniqueness of the minimal loop basis is achieved by ensuring shortest path distances of G are unique.

The minimal loop basis is then extracted from the Horton set by using the orthogonality of the cycle space. The inner product $\langle C, S\rangle$ represents the standard inner product of vectors, acting on subgraphs C and S in terms of their incidence vector.

The complete details of this algorithm and comparisons with other algorithms can be found in Mehlhorn and Michail [2007].

For sparse graphs, such as those we encounter in complex networks of granular systems, this is the best known algorithm for computing a minimal loop basis.

Algorithm 1 Algorithm for building minimal loop basis

```
Ensure uniqueness of shortest path distances of G
Construct superset (Horton set) S of Minimal Loop Basis
Set S_i = {e_i} for all i = 1, ..., N
for i = 1 to N do
    Find C_i as the shortest loop in S such that ⟨C_i, S_i⟩ = 1
    for j = i + 1 to N do
        if ⟨S_j, C_i⟩ = 1 then
            S_j = S_j + S_i
        end if
    end for
end for
return S is the minimal loop basis
```

4.1.2.3 Relation between force-chains and grain-loops

The medium around the force-chains is comprised of the grain-loops. By the fact that force-chains exist conjoined with grain-loops, force-chains and grain-loops share a mutual relationship, they are the essential mesostructures in the 2D granular medium (Figure 4.5). Several studies have pointed out the connection between the stability of force-chains with the grain-loop *L-3* (Tordesillas et al. [2011a]), where grain-loop *L-3* "are stabilizing agents that act as granular trusses to the load-bearing force-chain columns". There are still some missing aspects

needing to be investigated, for example: the role of bigger grain-loop (grain-loop *L-6*) to the instability of force-chains, which is discussed in the following section; or by taking into account a stability criterion to compare the strength of the grain-loops (Chapter 5).

4.2 Correlation between the variation of mesostructures and macroscopic behavior of granular materials

The investigation of mesostructures in this section is carried out based on the biaxial test introduced in Section 4.1.1. In this investigation, the number of force-chains N_{fc} and grain-loops $N_{\text{L-i}}$ are captured and compared with the deviatoric stress ($q = \sigma_1 - \sigma_2$) and the volumetric strain $\varepsilon_v = \varepsilon_1 + \varepsilon_2$, respectively. Since the force-chain is basically built based on the force criterion, N_{fc} is compared with q; while the grain-loops are defined based on their geometry settings, $N_{\text{L-i}}$ is compared with ε_v. The results are shown in Figures 4.11 and 4.12.

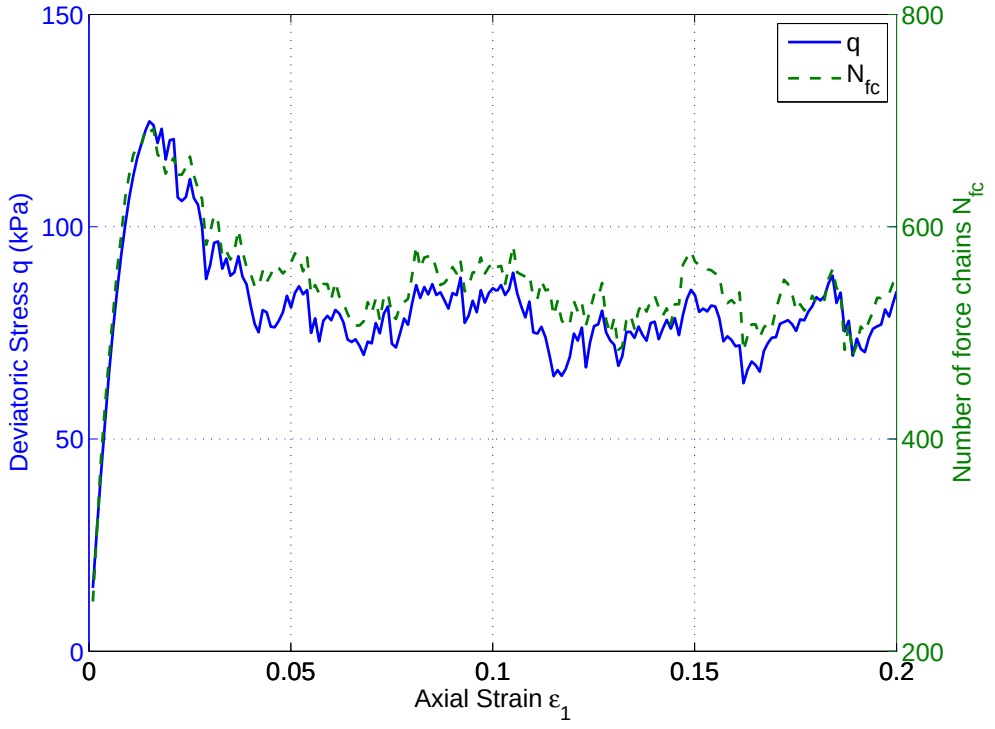

FIGURE 4.11: *Comparison between the deviatoric stress q and the total number of force-chains in the biaxial test*

The result from Figure 4.11 indicates that the macroscopic behaviour (deviatoric stress) of specimen changes in accordance with the variation of the microstructure (number of force-chains): when the test begins, an increase is found until reaching a peak, after that, there is a softening phase, tending to stabilize afterward. Force-chains appear to show as the material's capacity to sustain the external load: when the deviatoric stress rises, interactions between particles inside the material create force-chains as a response to the external deviatoric stress. As soon as force-chains collapse, the specimen loses its capacity and reaches the limit state.

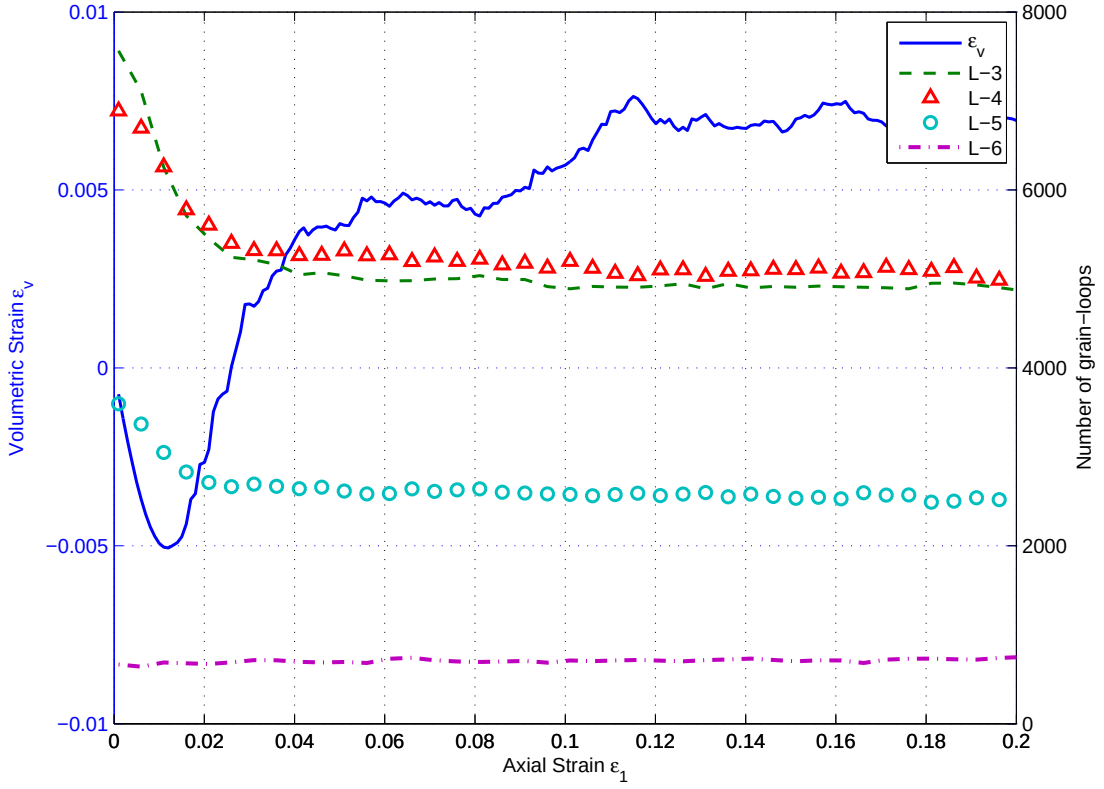

FIGURE 4.12: *Volumetric strain ε_v and the variation of the number of grain loops*

Meanwhile, the variation of the number of grain-loops shows a close correlation with volumetric strain of the system. As demonstrated in Figure 4.12, when the specimen is under compressive loading, the number of grain-loops changes accordingly: at the beginning, the stable *L-3* dominates the global loop number and *L-6* is less noticeable; when the deviatoric stress is applied, the number of *L-3* quickly decreases and *L-6* slightly increases during loading to peak shear stress. After that, when ε_v is constant, the number of all grain-loops is also stable.

As can be seen in the diagram, the numbers of grain-loops *L-4* and *L-5* share a similar evolution as *L-3*. Therefore, in this manuscript, the investigation is concentrated only on the loops *L-3* and *L-6*.

4.3 Instability of force-chains in granular material

4.3.1 Definition of force-chain buckling

The force-chains can be eliminated under the "buckling" mechanism, where the geometry condition is no longer satisfied (for instance, see Tordesillas [2007]): under this circumstance, a force-chain cannot form a quasi-linear line any longer. The buckling mechanism of a force-chain is described by taking a segment of 3 particles inside a chain, between two continuous states considered; the buckling angle θ_b between the branch vectors can be computed as shown in Figure 4.13.

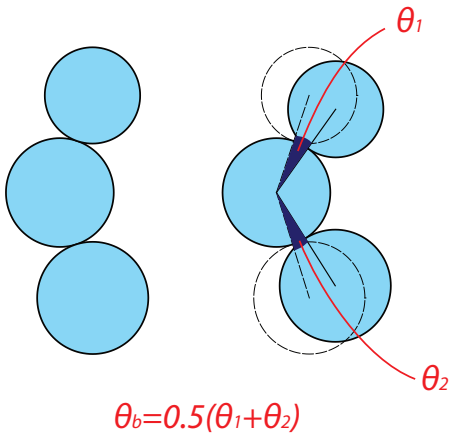

FIGURE 4.13: *Calculation of the buckling angle θ_b in the 3-particle segment in a force-chain. If this buckling angle exceeds the threshold, the force-chain is considered as buckling.*

When θ_b exceeds some prescribed threshold $\hat{\theta}_b$, the whole force-chain is considered buckled and no longer available. In this manuscript, three threshold values are used for the investigation $(0.5°, 1°, 2°)$, the result of the buckling events is shown in Figure 4.14.

In this segment of 3 particles, when the buckling event occurs (the buckling angle exceeds the chosen threshold), the middle grain is called the *buckling grain*, this grain is considered as the point where the force-chain collapses.

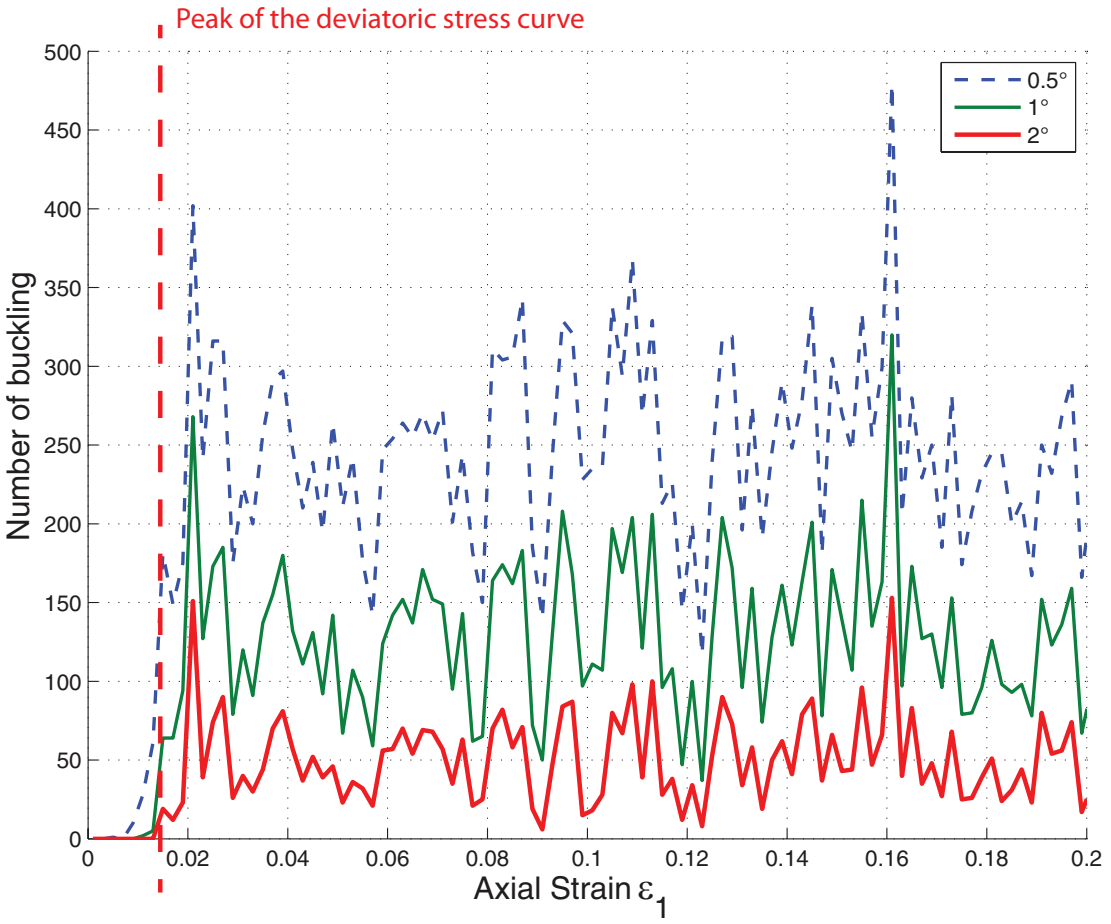

FIGURE 4.14: *Numbering of buckling events during the biaxial test*

Before the peak of the deviatoric - axial strain curve, force-chains are the main ingredient that bear the external load, even though there are some buckling events of force-chains in this state (as can be seen in the diagram 4.14, at the beginning state of the test where $\varepsilon_1 < 1\%$, there is no force-chain buckling). The drop of number of force-chains, or equally, the rise of buckling events, leads the specimen to an unstable state (in Figure 4.14), as can be observed when the axial strain $\varepsilon_1 \in [0.01, 0.015]$.

It is obvious that, when choosing a lower value of the threshold $\hat{\theta}_b$, a larger number of buckling events can be found. However, with whatever value, the result shows a same trend: from the isotropic state, there is no buckling of force-chains, after that in the hardening phase (before peak of the curve q), there are few buckling events of the force-chain, then the deviatoric curve reaches its peak; when the buckling events rise considerably, the specimen is unstable.

For the sake of simplicity, the force-chains are considered buckled when θ_b is bigger than the threshold value $\hat{\theta}_b = 1°$. This value for the force-chain buckling detecting algorithm is physically reasonable choice (Tordesillas et al. [2011a]).

4.3.2 Correlation between the evolution of force-chains and macroscopic behaviour

The force-chains appear as a response of the granular medium to the external loading (Radjai et al. [1998], Tordesillas [2007], Tordesillas et al. [2009]). In the biaxial test, a direct relation exists between the number of force-chains and the deviatoric stress. Consequently, the instability of force-chains plays an important role in the macroscopic failure of the specimen: the buckling event rises after the peak of the curve $q - \varepsilon_1$. In this case, even when the test is under a quasi-static regime, the kinetic energy of the system can be considered to identify the instability of the material.

This section investigates the correlation between the buckling of force-chains and the variation of kinetic energy calculated from the interactions between particles. The comparison result is demonstrated in Figure 4.15

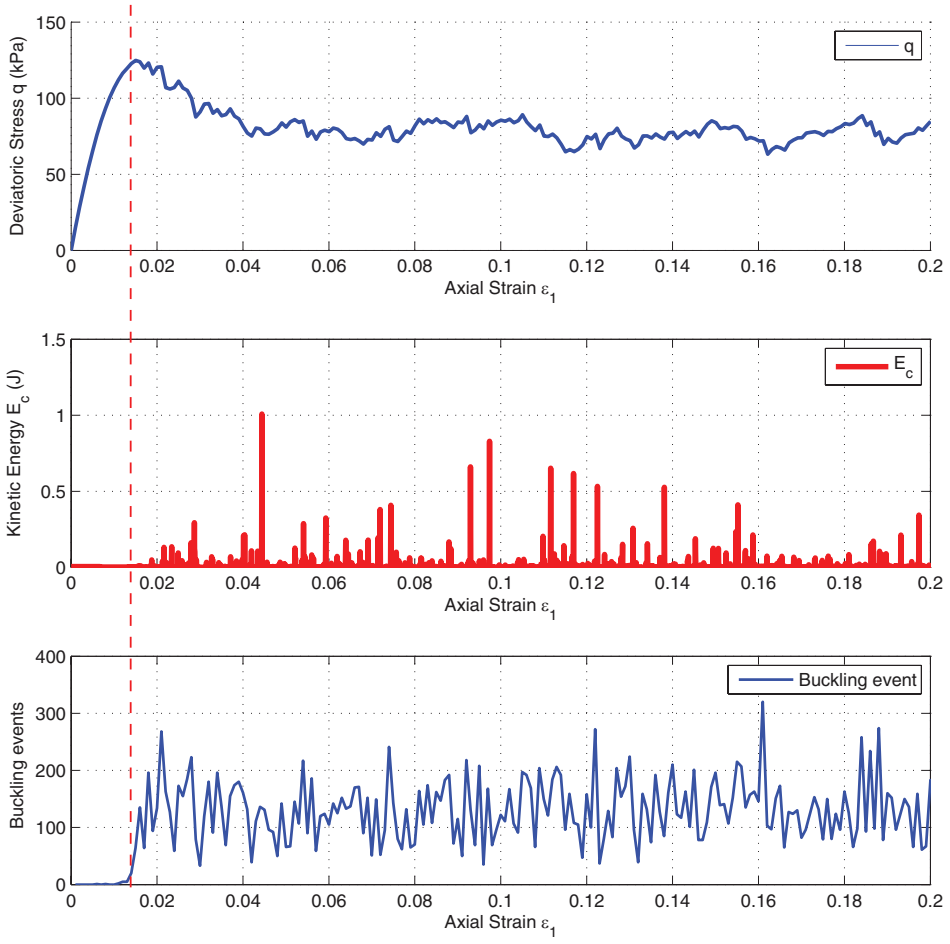

FIGURE 4.15: *Variation of kinetic energy E_c and evolution of buckling events during the biaxial test*

As can be seen in the diagram 4.15, the kinetic energy remains small and is negligible when the biaxial test is in the hardening phase (before the peak of the curve $q - \varepsilon_1$), however, as soon as q begins to drop, E_c rises accordingly. It is worth noting that when the number of force-chains N_{fc} begins to decrease, the specimen reaches a limit state: the deviatoric curve reaches its peak.

The problem at hand now is to find the relation between the number of the buckling of force-chains and the evolution of the kinetic energy E_c. From both results of E_c and N_{fc}, it is clear and sound to conclude that as soon as the force-chains buckle, the value of the kinetic energy is no longer negligible. It can be explained that when the re-arrangement of the particles causes the buckling of force-chains and gives rise to the kinetic energy, the specimen is no longer stable. By looking at

the comparison between the buckling event with the evolution of kinetic energy (Figure 4.15): the buckling events almost do not occur before the peak of q, also E_c is negligible; however, E_c increases when the buckling events take place in the specimen.

We have a brief conclusion of what we achieved: the establishment and buckling of force-chains in the classical drained biaxial test show a close correlation with the increase and decrease of deviatoric stress. The force-chains begin to build themselves along with the increase of the deviatoric stress (before peak), after that, when buckling of force-chains happens (means the total number of force-chains begins to drop, and buckling number begins to increase), the deviatoric stress turns to softening phase (post peak). Moreover, the evolution of kinetic energy E_c shows a close relation to the instability of force-chains: when the force-chains are stable, the kinetic energy remains small, however, when the buckling event happens, E_c increases and is no longer negligible. The result of this investigation in the quasi-static case can be extended to the dynamic case, where the force-chains can be used as a good approach to analyze the microstructure of a granular system under a dynamical load.

4.4 Relation between the existence of force-chains and attached grain-loops

As discussed in previous sections, the macroscopic behaviour has a steady correlation with the evolution of the mesostructures (force-chains and grain-loops). But what is the relation among mesostructures themselves? The condition to consider the longevity of force-chains and grain-loops might be different; however, inside the granular material, and in particular: force-chains and the environment around them, the relation between force-chains and grain-loops cannot be neglected. For this purpose, this section makes an effort to elucidate the relation between grain-loops and force-chains by considering what effect the grain-loops might have on force-chains during their longevity, the so-called *force-chain lifespan*.

4.4.1 Lifespan of force-chains and attached grain-loops

The lifespan of a force-chain can be defined as a recorded time span, or series of continuous recorded strain states, which begins from the moment that one single force-chain is initially built till the moment it buckles and is no longer available in the specimen. Consequently, each force-chain has a unique lifespan, and it is obvious that the lifespans of force-chains have different durations.

In order to investigate the relation between force-chains and grain-loops, we need to distinguish grain-loops into two groups: grain-loops that share something with the force-chains and individual grain-loops who do not have any connection with force-chain. Therefore, the next terminology *attached grain-loops* is introduced. As demonstrated in Figure 4.9, when the force-chains are built inside the specimen, they are always surrounded and supported by surrounding grain-loops [1]. Grain-loops that share at least one particle (in other words, the grain-loop that shares interactions with the force-chain) are defined as *attached grain-loops*. Let us take a single force-chain as an example, see Figure 4.16.

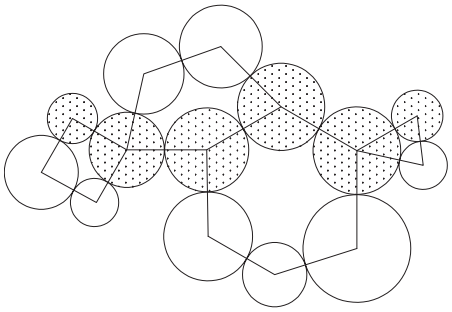

FIGURE 4.16: *Force-chain (particles marked with dotted pattern) with attached grain-loops*

This single force-chain has 4 grain-loops which share one or more particles with it; in other words, these grain-loops are attached to the force-chain. This force-chain is supported by these grain-loops: from the grain-loop *L-3* to the bigger grain-loop *L-6*. During the lifespan of the force-chain, the number of these attached grain-loops varies. This relation can quantitatively be expressed by introducing the ratio β_i:

[1] There are also single grains – – sharing contact with the force-chain, but their contribution is not noticeable

$$\beta_i = \frac{N_{L-i}}{N_{L-3} + N_{L-4} + N_{L-5} + N_{L-6}} \tag{4.6}$$

where N_{L-i} is the number of attached grain-loops L-i to the considered force-chain ($i = 3, 4, 5, 6$). Consequently, the higher β_i is, the more attached grain-loops of type L-i are found surrounding this force-chain. Applying this equation to the example in Figure 4.16, we have $\beta_3 = 0.25$, $\beta_4 = 0.25$, $\beta_5 = 0.25$, $\beta_6 = 0.25$.

For all force-chains inside the specimen, the ratio β_i can be computed at each strain state; then, by tracking the variation of β_i during the force-chains lifespan, we can find the relation between attached grain-loops and force-chains during force-chains living duration. By doing so, each force-chain's lifespan produces a set of β_i. However, since each force-chain has its own lifespan duration, some force-chains live only for few 2 or 3 states, others live longer; then in order to summarize the relation (grain-loops versus force-chain lifespan) for all of force-chains within the specimen, the lifespan of each force-chain can be normalized to $[0, 1]$, where 0 is the moment the force-chain is created and 1 is the moment it buckles. By doing so, β_i can be computed for all force-chains and is demonstrated in one diagram. The result for the evolution of β_3 is shown in Figure 4.17. The diagram represents the fitting curve of the value of β_i of all force-chains in corresponding phases (global – the whole test; or divided into hardening, softening and ultimate phases).

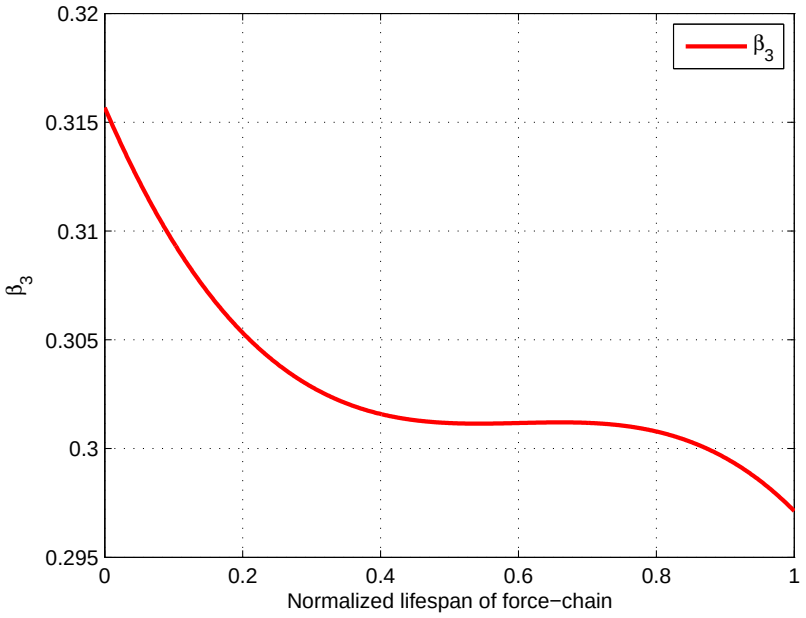

FIGURE 4.17: *Evolution of β_3 versus the normalized lifespan of force-chains*

As can be seen in the diagram, β_3 decreases over time. This result indicates that, during the lifespan of force-chains, the ratio between the attached grain-loops *L-3* to the sum of all attached grain-loop tends to decrease gradually. In other words, it means that: at first, when the force-chains are built and are still stable, they are supported by more strong grain-loops (*L-3*), after that, the force-chains are less and less supported by the grain-loops *L-3* and become weaker.

For the attached grain-loops *L-6*, the result is shown in Figure 4.18.

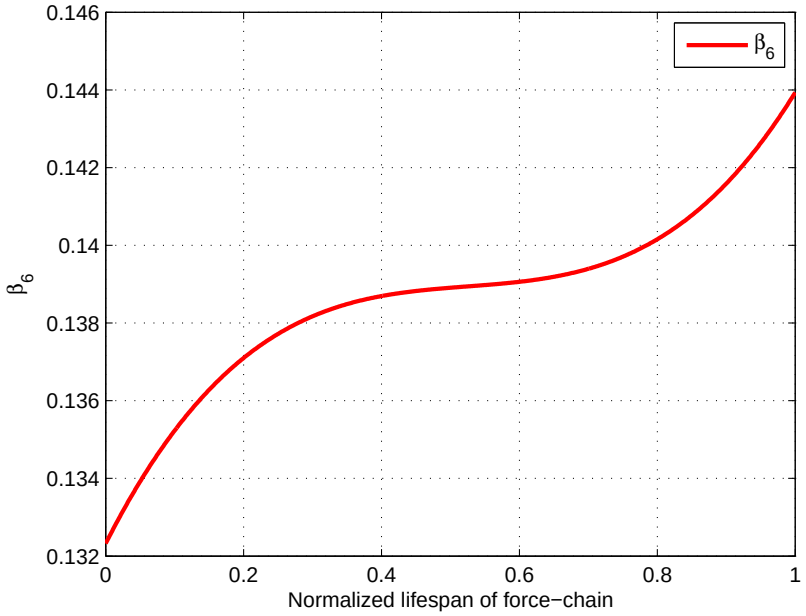

FIGURE 4.18: *Evolution of β_6 versus the normalized lifespan of force-chains*

Firstly, the result shows that, in accordance to the global number of grain-loops, where *L-3* dominates *L-6* (Figure 4.12), the attached grain-loops around the force-chains show the same trend: the ratio β_3 surpasses β_6. Furthermore, during the lifespan of force-chains, β_6 increases over time, it has an opposite evolution to β_3. This can be explained by the fact that, when the force-chains are weaker and buckles, they are surrounded by the grain-loops *L-6*, therefore this leads to the instability of the force-chains. Moreover, this result leads to a conclusion that, the surrounding environment of the force-chains tends to increase its deformability: the more *L-6*s are found, the more deformable the force-chain is.

Because force-chains are the response of the granular package to external loading, different states of the specimen might correspond to different behavior of force-chains in these states. To be more specific, we can investigate the variation of β_3

and β_6 of the force-chains by separating them into different phases of the deviatoric stress: hardening phase (before peak), softening phase (after peak) and ultimate phase (the plateau of the curve) (Figure 4.19).

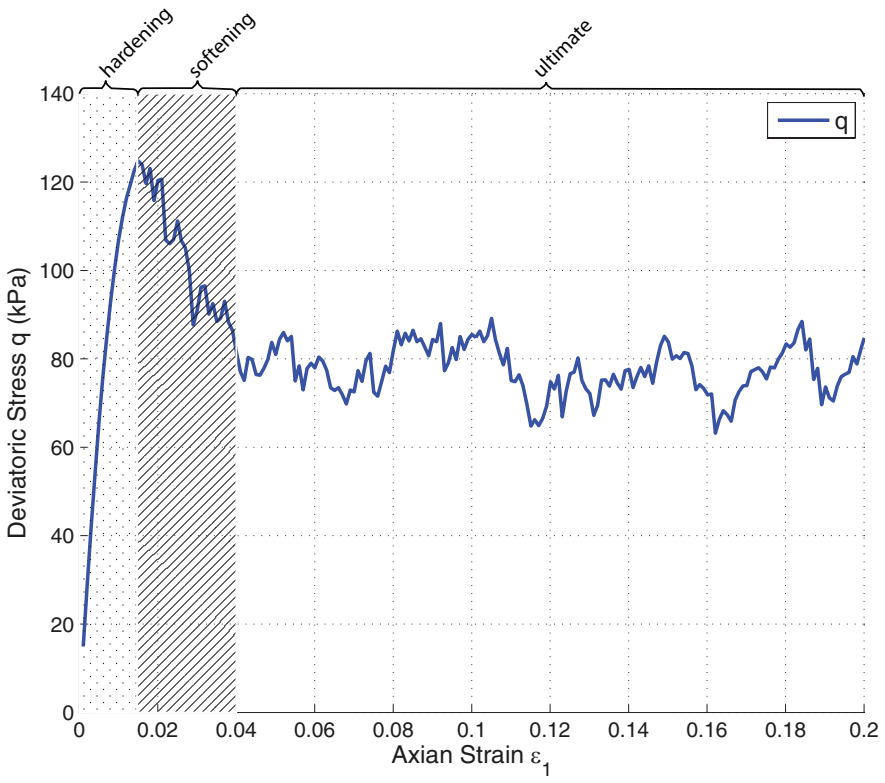

FIGURE 4.19: *Phases in the drained biaxial test: hardening, softening and ultimate*

In the *hardening phase*, as can be seen in previous result (see Figure 4.11) the number of force-chains increases along with the increment of the deviatoric stress till its peak, in this phase, most of the force-chains are supposed to be stable and buckling events are less noticeable. The result in Figure 4.20 demonstrates the variation of β_3 and β_6 during the lifespan of force-chains in the hardening phase.

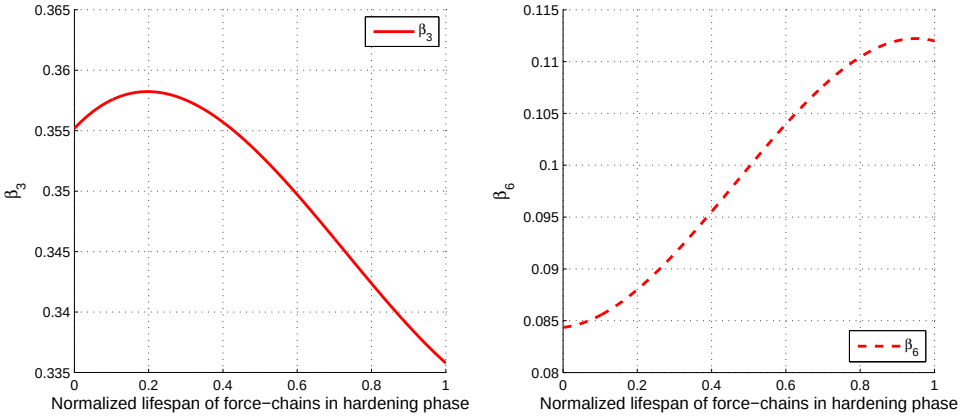

FIGURE 4.20: *Evolution of β_3 (left) and β_6 (right) of the force-chains in the hardening phase (zoom)*

In the *softening phase*, the trend keeps unchanged (Figure 4.21). However, when being compared with the hardening phase, β_6 rises (from $[0.085, 0.114]$ to $[0.123, 0.15]$), due to the fact that the number of global grain-loops *L-6* increases. In this phase, during the lifespan of force-chains, they are first surrounded and supported by the attached grain-loops *L-3*, then, the attached *L-3* decreases over time, while the number of attached grain-loops *L-6* increases (Figure 4.21).

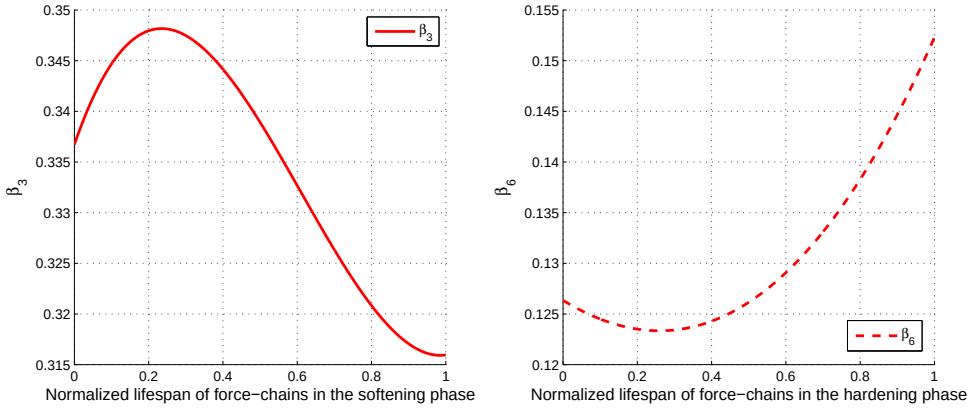

FIGURE 4.21: *Evolution of β_3 (left) and β_6 (right) of the force-chains in the softening phase (zoom)*

The result in the *ultimate phase* is shown in Figure 4.22. This phase is a special one, after the softening phase, the number of force-chains, the number of grain-loops are almost stable and the specimen reaches a critical state (for more detail on the appearance of a shear band, see Chapter 5). That is to say, the ratio β_i is now affected only by the interaction between force-chains and attached grain-loops. The force-chains in this stage are stilling building and buckling, but not as

significant as other phases. The variation of β_3 and β_6 has a same behavior at the beginning of the lifespan of force-chains, however, they keep having a stable value until the end (Figure 4.22).

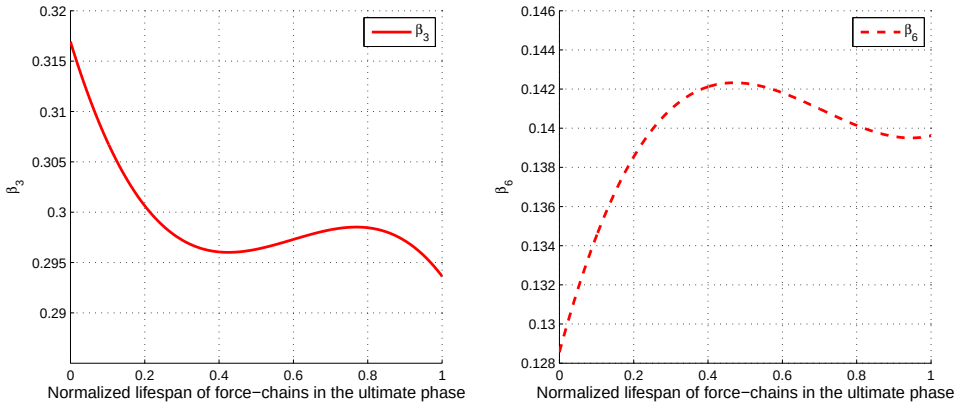

FIGURE 4.22: *Evolution of β_3 (left) and β_6 (right) of the force-chains in the ultimate phase (zoom)*

Finally, to point out the different variations of β_3 and β_6 through different phases of the specimen, a comparison is carried out: values of β_3 in different phases are compared (Figure 4.23(a)), and the same for β_6 (Figure 4.23(b)). Two things can be concluded from this results: **(a)** β_3 and β_6 have contrary trends. From hardening → softening → ultimate, an decrease of β_3 is observed, while β_6 increases. This is logical, since during the test, the global number of grain-loops *L-3* decreases and the number of *L-6* slightly increases. **(b)** In 3 phases, β_3 and β_6 have steady development: during the lifespan of force-chains, the curves of β_3 have descending slopes, while the curves of β_6 have ascending slopes.

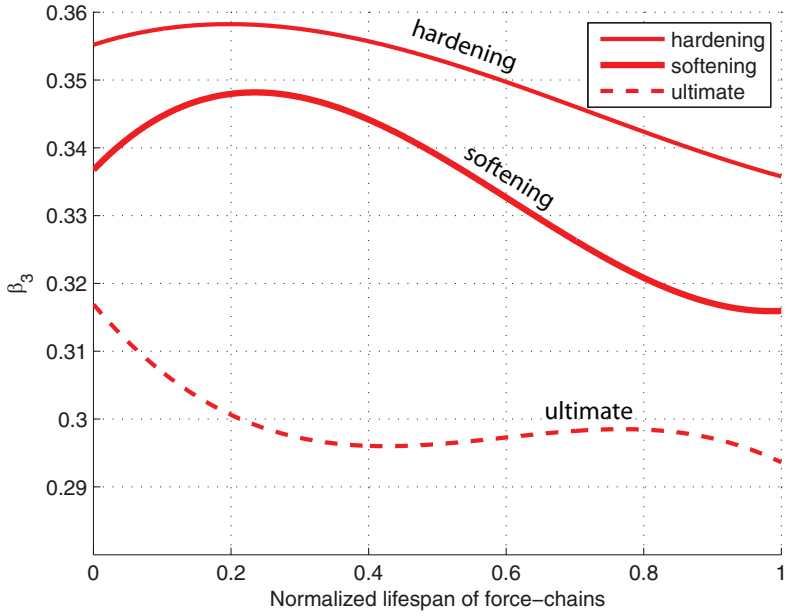

(a) Variation of β_3

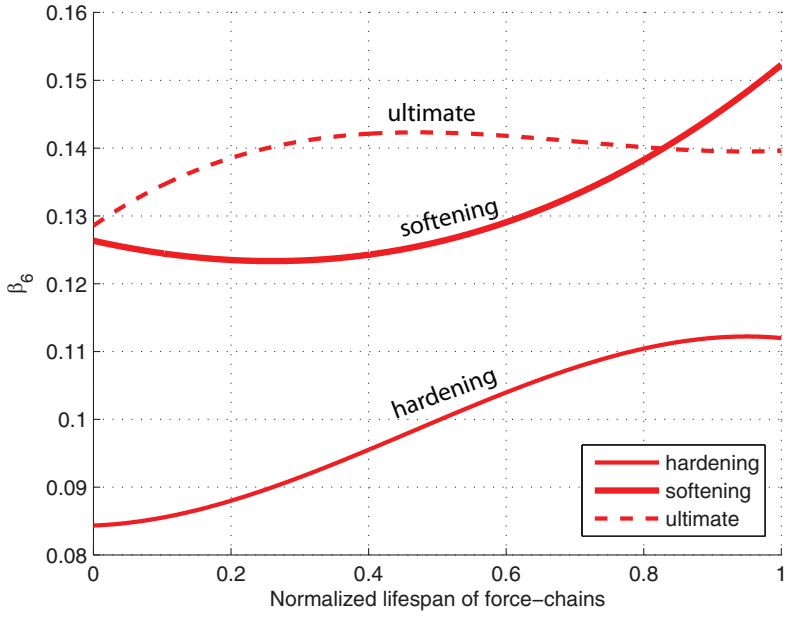

(b) Variation of β_6

FIGURE 4.23: *Variation of β_3 and β_6, compared separately in 3 phases*

To conclude, force-chains are built and supported by the attached grain-loops surrounding them. During the force-chain's lifespan, its relation with the supporting grain-loops changes accordingly. The force-chain, overtime, becomes weaker

and is eliminated by the buckling mechanism; when the number of attached *L-3* decreases and attached *L-6* increases, force-chains buckle.

4.5 Buckling of force-chains and local void ratio

This last section dedicates to the investigation of the relation between the buckling of force-chains and the local void ratio around the buckled force-chains. A force-chain is buckled when it cannot maintain the geometric stable condition. This phenomenon happens when there is a rearrangement of particles inside the force-chain itself. However, it is obvious that the rearrangement of particles happens not only inside the force-chain but also happens within the surrounding particles. Thus, it is necessary to investigate the environment around the buckled force-chain; not only the individual relation between a force-chain and its attached grain-loops, but on a larger scale. One of the possible investigation is the local void ratio around the buckling grain (the definition of the *buckling grain* is presented in Section 4.3.1).

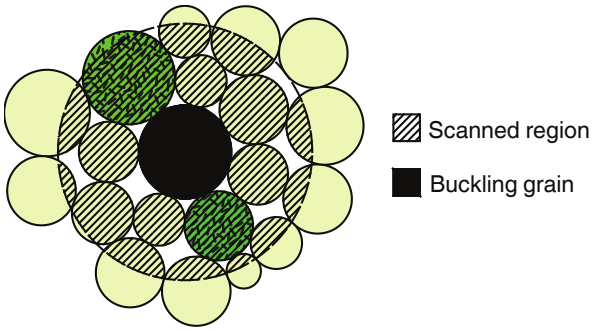

FIGURE 4.24: *Local area used to calculate the void ratio around the buckling grain*

The method of computing the local void ratio is adopted from the proposition of Cambou et al. [2013], O'Sullivan [2011]. Let us consider the buckling grain of a force-chain (see Figure 4.24). From this predefined point, an area can be therefore defined by taking it as the center, then drawing a circle with a chosen radius ($r_{scan} = 3\langle D_s \rangle$, where $\langle D_s \rangle$ is the average particles diameters). In this manuscript, this zone is called *buckling zone*. Then, the local void ratio around the buckling point can be defined as:

$$e = \frac{A_s}{A_v} \tag{4.7}$$

where A_s and A_v are the area of the solid and void within the scanning zone, respectively. When the *buckling zone* of all buckling grains is defined, the rest of the specimen is defined *non-buckling zone*, or *normal zone*.

The result shown in Figure 4.25 demonstrates the comparison between the average void ratio of *buckling zone* and the average void ratio of the *non-buckling zone*.

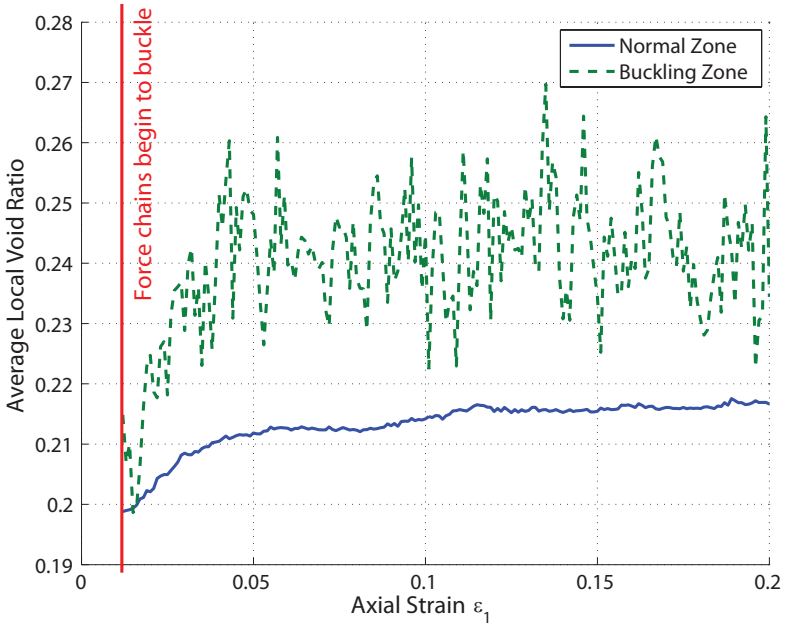

FIGURE 4.25: *Comparison of the local void ratio between the buckling zone and non-buckling zone*

As can be seen in the diagram, the average void ratio of the *buckling zone* is larger than the void ratio of the rest of the specimen. This result shows that: inside the *buckling zone*, the specimen has a loose pattern, meanwhile, outside the *buckling zone*, a denser pattern is found.

By pairing this result to what we achieved in Section 4.4.1, it is observed that the collapse of force-chains shares a strong relation with the surrounding environment known as the attached grain-loops. When the collapse of force-chains occurs, the neighborhood particles rearrange and turn to a looser pattern; this can be considered the same effect as the variation of support elements of force-chains: the

attached grain-loops change from *L-3* to *L-6*: at the end of force-chains lifespan, the number of *L-3* decreases, giving space for *L-6* to increase.

4.6 Conclusion

This chapter has went through the investigation of the mesostructures within the granular material, by investigating the biaxial drained test applying on a 2D dense specimen. Involving force-chains and grain-loops, the mesostructures are proven to have a close correlation to the macroscopic behavior of the sample. Firstly, the variation of force-chains and grain-loops changes in accordance with the macroscopic behavior. Force-chains are responsible for the strength of the granular material: the strength of granular system increases/decreases due to the establishment/disappearance of the strong force network (a.k.a force-chains). Force-chain is the main ingredient that governs the microstructure of the granular medium. Moreover, the buckling of force-chains is related to the increase of kinetic energy of the sample. Secondly, the instability of force-chains is strongly influenced by the surrounding environment, which consisting of grain-loops. It is also proven that, around buckled force-chains, a looser pattern can be found. In this surrounding environment, there are grain-loops that support force-chains. When a force-chain is created, it is supported by a greater number of attached grain-loop L-3; however, this quantity decreases over time until the force-chain is buckled. On the contrary, bigger attached grain-loops L-6 have an opposite development, they have a small number at the early state of the force-chain lifespan, then this number increases till the force-chain is buckled.

Chapter 5

Instability of mesostructures: second-order work investigation

5.1 Introduction

The failure in granular materials on the macroscopic scale (specimen scale) is strongly connected to the inter-particular mechanisms appearing and developing within the material (Kuhn [2010], Nicot et al. [2012b], Tordesillas [2007], Tordesillas et al. [2010b]). Therefore, it is essential and fundamental to have a closer look to the local aspect of the failure (into the particle scale and contact scale), by building a micromechanical formalism bridging both microscopic and macroscopic scales (Hadda et al. [2013]).

It is important to note that, in granular materials, two scales (macroscopic and microscopic) depend on each other mutually. When an external force is applied on the boundary of the sample, it is transmitted from the particles at the boundary (macro scale) to the center of the sample by the force network created from the inter-particulate contact forces; this force network is the main ingredient that governs the kinematics of particles (movement and rotation) through constitutive equation and physical laws (contact laws, internal friction angle, degrees of freedom, non uniform distribution of local variables...), which return the macroscopic strain. Moreover, the failure can be triggered from microscopic scale as a local instability inside the specimen then be amplified to the whole sample. After that, the failure can be detected on the macroscopic scale by a burst in kinetic energy (in

some cases) and the vanishing of the stress acting on the boundary if a convenient control mode is adopted (Chapter 3).

On the microscopic scale, many studies have been carried out in order to describe the physics of the microstructural behaviour and try to elucidate the failure happening inside granular medium from micromechanical approaches (Radjai et al. [1999], Tordesillas et al. [2010a]). The description of the micromechanical behavior of granular media covers the description of the structure (position of grains and contact points), the local kinematics (Tordesillas [2007]) (displacements, rotations), also the description of the strong contacts network, involving the force-chains (Radjai et al. [1999, 1998]). Several authors have studied several aspects of the micromechanics of granular media for different purposes: some authors try to validate the micro-macro mechanical approaches and constitutive relations of the material (Kuhn [2010], Oda [2004], Oda and Iwashita [2000], Radjai et al. [1999]), or to predict the appearance of the shear-band (Antony et al. [2004], Gardiner and Tordesillas [2004], Kuhn and Bagi [2004, 2005]) or to predict the instability occurrence within granular materials (Tordesillas et al. [2011a], Walker and Tordesillas [2010]). However, the link between the macroscopic scale and the microscopic scale still needs more attention, therefore it is crucial to put forward an efficient tool at the local scale to investigate the physical origin of the failure which can be related to the vanishing of the global second-order work.

In fact, the vanishing of the second-order work (Hill [1958]) is a necessary condition for the failure to occur (Nicot et al. [2007, 2011, 2009]), it also allows us to determine which is the direction of the loading applying on the system that leads to the failure (Nicot et al. [2011]). In order to apply this theory to the microscopic scale, the link between the macroscopic second-order work and the second-order work computed from the microscopic variables implying the contact forces and the position of particles has been developed (Nicot et al. [2012a]). This approach allows us to investigate the failure of the system from a microstructural point of view, and describes the local mechanism governing the vanishing of the second-order work.

In this chapter, the first section presents in detail the computation method of the second-order work from micromechanic variables. After that, this approach is extended to the mesoscale (grain-loops *L-3* and *L-6* in particular). Then a comparison between the second-order work within *L-3* and *L-6* is carried out as an attempt to explore the instability of grain-loops. The final part studies the

magnitude concentration of the microscopic second-order work around the buckled force-chains as an attempt to elucidate the relation between the vanishing of the second-order work and the instability of force-chains.

5.2 Linking macroscopic and microscopic scales

The second-order work can be expressed in a Lagrangian formalism as:

$$W_2 = \int_{V_0} \delta\Pi_{ij}\delta F_{ij} dV_0 \tag{5.1}$$

or in an Eulerian formalism:

$$W_2 = \int_{V} \delta\sigma_{ij}\delta\varepsilon_{ij} dV \tag{5.2}$$

where $\mathbf{\Pi}$ is the first Piola-Kirchoff stress tensor, $\boldsymbol{F}$ is the displacement gradient tensor, $\boldsymbol{\sigma}$ is the Cauchy stress tensor and $\boldsymbol{\varepsilon}$ is the strain tensor. V is the current volume of the system and V_0 is the initial volume of the system. The reference coordination is demonstrated in Figure 5.1.

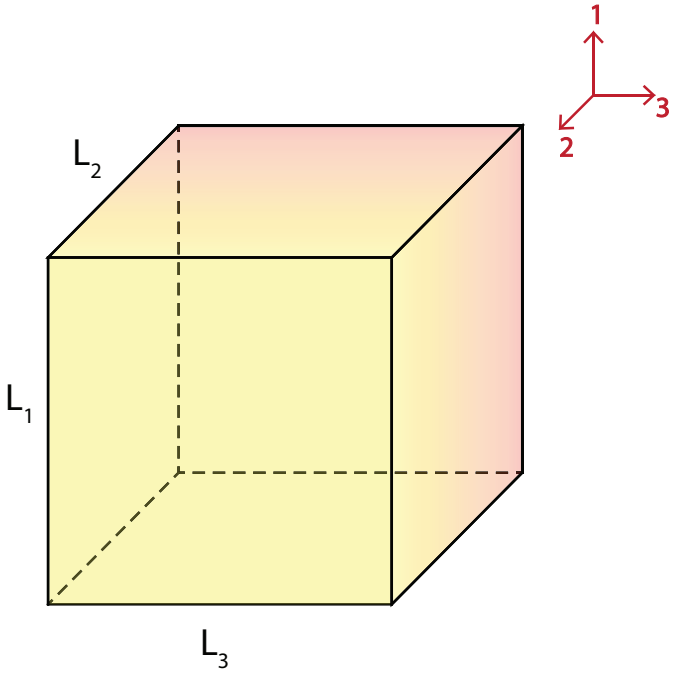

FIGURE 5.1: *Cubic specimen - geometrical settings*

Let us consider a homogeneous material comprising of N grains randomly located. 'p' denotes indiscriminately the grain (as a body) or enumerates a particular grain within the assembly such that $1 \leq p \leq N$. At a given moment t, each grain has contacts with n_p neighbour particles $q \neq p$ (Figure 5.2), whereas the total number of contacts in the assembly at this moment is denoted N_c. Particles having contacts with boundaries ∂V are distinguished with internal particles occupying the volume $\breve{V} = V - \partial V$ which are strictly separated from the boundaries.

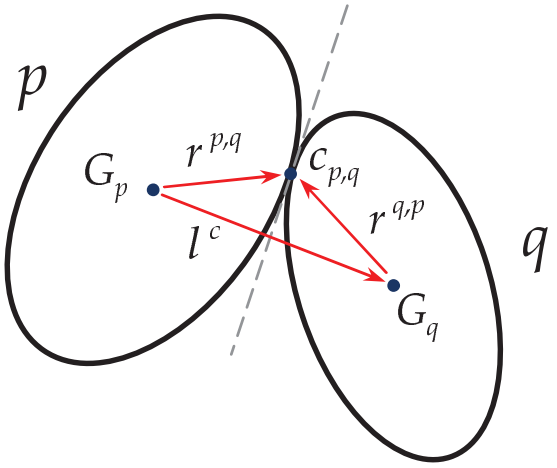

FIGURE 5.2: *Definition of particles in contact (Nicot et al. [2012a])*

It is shown that (Nicot et al. [2012a]) the second-order work can be written as a function of microscopic variables describing the granular material microstructure:

$$W_2 = \sum_{p,q} \delta f_i^c \delta l_i^c + \sum_{p \in V} \delta f_i^p \delta x_i^p \tag{5.3}$$

where $\boldsymbol{l}_c$ is the branch vector connecting the two centers of a contacting pair of particles in contact (p, q), $\boldsymbol{f}_c$ is the inter-particulate contact force, $\boldsymbol{f}^p$ is the resultant contact force applying on the particle p and x^p denotes the position of the mass center of p.

Equation 5.3 is the combination of two terms:

- The first term $\sum_{p,q} \delta f_i^c \delta l_i^c$ implies the contact force and the branch vector between the particles in contact. This term can be linked to the microscopic second-order work $W_2^m = \delta f_i^c \delta u_i^c$ of the given contact c between 2 particles

p and q (Figure 5.2). $\boldsymbol{u}^c$ is the relative displacement of the particle p to the particle q. As:

$$\delta\boldsymbol{u}^c = \delta\boldsymbol{u}^p - \delta\boldsymbol{u}^q + \boldsymbol{r}^{p,q} \wedge \delta\boldsymbol{\omega}^q - \boldsymbol{r}^{p,q} \wedge \delta\boldsymbol{\omega}^p = \delta\boldsymbol{l}^c + \boldsymbol{r}^{q,p} \wedge \delta\boldsymbol{\omega}^q - \boldsymbol{r}^{p,q} \wedge \delta\boldsymbol{\omega}^p \quad (5.4)$$

we have:

$$\delta\boldsymbol{f}^c.\delta\boldsymbol{u}^c = \delta\boldsymbol{f}^c.\delta\boldsymbol{l}^c - (\boldsymbol{r}^{q,p} \wedge \delta\boldsymbol{f}^{p,q}).\delta\boldsymbol{\omega}^q - (\boldsymbol{r}^{p,q} \wedge \delta\boldsymbol{f}^{q,p}).\delta\boldsymbol{\omega}^p \quad (5.5)$$

which implies that:

$$W_2^m = \sum_{p,q} \delta f_i^c \delta l_i^c - \sum_{p,q} ((\boldsymbol{r}^{q,p} \wedge \delta\boldsymbol{f}^{p,q}).\delta\boldsymbol{\omega}^q + (\boldsymbol{r}^{p,q} \wedge \delta\boldsymbol{f}^{q,p}).\delta\boldsymbol{\omega}^p) \quad (5.6)$$

With the absence of the rotation of particles, the microscopic second-order work is reduced to $\delta f_i^c \delta l_i^c$. In this case, we have:

$$W_2^m = W_2 - \sum_{p \in V} \delta f_i^p \delta x_i^p \quad (5.7)$$

- The second term $\sum_{p \in V} \delta f_i^p \delta x_i^p$ implies the incremental resultant force $\delta\boldsymbol{f}^p$ acting on each particle p. Whether the inertial effect is negligible (in the quasistatic regime, for example), the contribution of this term is not significant. However, when the micro-structural rearrangement happens more importantly and more rapidly, this term is no longer neglected.

Equation 5.3 introduces the micro-mechanical expression of the second-order work, which allows us to investigate, on the microscopic scale, the origin of the vanishing of macroscopic second-order work. The vanishing of the second-order work is fundamental and necessary for the collapse of the system to occur (Darve et al. [2004], Nicot et al. [2009]).

5.3 Numerical validation of the second-order work at the contact scale: the 3D case

It is necessary to validate the expression of second-order work computed from the microscopic variables. The numerical simulation in this section is carried out by modeling a stress probe test (Alonso-Marroquin and Herrmann [2005], Bardet [1994], Gudehus [1979], Nova [1994]) in quasi-static regime, applying on a 3D sample introduced in Chapter 3. Since the test is in quasistatic regime, the term $\sum_{p\in V} \delta f_i^p \delta x_i^p$ is negligible, therefore equation 5.3 can be reduced to:

$$W_2 = \sum_{p,q} \delta f_i^c \delta l_i^c \tag{5.8}$$

It is worth noting that when a simulation implies a significant rearrangement of the particles that leads to an irreversible deformation (inter-particulate sliding between particles, opening or creation of contacts), the term $\sum_{p\in V} \delta f_i^p \delta x_i^p$ cannot be neglected and must be taken into account for the computation of the second-order work.

The comparison between the second-order work calculated from macroscopic variables and from microscopic variables is the subject in hand. This comparison allows us to check the validity of equation 5.8. The process is explained in next section (Hadda et al. [2013], Sibille [2006a]). After that the result of the comparison is demonstrated.

5.3.1 Stress probe and strain probe simulation

In this study, only axisymmetric (stress or strain) conditions are considered. Therefore, the stress (or strain) loading can be demonstrated on an axisymmetric plane (Gudehus [1979]). Figure 5.3 demonstrates the definition of the loading on the left and the response of the sample on the right.

Firstly, we defined the stress increment $\Delta\boldsymbol{\sigma}$ in the incremental stress space $(\sqrt{2}\Delta\sigma_3, \Delta\sigma_1)$, the norm of which is $\|\Delta\boldsymbol{\sigma}\| = \sqrt{(\Delta\sigma_1)^2 + 2(\Delta\sigma_3)^2}$. The response of the sample is given by $\Delta\boldsymbol{\varepsilon}$. For the case of strain probe, the strain increment in the axisymmetric strain space $(\sqrt{2}\Delta\varepsilon_3, \Delta\varepsilon_1)$ is imposed with $\|\Delta\boldsymbol{\varepsilon}\| = \sqrt{(\Delta\varepsilon_1)^2 + 2(\Delta\varepsilon_3)^2}$ and

the response of the system is $\Delta\sigma$. The angle between the abscissa axis and the incremental stress or strain loading direction is denoted α_σ (or α_ε).

Secondly, once the incremental stress (or strain) is defined, it is applied to a specimen at a given stress-strain state. By doing so, the system gives a correspondent response to the loading as an incremental strain (or stress), this response is demonstrated on the right side in the Figure 5.3, with the value $\|\Delta\boldsymbol{\varepsilon}\| = \sqrt{(\Delta\varepsilon_1)^2 + 2(\Delta\varepsilon_3)^2}$ (or $\|\Delta\boldsymbol{\sigma}\| = \sqrt{(\Delta\sigma_1)^2 + 2(\Delta\sigma_3)^2}$) and the angle β_σ (or β_ε) between the abscissa axis and the incremental response vector.

The stress probe (or strain probe) simulation is carried out by applying the same loading condition at a given stress-strain state of the sample (which can be saved and reloaded again by the help of numerical tool). The loading condition varies by changing the loading angle (α_σ or α_ε) from 0° to 360°.

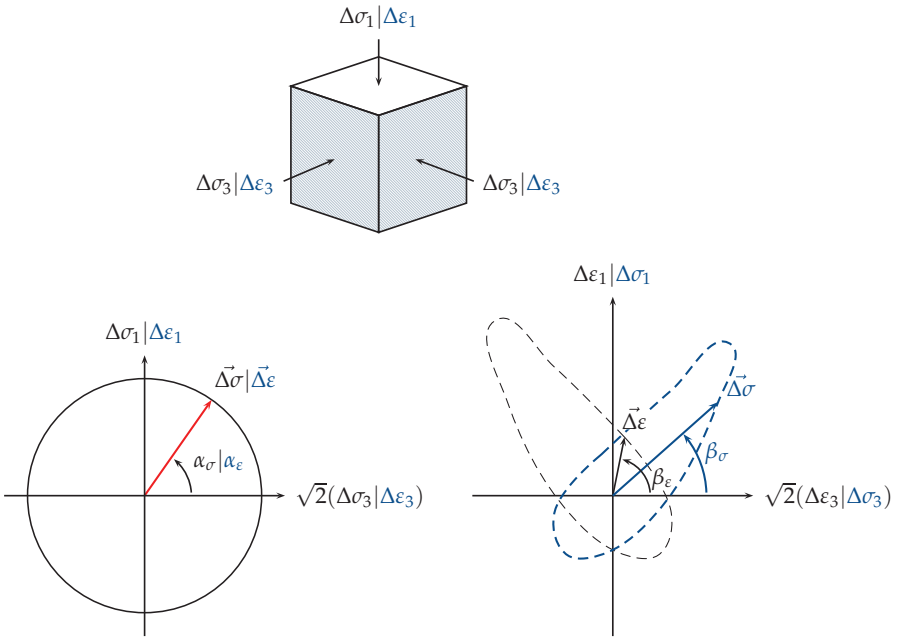

FIGURE 5.3: *Definition of the Rendulic plan: stress probe and strain probe (left) and the response of the system (right) (Hadda et al. [2013])*

The initial state of the sample prepared for the stress probe test is obtained during a triaxial test.

In Figure 5.4 and Figure 5.5, a dense specimen is considered, and a drained biaxial test is applied with the confinement stress $\sigma_3 = 200kPa$. Three different states are indicated by the points A, B, C. Once the initial state is chosen, the sample is stabilized to reach a quasistatic state ($E_c < 10^{-7}J$, see Chapter 3), the probing

test is carried out by applying an incremental strain ($|\Delta\varepsilon| = 5 \times 10^{-4}$) to the specimen.

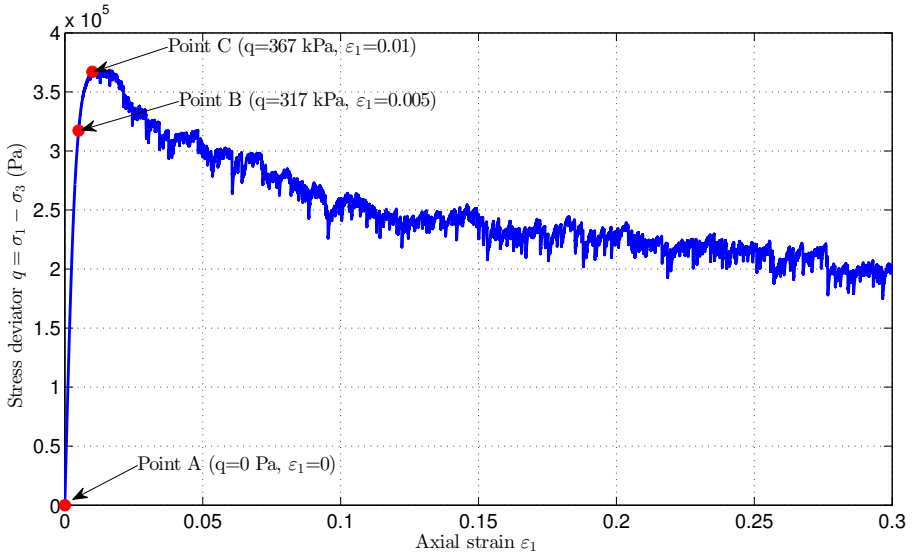

FIGURE 5.4: *Deviatoric stress versus axial strain and the 3 states where the probing test is carried out*

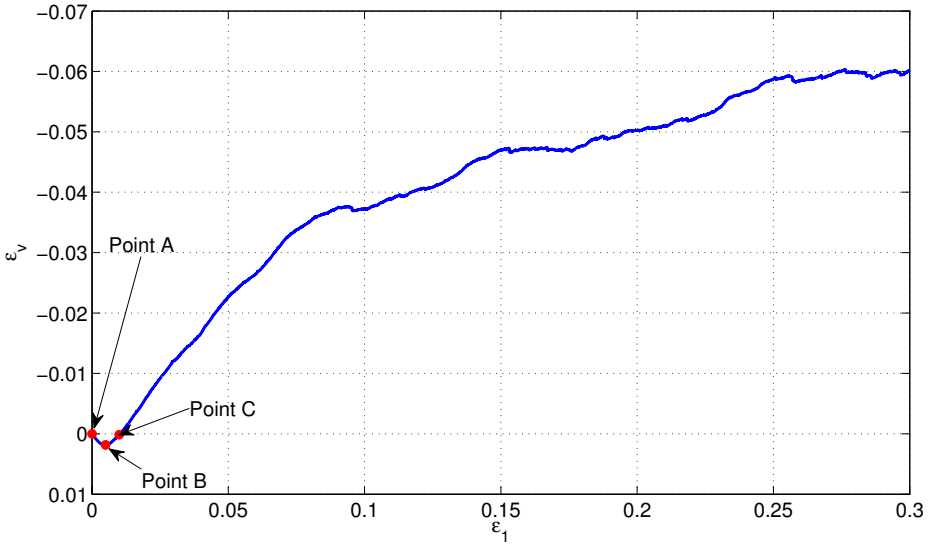

FIGURE 5.5: *Volumetric strain versus axial strain and the 3 states where the probing test is carried out*

5.3.2 Vanishing of the second-order work and instability cones

Based on the stress probe (or strain probe) test mentioned above, for each direction of the stress probe (or strain probe), whenever the incremental strain response $\Delta\boldsymbol{\varepsilon}$ (or $\Delta\boldsymbol{\sigma}$) of the system is determined, the normalized second-order work can be defined as:

$$W_2^n = \frac{\Delta\boldsymbol{\varepsilon} \cdot \Delta\boldsymbol{\sigma}}{\|\Delta\boldsymbol{\varepsilon}\| \cdot \|\Delta\boldsymbol{\sigma}\|} \tag{5.9}$$

this is also the cosine of the angle between $\Delta\boldsymbol{\sigma}$ and $\Delta\boldsymbol{\varepsilon}$, consequently we have $-1 \leq W_2^n \leq 1$. For the sample mentioned in previous section, W_2^n is plotted in a polar diagram as demonstrated in Figure 5.6. It is worth noting that in this diagram, what we plot is $W_2^n + \rho$, where ρ is chosen so that the negative values of W_2^n are inside the circle of radius ρ (marked as red circle in the diagram).

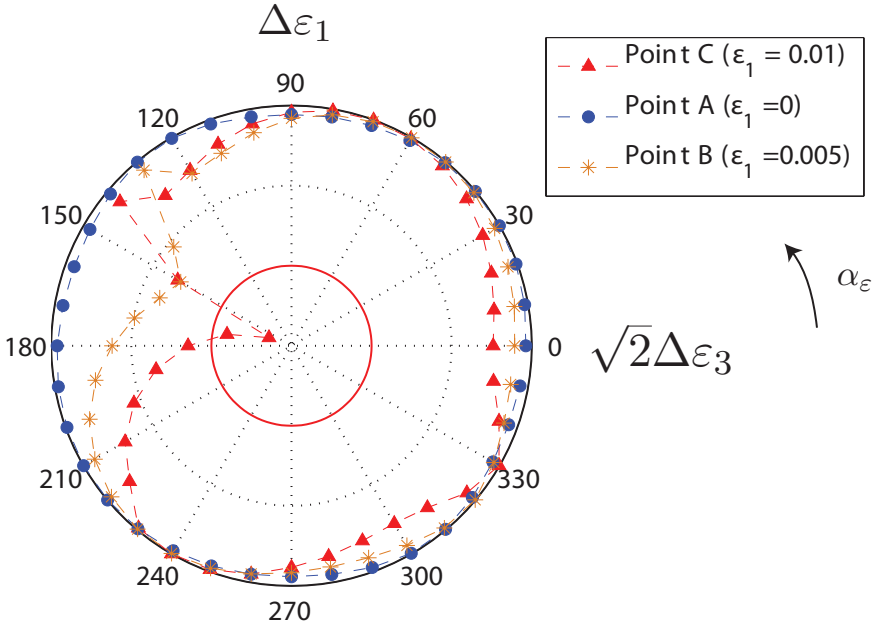

FIGURE 5.6: *The normalized second-order work from the strain probe test mentioned in Section 5.3.1*

5.3.3 Result of the numerical validation

The purpose of this section is to compare the *non-normalized* second-order work W_2 and the second-order work W_2^m calculated from the microscopic variables: contact forces and positions of particles. In order to determine W_2^m, the scalar product $\Delta \boldsymbol{f}^c \cdot \Delta \boldsymbol{l}^c$ is evaluated at each contact point. The variation of the contact force $\Delta \boldsymbol{f}^c$ is the difference between the contact force at the final state and at the initial state of the test. The variation of the branch vector is calculated from the displacement of the particles involving the contact, after the application of the incremental loading, the incremental branch vector at the contact between particles p, q is defined as $\Delta \boldsymbol{l}^c = \Delta \boldsymbol{x}^p - \Delta \boldsymbol{x}^q$. For a given incremental loading direction, the value of the second-order work from the microscopic variables is calculated by summing all the scalar products for all the contacts inside the sample.

It is worth noting that during the probe test, newly created contacts and lost contacts are also taken into account for the computation of $\Delta \boldsymbol{f}^c \cdot \Delta \boldsymbol{l}^c$. For lost contacts, the contact force at the final state is considered nil; for newly created contacts, the contact force at the initial state is considered nil (Hadda et al. [2013]).

Figures 5.7, 5.8, 5.9 demonstrate the comparison between the second-order work calculated from the macroscopic variables W_2 (non-normalized) and from the microscopic variables W_2^m. A very good agreement is found between the two terms, which confirms the validity of the second-order work computed from microscopic variables. Other numerical simulations on looser samples can be found in Hadda et al. [2013].

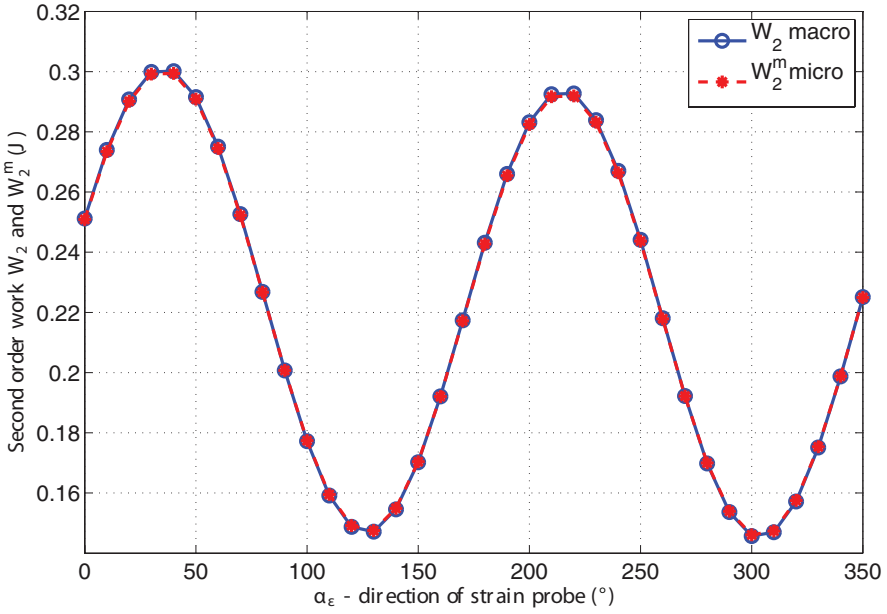

FIGURE 5.7: *Comparison between W_2 and W_2^m at point A*

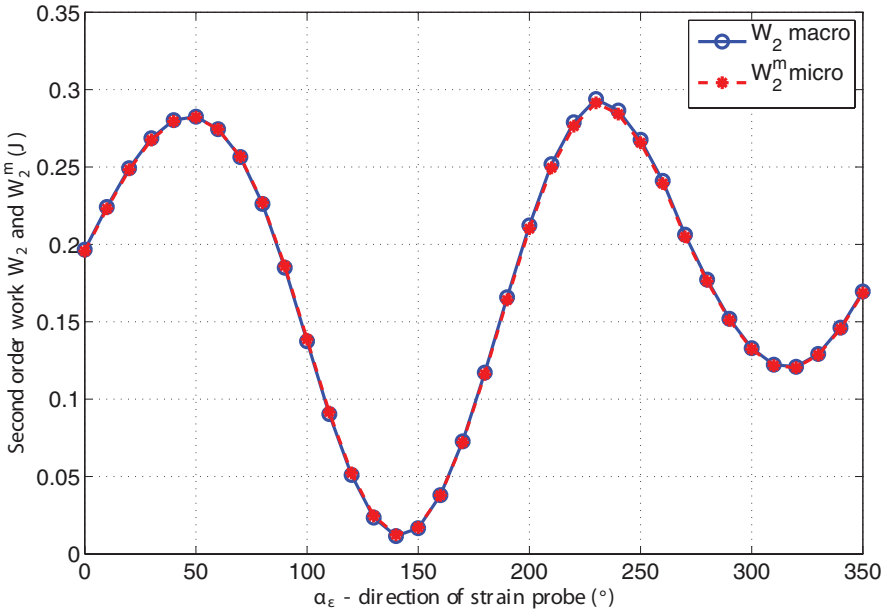

FIGURE 5.8: *Comparison between W_2 and W_2^m at point B*

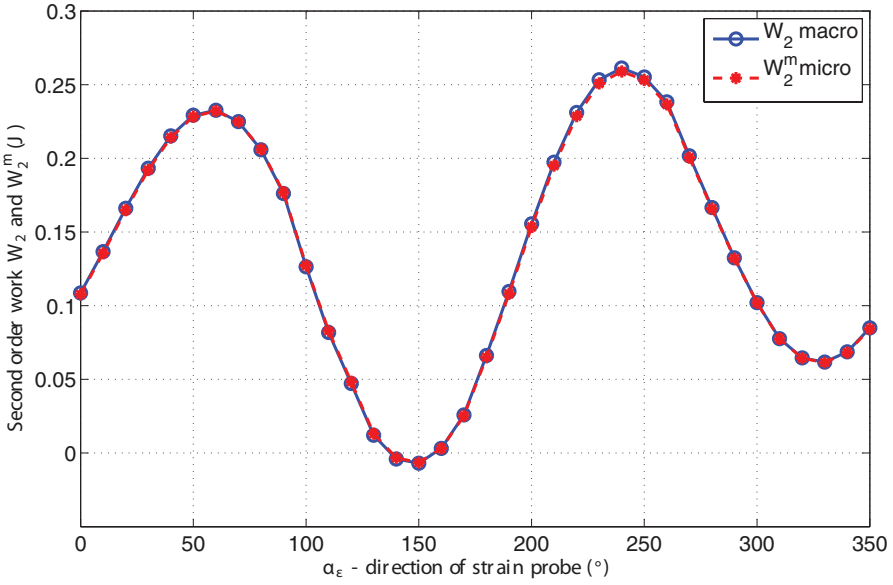

FIGURE 5.9: *Comparison between W_2 and W_2^m at point C*

5.4 Contact c^- and buckling of force-chains

Force-chains were shown to play an important role in the force transmission within the granular specimen, and therefore determine the strength of the specimen. The limit stress observed when the deviatoric (or axial) stress reaches a maximum means that the specimen is not able to increase its force bearing, that is to say to develop force-chains able to resist against an external loading larger than this maximum value. In this context, the stability of force-chains is an important point, since the collapse of force-chains can compromise the bearing capacity of the specimen itself.

In this section, we propose to investigate the collapse of force-chains in the context of the second-order work approach. In the previous section, an expression of the second-order work applying to the contact scale were inferred. This expression involves the incremental contact force, together with the incremental change in the branch vector joining the two centers of the grains in contact: $W_2^c = \Delta f_c \Delta l_c$.

When W_2^c is negative, the contact 'c' is considered as unstable, and is denoted 'c^-'. As a force-chain can be regarded as a set of contacts between the particles composing the pattern, it makes sense tracking the distribution of such 'c^-' contacts within the specimen, and checking whether these contacts belong to buckling

force-chains. If so, this would mean that the evolution of the mesostructure of the specimen, namely the force-chains, is correlated to the instability of the contacts within the chains.

Figure 5.13 shows the distribution of the contacts c^- within the 2D dense specimen (see Chapter 4) [1], along a drained biaxial loading path. Different states are presented ($\varepsilon = 0.1\%$, $\varepsilon = 2\%$, $\varepsilon = 6\%$) as indicated in Figure 5.10.

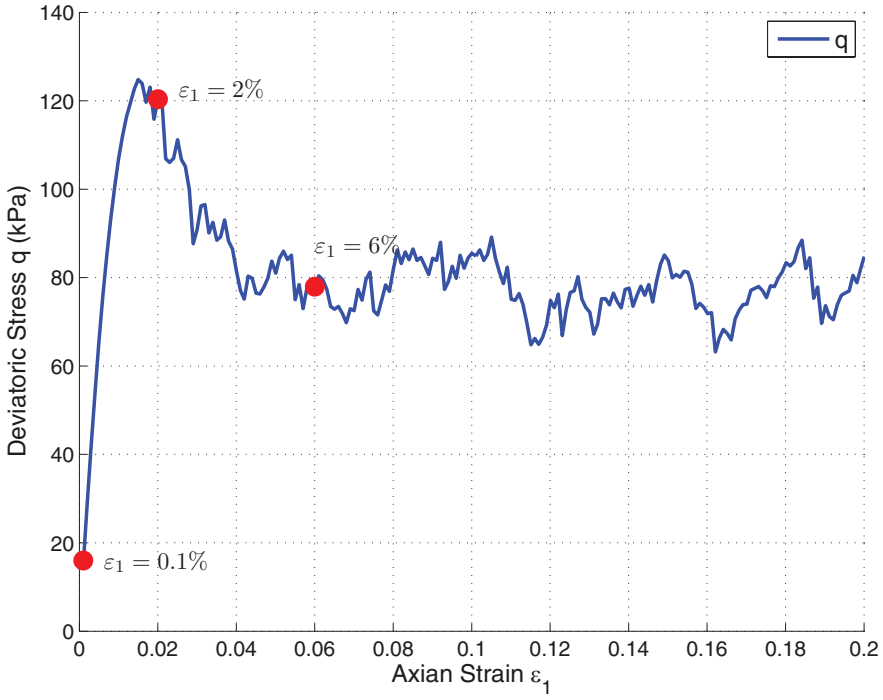

FIGURE 5.10: *Three considered states* $\varepsilon_1 = 0.1\%$, $\varepsilon_1 = 2\%$ *and* $\varepsilon_1 = 6\%$

Figures 5.11 and 5.12 give the distribution of the (incremental) kinematic field at the same strain states. It can be observed that the contacts c^- concentrate within the same zones as the incremental displacement field. At 6 % of axial strain (softening regime), the contacts c^- locate within two crossed bands, that coincide with the kinematic pattern (shear band) observed in Figures 5.11 and 5.12. Hence, this points out that the second-order work vanishes within the zones where the specimen fails.

Moreover, we examine also the distribution of the buckling grains. As introduced in Chapter 4 buckling grains belong to buckling force-chains. Only central grains (each force-chain is described (segmented) as a set of three-grain force-chain) are candidate to be buckling grains as reported in Figure 4.13. Interestingly, the

[1] For a complete plots of contacts c^-, see Section 5.7

distribution of the buckling grains (at $\varepsilon_1 = 2\%$ and $\varepsilon_1 = 6\%$) locates along a shear band, corresponding to the band observed in both Figures 5.11 and 5.12 (Figures 5.11 and 5.12 display the relative displacement field on the horizontal x-axis ΔU_x and the vertical y-axis ΔU_y at three corresponding states of axial strain ε_1: 0.1%, 2% and 6%, respectively).

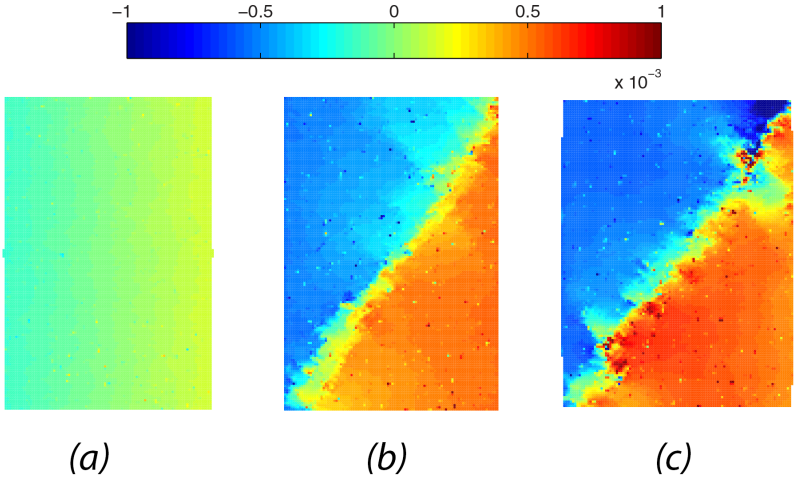

FIGURE 5.11: *Relative displacement field* ΔU_x *at (a):* $\varepsilon_1 = 0.1\%$*, (b):* $\varepsilon_1 = 2\%$ *and (c):* $\varepsilon_1 = 6\%$

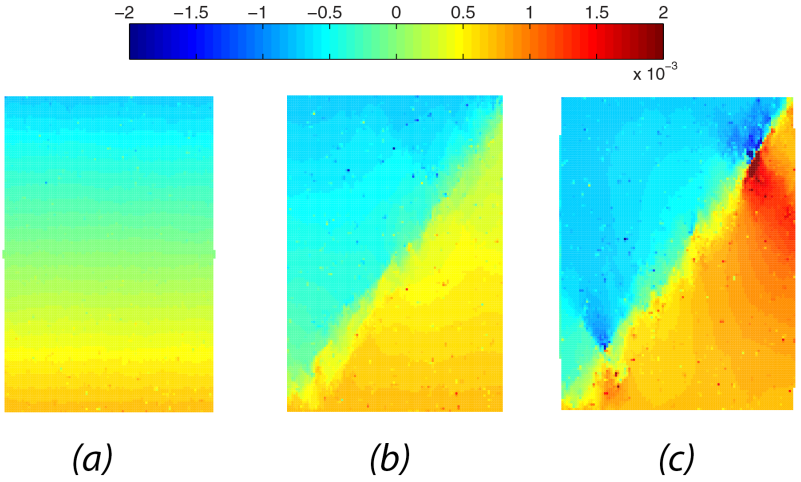

FIGURE 5.12: *Relative displacement field* ΔU_y *at (a):* $\varepsilon_1 = 0.1\%$*, (b):* $\varepsilon_1 = 2\%$ *and (c):* $\varepsilon_1 = 6\%$

As a consequence, both contacts c^- and buckling force chains distribute accordingly the failure pattern of the specimen: when a shear band develops within the specimen, the distributions of both the buckling of force-chains and the contacts c^- coincide with the shear band pattern.

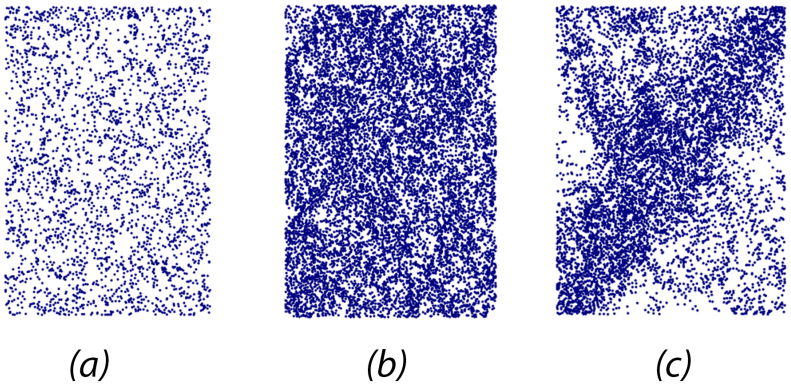

FIGURE 5.13: *Distribution of contacts c^- at (a): $\varepsilon_1 = 0.1\%$, (b): $\varepsilon_1 = 2\%$ and (c): $\varepsilon_1 = 6\%$*

As defined in previous chapter, the force-chain collapses when the buckling phenomenon occurs, this phenomenon is caused by the rearrangement of particles inside the force-chain. It is observed that when the specimen collapsed, there are more buckled force-chains inside the shear band. In Figure 5.14, plots of buckled force-chains at three similar states as in Figure 5.13 are demonstrated; and in Figure 5.15, only buckling grains are plotted.

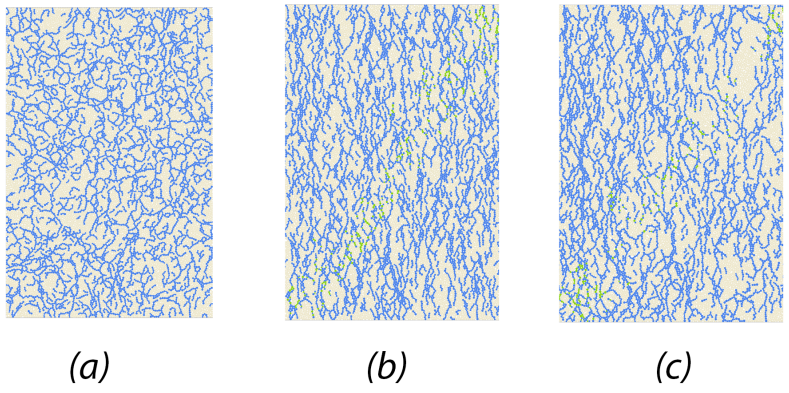

FIGURE 5.14: *Distribution of force-chains at (a): $\varepsilon_1 = 0.1\%$, (b): $\varepsilon_1 = 2\%$ and (c): $\varepsilon_1 = 6\%$*

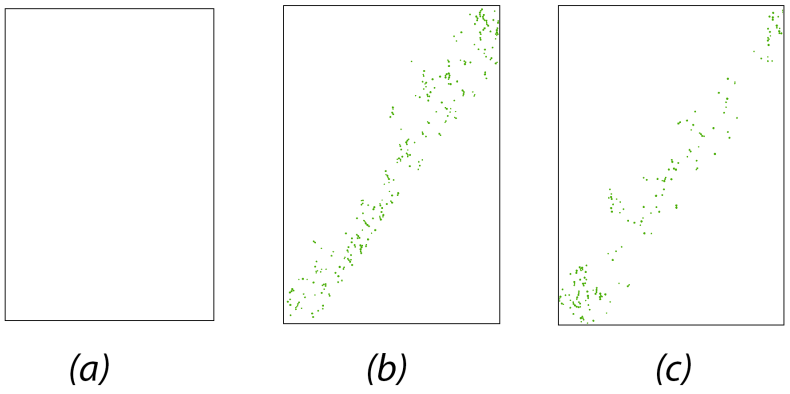

FIGURE 5.15: *Distribution of buckling grains at (a): $\varepsilon_1 = 0.1\%$, (b): $\varepsilon_1 = 2\%$ and (c): $\varepsilon_1 = 6\%$*

Both contacts c^- and buckled force-chains distribute accordingly to the failure of the sample: when a shear band appears within the specimen, the buckling of force-chains and the distribution of contacts c^- have similar patterns as the development of the shear band.

The purpose of the next investigation is to find the relation between the buckling of force-chains and the distribution of the contacts c^-. Figure 5.16 demonstrates a close view of the distribution of contacts c^- and the buckling grains of force-chains at the axial deformation $\varepsilon_1 = 2\%$.

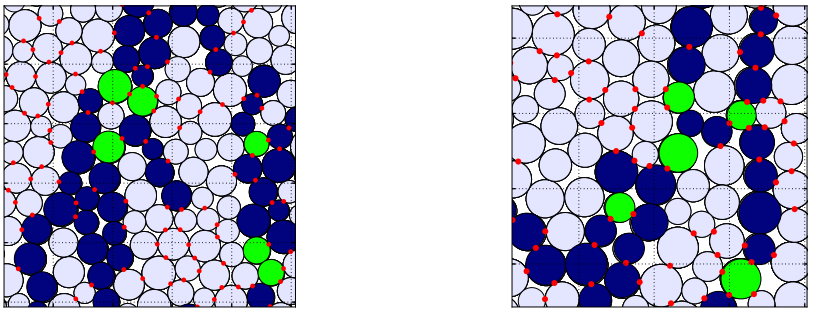

FIGURE 5.16: *Zoom to the sample. Red dots demonstrate contacts c^-, green particles are buckling grains, dark blue grains are particles belonging to force-chains*

According to Figure 5.16, whether the force-chain is buckled, the contact c^- appears at that buckling point, but the appearance of the contact c^- is not a sufficient condition (it is mandatory, since each buckling grain admits at least one contact

c^-) for the buckling of force-chains to occur, by the fact that a number of contacts c^- is also found at elsewhere inside the sample.

The result leaves an unanswered question: the instability of force-chains and the distribution of the vanishing of the microscopic second-order work are not strongly connected, as contacts c^- also appear in the non-force-chain zone, and also at the grain inside the force-chain that is not a buckled grain; so, how about the magnitude of the contact c^- around the buckling grain? What is its property? To answer this question, an investigation is carried out using a method explained in the paragraph below.

Let us consider a buckling grain inside a buckled force-chain. From this grain, an incremental scanning region can be defined. Then by taking into account all the contacts c^- inside the scanning zone by computing the density D_{c^-} of the microscopic second-order work, it follows:

$$D_{c^-} = |\frac{\sum W_2^c}{A_s}| \tag{5.10}$$

where $\sum W_2^c$ is the sum of the magnitude of the second-order work at all contacts c^- in the scanning zone, and A_s is the area of the scanning zone. Two types of scanning are considered: the first method is the circle scan, the second is the ring scan. These methods of scanning are defined in Figure 5.17. By taking the buckling grain at the center of the scanning zone, the zone is then defined by an increment of the average of grains radii $\overline{r}$. The only difference between the two methods is: for the circle scan, the scanning zone is continuous, whereas for the ring scan, the scanning zone is divided into successive rings of radius $i\overline{r}$, i being integer.

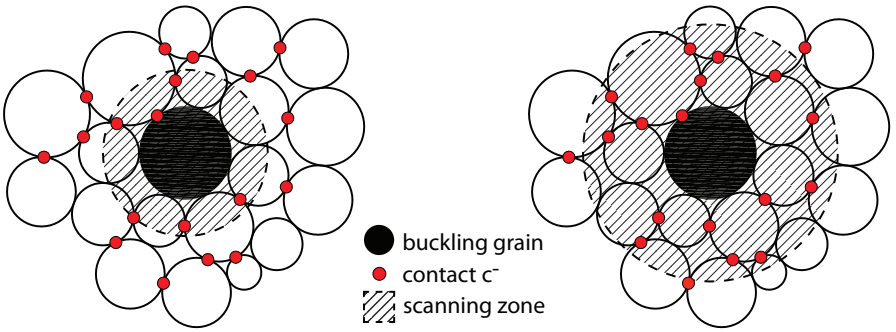

(a) First method: Circle scan

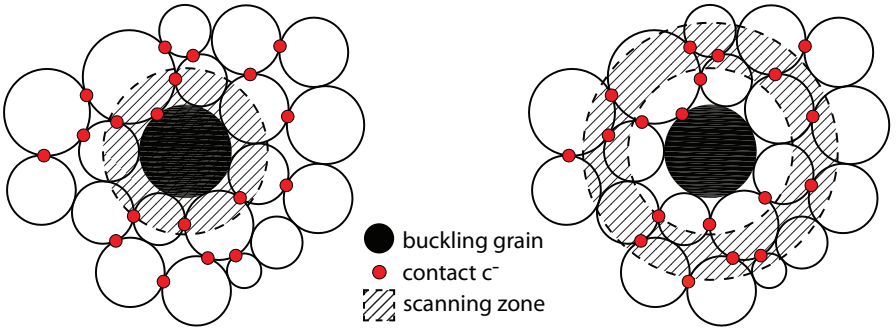

(b) Second method: Ring scan

FIGURE 5.17: *Definition of the scanning zone around the buckling grain*

The result is shown in Figure 5.18. As can be seen in the diagram, the magnitude of contacts c^- near the buckling grain is greater than in the outside zone. They have greater amplitude around the buckling grains. Then when the scanning zone is larger (the scanning iteration i increases) and getting further from the buckling grain (the center of the scanning zone), we observe a decreasing trend.

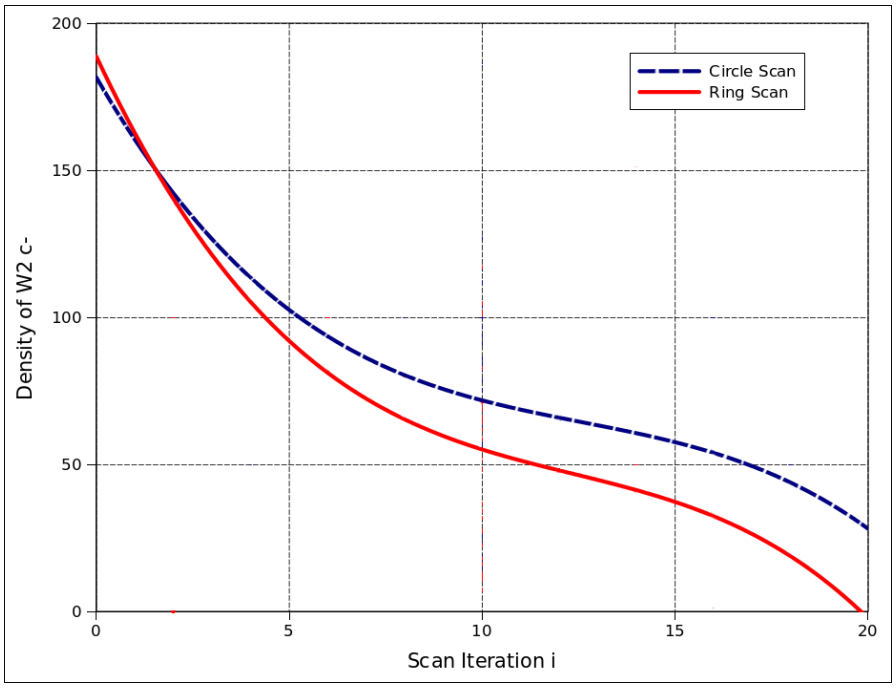

FIGURE 5.18: *Average magnitude of the vanishing second-order work around the buckling grains*

This result indicates that the environment surrounding the buckling grains is unstable in comparison with other zone within the specimen. Although the vanishing of the second-order work at the contact scale does not imply the collapse of force-chains, their magnitude density changes accordingly to the distribution of buckling grains. This difference in magnitudes of the second-order work can be explained by the fact that the collapse of force-chains induces a great variation of the increment of contact forces $\Delta \boldsymbol{f}$; consequently, $|\Delta \boldsymbol{f} \cdot \Delta \boldsymbol{l}|$ increases near the buckled force-chains.

5.5 Microscopic second-order work and instability of attached grain-loops

In Chapter 4 we have discussed the relation between the attached grain-loops and the lifespan of force-chain and reached the conclusion that the force-chain is more stable if it is supported by stronger grain-loops. From the geometry point of view, the grain-loop which has lesser particles (*L-3*) tends to be more stable than the grain loop which has greater particles (*L-6*). In the section, we use the microscopic second order work to confirm this statement.

The grain-loop is a set of particles which have contacts with each other, forming a close polygonal line. The breakage of a grain-loop occurs when one of these contacts is lost, the grain-loop is therefore no longer available. Based on this definition of the grain-loop, the microscopic second-order work of a grain-loop is introduced as the sum of the scalar product of the incremental contact force and the incremental branch vector of every contact inside a grain-loop. For example, Figure 5.19 demonstrates the grain-loop of 3 particles (*L-3*), this grain-loop can be decomposed into 3 contacts.

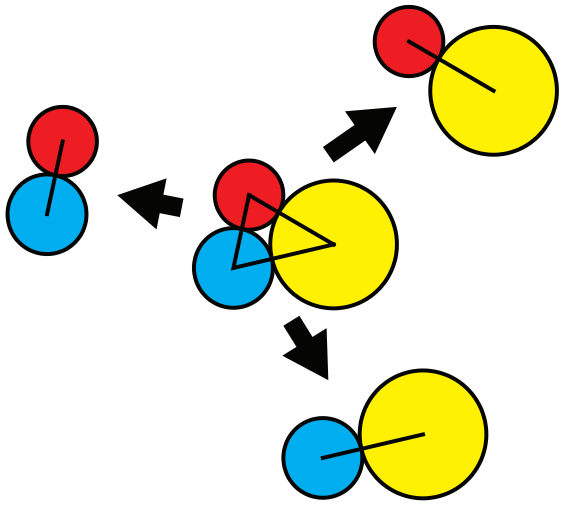

FIGURE 5.19: *Decompostion of a grain-loop L-3 into 3 contacts*

The second-order work of this single grain-loop therefore reads:

$$W_2^{L-3(c)} = \sum_{i=1}^{3} \Delta f_i^c \cdot \Delta l_i^c \tag{5.11}$$

similarly, for *L-6*, we have:

$$W_2^{L-6(c)} = \sum_{i=1}^{6} \Delta f_i^c \cdot \Delta l_i^c \tag{5.12}$$

Based on this definition, the second-order work for each grain-loop can be calculated. Then by summing all of them together, we can define the global second-order work (W_2^{L-3} and W_2^{L-6}) for grain-loops *L-3* and *L-6*.

In what follows, the second-order works for grain-loops *L-3* and *L-6* are compared; after that, the surrounding environment of force-chains is taken into account: the

second-order works for the attached grain-loops (grain-loops that share contact with force-chains) *L-3a* and *L-6a* are compared.

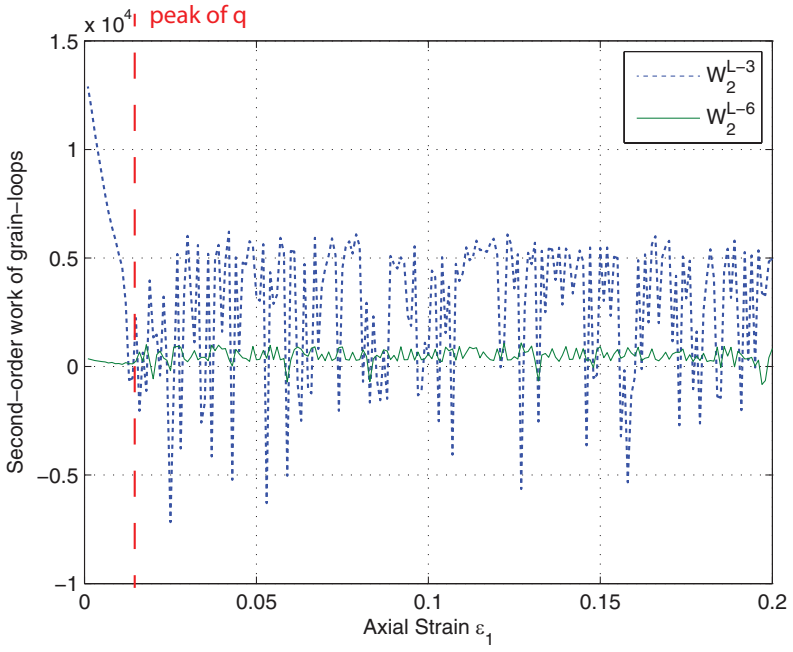

FIGURE 5.20: *Comparison between the second-order work for loop L-3 and L-6 in the biaxial test*

As can be seen in Figure 5.20, at the beginning of the test, the average second-order work for grain-loop *L-3* is greater than that for *L-6*. Then, before the peak of the deviatoric stress curve – or similarly when the axial strain $\varepsilon_1 < 1.5\%$, W_2^{L-3} is positive, but decreases rapidly; when the sample is no longer stable (after the peak of q), W_2^{L-3} begins to vanish. W_2^{L-6} is small, as an easy-to-deform structure, its second-order work is likely easier to vanish. It is worth noting that when all the grain-loops are taken into account, it means that not only grain-loops attaching to force-chains are taken into account, but also free grain-loops (grain-loops inside the sample but without contact with force-chains). In order to elucidate the relation between force-chains and grain-loops, attached grain-loops are taken into account.

The comparison of the second-order work (non normalized) between attached grain-loops *L-3* and attached grain-loops *L-6* is shown in Figure 5.21.

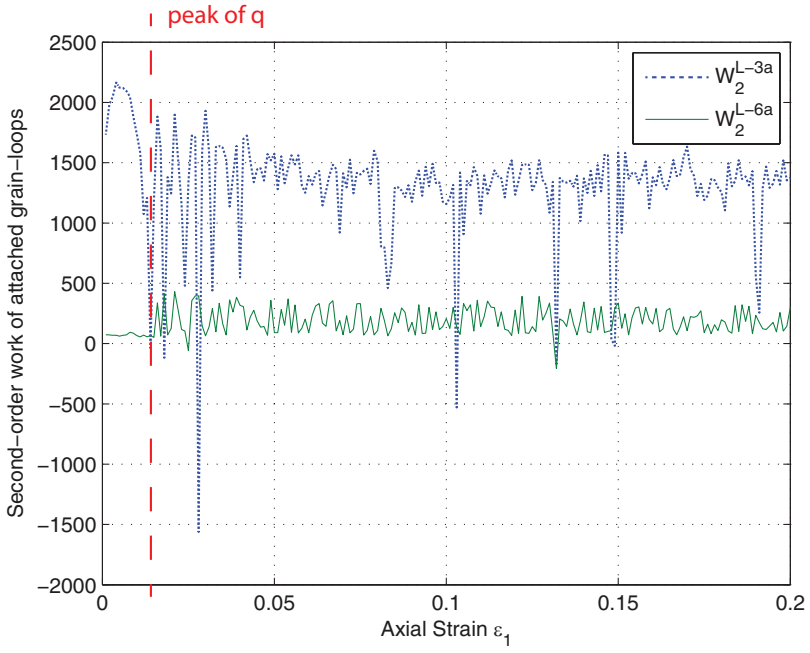

FIGURE 5.21: *Comparison between the second-order work for attached loop L-3a and L-6a in biaxial test*

The figure indicates that during the biaxial test, the overall second-order work for attached *L-3a* has a greater value than for attached *L-6a*. The grain-loops *L-6a* therefore tend to vanish more easily than the grain-loop *L-3a* do. The grain-loop *L-6a* is therefore less stable.

Moreover, during the hardening phase (the axial strain $\varepsilon_1 < 1.5\%$) of the biaxial test, the second-order work of *L-3a* increases gradually, while the *L-6a* shows no significant signal. But as soon as the sample is unstable, W_2^{L-3a} drops rapidly, and W_2^{L-6a} begins to fluctuate. As mentioned in Chapter 4, the instability of force-chains quantitatively relates to the surrounding environment where attached grain-loops are the main ingredient; by using the second-order work, the attached grain-loop *L-3a* is proven to be stronger than *L-6a*. When force-chains are supported by this type of mesostructure, force-chains are more stable. Also, *L-3* can be considered as an important element to ensure the stability of the specimen and on the contrary, when *L-6* appears, the specimen becomes more unstable. The variation of the second-order work of these two types of grain-loops illustrates very well this situation.

5.6 Conclusion

In this chapter, the second-order work calculated from microscopic variables is taken into account within a dense specimen subjected to a drained biaxial test. The distribution of the vanishing of second-order work (contact c^-), the second-order work for grain-loops and the concentration of contacts c^- around buckling force-chains are investigated.

At failure, the vanishing of the second-order work and the buckling of force-chain correlate with the forming of the shear band within the specimen. This relation is strengthened by the fact that around the buckled grains of force-chains, contacts c^- concentrate around these points. *When a force-chain buckles, the second-order work calculated from the microscopic variable vanishes at the buckling grain. However the appearance of the contacts c^- is not a sufficient indication to predict the buckling of force-chains.*

Moreover, when the second-order work is taken into account for grain-loops, it is proven that for a more unstable grain-loop, the evolution of its second-order work goes down closer to zero than the stable one.

5.7 Appendices

Figure 5.22 demonstrates all plots of the distribution of contact c^- during the test.

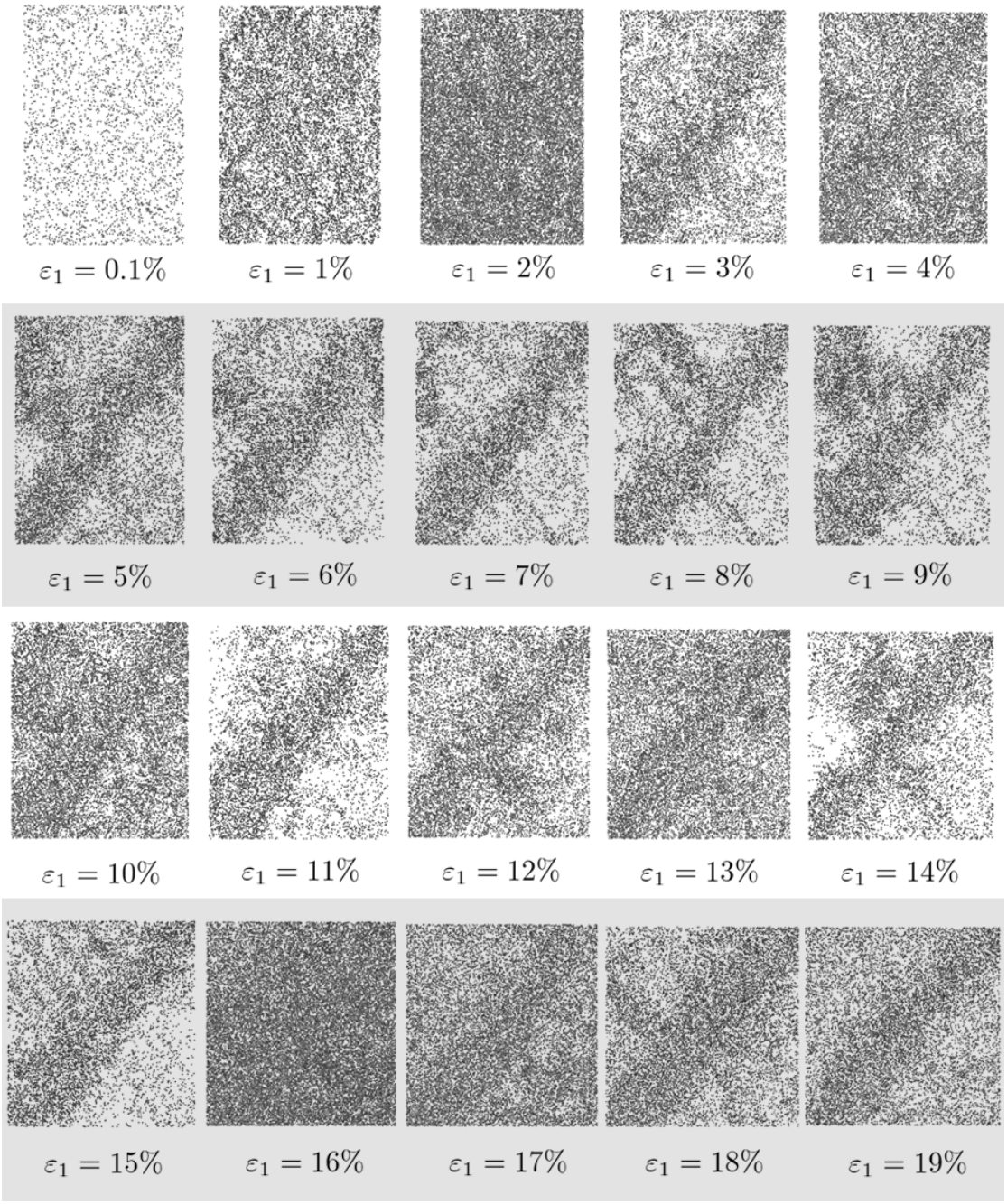

FIGURE 5.22: *Summary of the distribution of contacts c^- in the drained biaxial test of the dense specimen*

Figure 5.23 demonstrates all plots of the distribution of force-chains during the test. Only grains belonging to force-chains are plotted.

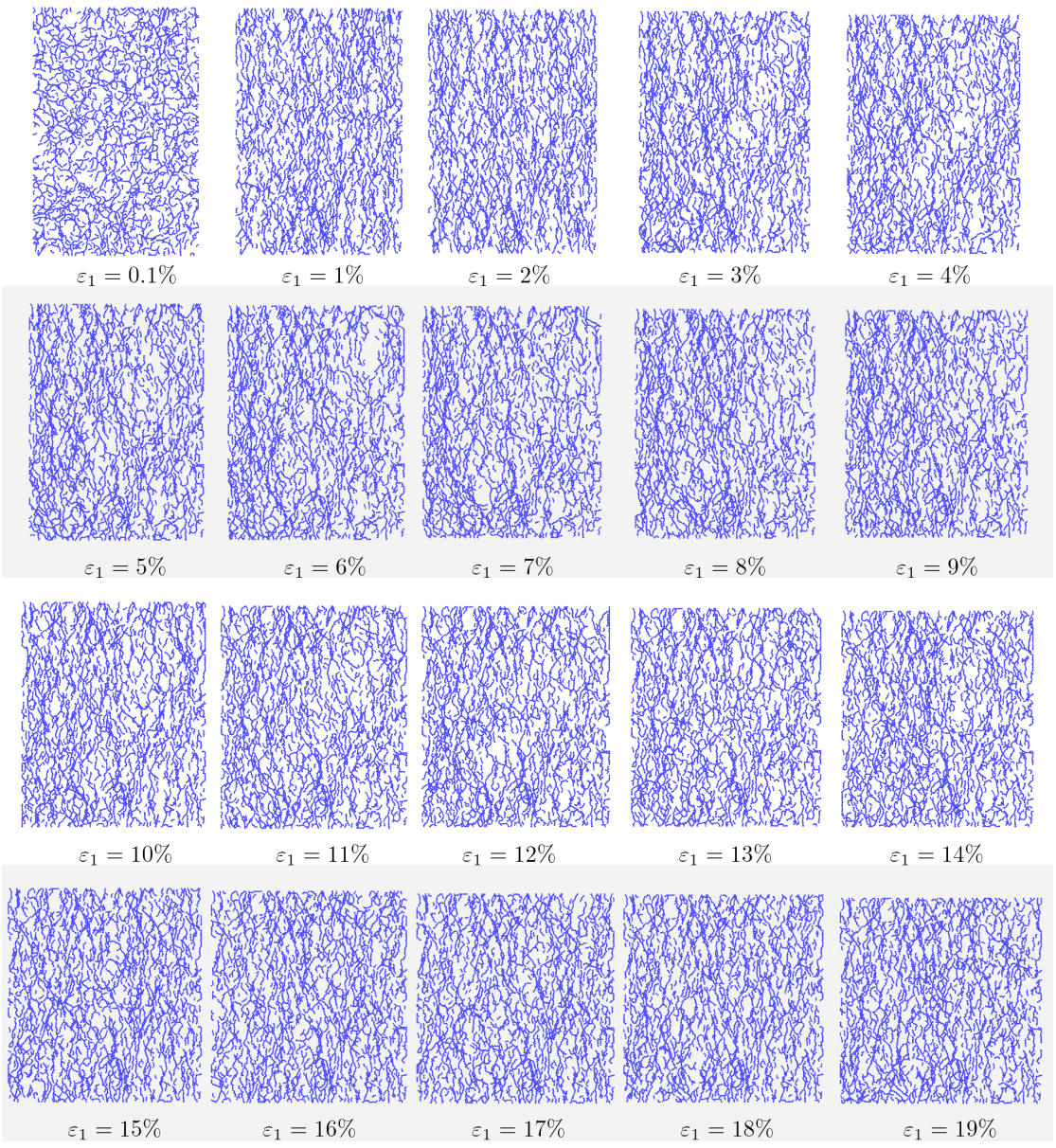

FIGURE 5.23: *Summary of the distribution of force-chains in the drained biaxial test of the dense specimen*

Figure 5.24 demonstrates all plots of the distribution of buckling grains during the test. Only buckling grains are plotted.

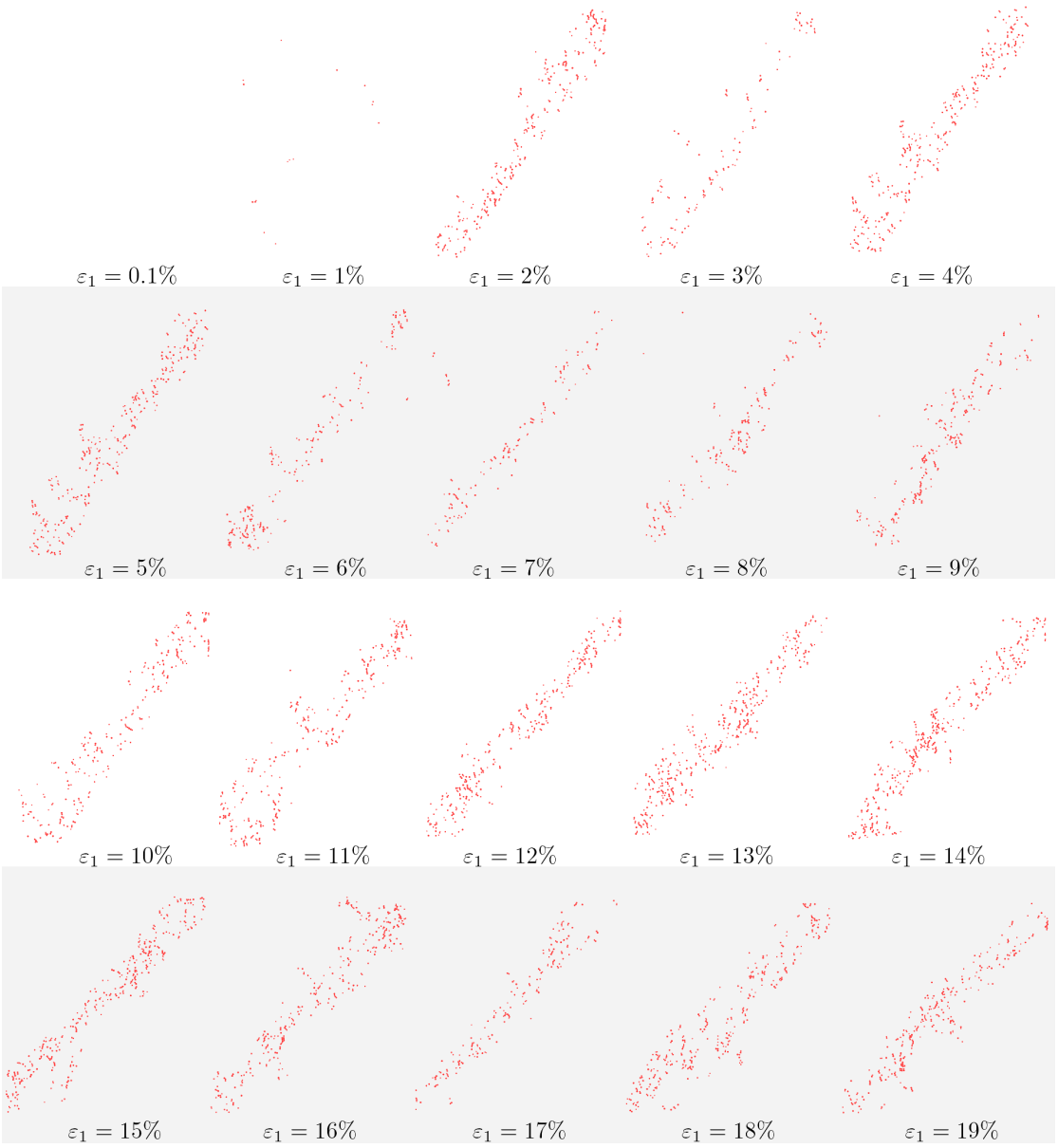

FIGURE 5.24: *Summary of the distribution of buckling grains in the drained biaxial test of the dense specimen*

Chapter 6

Conclusions and perspectives

This thesis pertains to the role of microstructures in granular materials. Multiscale numerical investigations were carried out on both macroscopic and microscopic scales using a DEM approach. The samples considered in this thesis are 3D and 2D specimens, consisting of spherical particles, surrounded by frictionless walls at the boundary.

Three main topics are discussed:

- Validation of the relation between the variation of kinetic energy with the second-order work for rate-independent systems, when the failure occurs, the specimen turing from a quasi-static regime to a dynamic regime.
- Investigation of the behaviour of mesostructures inside a 2D specimen, comprising of the force-chains and the grain-loops in a dense sample subjected to a drained biaxial test. Two main ideas are considered: **(a)** the relation between the evolution of force-chains number, the buckling of force-chains and the macroscopic behaviour (the deviatoric stress and the volumetric strain); **(b)** the relation between grain-loops and force-chains and which effect the grain-loops attached to force-chains give on the instability of those force-chains during their lifespan.
- Analyses of the microscopic second-order work on the contact scale and then expand it to grain-loops to investigate their instability. After that, a link between the buckling of force-chains and the distribution of microscopic second-order work is investigated, to analyze the physics of force-chains collapse.

Main results of this study are resumed below:

- For a rate-independent granular material, the diffuse failure can be accompanied by an outburst of kinetic energy. This increase in kinetic energy is caused by the difference between the external second-order work involving the external loading parameters and the internal second-order work. The mechanical origin lies in the distinction between the internal stress within the material and the applied stresses on the system's boundary. When the internal stress loses the capacity to balance the external stress, the specimen produces a dynamic response.

  Based on discrete elements simulations, the validity of the basic equation which relates the specimen's kinetic energy to the difference between external and internal second-order works, was checked carefully, using two different approaches: first, an integral method and second, a time expansion series. For this purpose, we have considered two numerical specimens. A dense specimen was subjected to a drained triaxial loading path, and a loose specimen was subjected to an undrained triaxial loading path. An increase in kinetic energy was observed after a limit state was reached (axial or deviatoric stress peak), after application of a small additional axial load. A very good agreement was found with the integral method, whereas the method based on expansion series requires a small time range. It is obvious that for very large strains, corresponding to a substantial collapse of the specimen, the validity of the equation can no longer be tracked.

- Force-chains and grain-loops were investigated from a biaxial drained test applied on a 2D, dense specimen. Involving force-chains and grain-loops, the macroscopic behaviour of the sample is poven to have a close correlation with the evolution of mesostructures.

  1. First, the evolution of force-chains and grain-loops changes in accordance with the macroscopic behavior. Force-chains are responsible for the strength of the granular material: the strength of granular system increases/decreases due to the establishment/disappearance of the strong force network (a.k.a. force-chains). Force-chain is the main ingredient that governs the microstructure of the granular medium, from a static point of view. Moreover, the buckling of force-chains is related to the increase of kinetic energy of the sample.

2. Second, the collapse of force-chains is strongly influenced by the surrounding environment, which comprises grain-loops: from firm grain-loops of 3 particles to deformable grain-loops of 6 particles. It is also proven that, around force-chains buckling, looser patterns can be found. In this surrounding environment, there are grain-loops that support force-chains. When a force-chain is created, it is supported by a greater number of attached grain-loop L-3; however, this quantity decreases over time until the force-chain buckles. On the contrary, bigger attached grain-loops L-6 have an opposite development: they have a small number at the early state of force-chain lifespan, and then this number increases till the force-chain buckles. Force-chains and grain-loops share a symbiosis relation.

- This thesis also tries to point out the importance of the second-order work to investigate instability; it can be used as a fundamental approach on both macroscopic scale and microscopic scale Nicot et al. [2007, 2012a]. The study concerning the second-order work on the contact scale draws several conclusions:

  1. From a numerical point of view, it is confirmed that macroscopic and microscopic expressions of second-order work are equivalent for a given volume of materials in quasi-static regime.
  2. The vanishing of the microscopic second-order work, which is defined as the appearance of contacts c^-, is distributed in accordance with the failure of the sample in the case of 2D biaxial test of a dense specimen: contacts c^- are located largely inside the shear band.
  3. It is observed that the distribution of contacts c^- also shows a good correlation with the collapse of force-chains: the magnitude of the second-order work (when negative) at contact c^- around buckling grains of force-chains is larger than the second-order work computed on contact c^- far from buckling grains; however, the appearance of contact c^- is not a crucial indication of the collapse of force-chains.
  4. For the case of grain-loops, the second-order work of the bigger grain-loops *L-6* is smaller than *L-3*. This validates the vanishing of the second-order work plays a basic role to detect instabilities, even on the microscopic scale.

The results and conclusions presented in this thesis provide more details to better understand the nature of the failure modes of granular materials through the investigation of the kinetic energy and second-order works. Furthermore, the second-order work is proven to be an efficient criterion to detect the instability of materials, not only on the macroscale but also on the mesoscale and microscale, including force-chains and grain-loops species.

By taking into account the mesostructures and the second-order work, this thesis provides more utilities to investigate the origin of the localized failure mode in granular materials. The force-chain and the grain-loop might help understand the appearance of the shear-band and help answer the question why and how the dense granular system chooses such patterns to develop when the failure occurs.

Mesostructures play an important role to the behaviour of granular materials and they are not limited to force-chains and grain-loops: there are other types of mesostructures inside granular media (for example: grain cluster Hadda et al. [2015]). Furthermore, in this thesis, force-chains and grain-loops are considered as mesostructures inside granular media that limited to 2D case only. Expanding to 3D study is probably a promising future research direction. For the case of force-chains, several studies in 3D space have been carried out (Pucilowski and Tordesillas [2010]). However, it is still lacking attention for grain-loops; one of the reason is the hyper complexity of finding the equivalent element in 3D for 2D grain-loops. Therefore, a better and more detailed definition of 3D "grain-loops" needs to be developed and taken into account for the 3D investigation.

Bibliography

Alonso-Marroquın, F. (2004). *Micromechanical investigation of soil deformation: incremental response and granular ratcheting*. PhD thesis, PhD thesis, Universtiät Stuttgart.

Alonso-Marroquin, F. and Herrmann, H. (2005). The incremental response of soils. an investigation using a discrete-element model. *Journal of Engineering Mathematics*, 52(1):11–34.

Antony, S., Momoh, R., and Kuhn, M. (2004). Micromechanical modelling of oval particulates subjected to bi-axial compression. *Computational materials science*, 29(4):494–498.

Bardet, J. (1994). Numerical simulations of the incremental responses of idealized granular materials. *International Journal of Plasticity*, 10(8):879–908.

Bigoni, D. (2000). *Bifurcation and instability of non-associative elastoplastic solids*. Springer.

Bigoni, D. and Hueckel, T. (1991). Uniqueness and localization–i. associative and non-associative elastoplasticity. *International Journal of Solids and Structures*, 28(2):197 – 213.

Bonilla, R. R. O. (2004). *Numerical simulations of undrained granular media*. PhD thesis, University of Waterloo.

Calvetti, F., Viggiani, G., and Tamagnini, C. (2003). A numerical investigation of the incremental behavior of granular soils. *Rivista italiana di geotecnica*, 37(3):11–29.

Cambou, B., Jean, M., and Radjai, F. (2013). *Micromechanics of Granular Materials*. ISTE. Wiley.

Campbell, C. S. (2003). A problem related to the stability of force chains. *Granular Matter*, 5(3):129–134.

Chambon, R. and Caillerie, D. (1999). Existence and uniqueness theorems for boundaryvalue problems involving incrementally non linear models. *International journal of solids and structures*, 36(33):5089–5099.

Chambon, R., Caillerie, D., and Viggiani, G. (2004). Loss of uniqueness and bifurcation vs instability: some remarks. *Revue française de génie civil*, 8(5-6):517–535.

Chareyre, B. (2003). *Discrete element modeling of composites soil-geosynthetics structures: application to trench anchorages at the top of slopes*. Theses, Université Joseph-Fourier - Grenoble I.

Cundall, P. A. and Strack, O. D. L. (1979). A discrete numerical model for granular assemblies. *Géotechnique*, 29:47–65(18).

Darve, F. and Laouafa, F. (2000). Instabilities in granular materials and application to landslides. *Mechanics of Cohesive-frictional Materials*, 5(8):627–652.

Darve, F., Servant, G., Laouafa, F., and Khoa, H. (2004). Failure in geomaterials: continuous and discrete analyses. *Computer Methods in Applied Mechanics and Engineering*, 193(27–29):3057 – 3085.

Desrues, J. (2004). Tracking strain localization in geomaterials using computerized tomography. *X-ray CT for Geomaterials*, pages 15–41.

Desrues, J. and Viggiani, G. (2004). Strain localization in sand: an overview of the experimental results obtained in grenoble using stereophotogrammetry. *International Journal for Numerical and Analytical Methods in Geomechanics*, 28(4):279–321.

Di Prisco, C. and Imposimato, S. (1997). Experimental analysis and theoretical interpretation of triaxial load controlled loose sand specimen collapses. *Mechanics of Cohesive-frictional Materials*, 2(2):93–120.

Drucker, D. C. (1957). A definition of stable inelastic material. Technical report, DTIC Document.

Gardiner, B. and Tordesillas, A. (2004). Micromechanics of shear bands. *International Journal of Solids and Structures*, 41(21):5885–5901.

Gudehus, G. (1979). A comparison of some constitutive laws for soils under radially symmetric loading and unloading. *Canadian Geotechnical Journal*, 20:502–516.

Hadda, N., Nicot, F., and Darve, F. (2013). *Aspects micromécaniques de la rupture dans les milieux granulaires.* Thèse de doctorat Mécanique, génie mécanique Grenoble 2013.

Hadda, N., Nicot, F., Wan, R., and Darve, F. (2015). Microstructural self-organization in granular materials during failure. *Comptes Rendus Mécanique*, 343(2):143–154.

Hill, R. (1958). A general theory of uniqueness and stability in elastic-plastic solids. *Journal of the Mechanics and Physics of Solids*, 6(3):236 – 249.

Hunt, G. W., Tordesillas, A., Green, S. C., and Shi, J. (2010). Force-chain buckling in granular media: a structural mechanics perspective. *Philosophical Transactions of the Royal Society of London A: Mathematical, Physical and Engineering Sciences*, 368(1910):249–262.

Iordache, M.-M. and Willam, K. (1998). Localized failure analysis in elastoplastic cosserat continua. *Computer Methods in Applied Mechanics and Engineering*, 151(3):559–586.

Iwashita, K. and Oda, M. (2000). Micro-deformation mechanism of shear banding process based on modified distinct element method. *Powder Technology*, 109(1):192–205.

Koïter, W. T. (1969). On the thermodynamic background of elastic stability theory. problems of hydro-dynamics and continuum mechanics. *In SIAM, pages 423 - 433, Philadelphia.*

Kuhn, M. R. (2010). Micro-mechanics of fabric and failure in granular materials. *Mechanics of Materials*, 42(9):827–840.

Kuhn, M. R. and Bagi, K. (2004). Contact rolling and deformation in granular media. *International journal of solids and structures*, 41(21):5793–5820.

Kuhn, M. R. and Bagi, K. (2005). On the relative motions of two rigid bodies at a compliant contact: application to granular media. *Mechanics Research Communications*, 32(4):463–480.

Lanier, J. and Jean, M. (2000). Experiments and numerical simulations with 2d disks assembly. *Powder Technology*, 109(1):206–221.

Lyapunov, A. (1907). Problème général de la stabilité des mouvements. *Annales de la faculté des sciences de Toulouse (France)*, 9:203–474.

Mahboubi, A., Ghaouti, A., and Cambou, B. (1996). La simulation numérique discrète du comportement des matériaux granulaires. *Revue française de géotechnique*, (76).

Mandel, J. (1966). *Cours de mécanique des milieux continus*. Gauthier-Villars.

Mehlhorn, K. and Michail, D. (2007). Implementing minimum cycle basis algorithms. *Journal of Experimental Algorithmics (JEA)*, 11:2–5.

Neilsen, M. and Schreyer, H. (1993). Bifurcations in elastic-plastic materials. *International Journal of Solids and Structures*, 30(4):521–544.

Ng, T.-T. (2004). Shear strength of assemblies of ellipsoidal particles. *Geotechnique*, 54(10):659–669.

Nicot, F. and Darve, F. (2007). A micro-mechanical investigation of bifurcation in granular materials. *International Journal of Solids and Structures*, 44(20):6630–6652.

Nicot, F., Darve, F., and Dat Vu Khoa, H. (2007). Bifurcation and second-order work in geomaterials. *International journal for numerical and analytical methods in geomechanics*, 31(8):1007–1032.

Nicot, F., Hadda, N., Bourrier, F., Sibille, L., and Darve, F. (2011). Failure mechanisms in granular media: a discrete element analysis. *Granular Matter*, 13(3):255–260.

Nicot, F., Hadda, N., Bourrier, F., Sibille, L., Wan, R., and Darve, F. (2012a). Inertia effects as a possible missing link between micro and macro second-order work in granular media. *International Journal of Solids and Structures*, 49(10):1252–1258.

Nicot, F., Sibille, L., and Darve, F. (2009). Bifurcation in granular materials: An attempt for a unified framework. *International Journal of Solids and Structures*, 46(22):3938–3947.

Nicot, F., Sibille, L., and Darve, F. (2012b). Failure in rate-independent granular materials as a bifurcation toward a dynamic regime. *International Journal of Plasticity*, 29(0):136 – 154.

Nova, R. (1994). Controllability of the incremental response of soil specimens subjected to arbitrary loading programmes. *Journal of the Mechanical behavior of Materials*, 5(2):193–202.

Oda, M. (2004). Microstructure of shear band developed in toyoura sand by means of microfocus x-ray computed tomography. *Geotechnique*, 54:539–542.

Oda, M. and Iwashita, K. (2000). Study on couple stress and shear band development in granular media based on numerical simulation analyses. *International journal of engineering science*, 38(15):1713–1740.

Osinov, V. and Wu, W. (2005). Instability and ill-posedness in the deformation of plastic solids: some correlations through simple examples. *Trends in Applications of Mathematics to Mechanics*, pages 361–370.

O'Sullivan, C. (2011). *Particulate discrete element modelling*. Taylor & Francis.

Peters, J., Muthuswamy, M., Wibowo, J., and Tordesillas, A. (2005). Characterization of force chains in granular material. *Physical review E*, 72(4):041307.

Petryk, H. (1993). *Theory of bifurcation and instability in time-independent plasticity*. Springer.

Prunier, F., Laouafa, F., and Darve, F. (2009a). 3d bifurcation analysis in geomaterials: Investigation of the second order work criterion. *European Journal of Environmental and Civil Engineering*, 13(2):135–147.

Prunier, F., Nicot, F., Darve, F., Laouafa, F., and Lignon, S. (2009b). Three-dimensional multiscale bifurcation analysis of granular media. *Journal of Engineering Mechanics*, 135(6):493–509.

Pucilowski, S. and Tordesillas, A. (2010). Building blocks for the self-assembly of granular materials in three-dimensions.

Radjai, F., Roux, S., and Moreau, J. J. (1999). Contact forces in a granular packing. *Chaos: An Interdisciplinary Journal of Nonlinear Science*, 9(3):544–550.

Radjai, F., Wolf, D. E., Jean, M., and Moreau, J.-J. (1998). Bimodal character of stress transmission in granular packings. *Phys. Rev. Lett.*, 80:61–64.

Raniecki, B. (1979). Uniqueness criteria in solids with non-associated plastic-flow laws at finite deformations. *Bulletin De L Academie Polonaise Des Sciences-Serie Des Sciences Techniques*, 27(8-9):721–729.

Raniecki, B. and Bruhns, O. (1981). Bounds to bifurcation stresses in solids with non-associated plastic flow law at finite strain. *Journal of the Mechanics and Physics of Solids*, 29(2):153–172.

Rice, J. R. (1976). The localization of plastic deformation. In *in: WT Koiter (Ed.), Theoretical and Applied Mechanics*. Citeseer.

Royis, P. and Doanh, T. (1998). Theoretical analysis of strain response envelopes using incrementally non-linear constitutive equations. *International journal for numerical and analytical methods in geomechanics*, 22(2):97–132.

Rudnicki, J. W. and Rice, J. (1975). Conditions for the localization of deformation in pressure-sensitive dilatant materials. *Journal of the Mechanics and Physics of Solids*, 23(6):371–394.

Servant, G., Darve, F., Desrues, J., and Georgopoulos, I. (2005). Diffuse modes of failure in geomaterials. *Deformation characteristics of geomaterials*, pages 181–198.

Sibille, L. (2006a). *Modélisations discrètes de la rupture dans les milieux granulaires*. PhD thesis, Institut National Polytechnique de Grenoble-INPG.

Sibille, L. (2006b). *Modélisations discrètes de la rupture dans les milieux granulaires*.

Sibille, L., Nicot, F., Donzé, F.-V., and Darve, F. (2009). Analysis of failure occurrence from direct simulations. *European Journal of Environmental and Civil Engineering*, 13(2):187–201.

Sibille, L., Nicot, F., Donzé, F., and Darve, F. (2007). Material instability in granular assemblies from fundamentally different models. *International journal for numerical and analytical methods in geomechanics*, 31(3):457–481.

Smart, A. G. and Ottino, J. M. (2008). Evolving loop structure in gradually tilted two-dimensional granular packings. *Physical Review E*, 77(4):041307.

Šmilauer, V., Catalano, E., Chareyre, B., Dorofeenko, S., Duriez, J., Gladky, A., Kozicki, J., Modenese, C., Scholtès, L., Sibille, L., Stránský, J., and Thoeni, K. (2010). Yade Reference Documentation. In Šmilauer, editor, *Yade Documentation*. The Yade Project, 1st edition. http://yade-dem.org/doc/.

Thompson, K., Gray, J., et al. (2004). Granular materials: fundamentals and application. *Granular materials: fundamentals and application*.

Thornton, C. (2000). Numerical simulations of deviatoric shear deformation of granular media. *Géotechnique*, 50(1):43–53.

Tordesillas, A. (2007). Force chain buckling, unjamming transitions and shear banding in dense granular assemblies. *Philosophical Magazine*, 87(32):4987–5016.

Tordesillas, A., Lin, Q., Zhang, J., Behringer, R., and Shi, J. (2011a). Structural stability and jamming of self-organized cluster conformations in dense granular materials. *Journal of the Mechanics and Physics of Solids*, 59(2):265–296.

Tordesillas, A. and Muthuswamy, M. (2009). On the modeling of confined buckling of force chains. *Journal of the Mechanics and Physics of Solids*, 57(4):706–727.

Tordesillas, A., Shi, J., and Tshaikiwsky, T. (2011b). Stress-dilatancy and force chain evolution. *International Journal for Numerical and Analytical Methods in Geomechanics*, 35(2):264–292.

Tordesillas, A., Walker, D. M., and Lin, Q. (2010a). Force cycles and force chains. *Physical Review E*, 81(1):011302.

Tordesillas, A., Walsh, S. D., and Muthuswamy, M. (2010b). The effect of local kinematics on the local and global deformations of granular systems. *Mathematics and Mechanics of Solids*, 15(1):3–41.

Tordesillas, A., Zhang, J., and Behringer, R. (2009). Buckling force chains in dense granular assemblies: physical and numerical experiments. *Geomechanics and Geoengineering: An International Journal*, 4(1):3–16.

Valanis, K. (1985). On the uniqueness of solution of the initial value problem in softening materials. *Journal of applied mechanics*, 52(3):649–653.

Valanis, K. (1989). Banding and stability in plastic materials. *Acta mechanica*, 79(1-2):113–141.

Walker, D. M. and Tordesillas, A. (2010). Topological evolution in dense granular materials: a complex networks perspective. *International Journal of Solids and Structures*, 47(5):624–639.